University of Alberta

Practical and Applied Reflectance Spectroscopy: Automated Drill Core Logging and Mineral Mapping

by

Michelle Coreena Tappert

A thesis submitted to the Faculty of Graduate Studies and Research
in partial fulfillment of the requirements for the degree of

Doctor of Philosophy

Department of Earth and Atmospheric Sciences

Fall 2012
Edmonton, Alberta

Abstract

This thesis investigates three ways that automated reflectance spectroscopy can be used for applied purposes: the automated logging of drill core into ore-bearing and barren zones, the analysis of minerals to provide evidence of hydrothermal alteration, and the creation of mineral maps to show crystal orientation.

Reflectance spectra collected from 300 meters of drill core from the iron oxide-copper-gold deposit (IOCG) at Olympic Dam using HyLogger were analyzed between 870 and 960, and 2,190 and 2,230 nm to identify hematite (i.e., mineralized lithologies) and phengite (i.e., barren lithologies), respectively. The results were plotted as a function of depth to produce a log that accurately identified ore-bearing and barren zones. The most intense absorption features between 870 and 960 nm, and 2,190 and 2,230 nm were also found to correspond to iron and aluminum concentrations, respectively.

Reflectance spectra were also collected from the same drill core using HyLogger 2 and were analyzed between 2.190 and 2.230 μm to evaluate the abundance and mineral chemistry of phengite. Microprobe results from 597 phengite grains were compared to the spectral results, and it was revealed that in the ore-bearing zones, phengite displayed a higher-Al content and lower Mg-number than phengite from the barren zones. Mid-infrared spectra collected from individual phengite crystals revealed that high-Al phengites produced a peak at 9.59 μm, and low-Al phengites produced a peak at 9.57 μm.

To document the effect that crystal orientation has on the mid-infrared reflectance spectrum of quartz, spectra were collected at a 100 x 100 μm spot size from an oriented quartz crystal and from quartz crystals contained within a quartz-bearing granite hand sample (Inco-37). Spectra from the optic axis (i.e., c-axis) produced an intense trough at 8.63 μm, and a peak at 12.50 μm. Spectra from the a-axis produced a less intense trough at 8.63 μm, and two peaks at 12.50 and 12.79 μm. Furthermore, the band ratio $Ref_{9.01}/Ref_{8.63}$ was used to estimate the orientation of quartz crystals.

Acknowledgements

First and foremost, I would like to thank my supervisor, Benoit Rivard, for his time, effort, and patience. His support for my research, my many side projects, and me has made these last few years quite enjoyable.

Although most of the scholarly work for this PhD was completed at the University of Alberta, this research was initiated at the University of Adelaide, South Australia. I would specifically like to thank David Giles, who provided me with the opportunity to work on the drill core from Olympic Dam. While in Adelaide, I also received assistance from Alan Mauger, John Huntington, Georgina Gordon, John Keeling, John Foden, Kathy Ehrig, the staff at the core library, the staff at Adelaide Microscopy, and the staff at Flinders Diamonds and FMES.

I have been a somewhat regular fixture at the University of Alberta since 1996, and during my time there, I have become indebted to a few people: Karlis Muehlenbachs, Sergei Matveev, Thomas Stachel, Thomas Chacko, Alex Wolfe, Ryan McKeller, and Stacey Gibb. Thank you for your help.

I would also like to thank the professors and staff at the University of Innsbruck, Austria, for providing me with access to their facilities. In particular, I would like to thank Roland Stalder for graciously allowing me to use the infrared spectrometer.

Finally, I would like to thank the numerous individuals who have supported me personally throughout the last few years. There are too many to list, but I hope that you know that I have appreciated your involvement in my life. In specific, however, I would like to thank Lelde Muehlenbachs, who was always keen to organize an evening out on the town; Jody Backer-Campeau, who rarely said no when I asked her to hang out; and Susan Egge-Morisson, who still makes me laugh.

Of course, I would also like to thank my immediate and extended family. I want to thank my mother, Janet Palser, for her support and understanding, and my father, Gerald Goryniuk, for his unique viewpoints on many topics. Most importantly, I would like to thank my husband, Ralf Tappert, who has been a steady source of joy and inspiration during our time together. Lastly, I would like to thank Heidi Tappert, who had the patience to wait until the last paper was mostly written before deciding that it was time to be born.

Table of Contents

List of Tables

List of Figures

Chapter 1: Introduction

1.1 The Evolution of Reflectance Spectroscopy

In 1906, the first absorption, emission, and reflectance spectra of minerals and rocks were published by Coblentz, who collected thousands of spectra using handmade spectrometers (Coblentz, 1906). During World War II, similar styles of handmade spectrometers were used to verify the composition and quality of materials although absorption spectra were mainly used for these purposes (Lyon et al., 1959; Coates, 1996). After the war, and after the commercial development of other analytical instruments that were better suited for quantitative analysis (e.g., XRF, mass spectrometers, etc.), reflectance spectroscopy was used mainly for qualitative purposes. Since then, much time and effort has been dedicated to acquiring reflectance spectra from minerals and rocks, but much of the analysis has focused on the documentation of reflectance spectra and the development of qualitative applications (e.g., Saksena, 1940; Farmer, 1974; Salisbury, 1991; Burns, 1993; Clark, 2004).

One hundred years after Coblentz built his first spectrometers, which required three to five hours to collect a single reflectance spectrum, modern automated spectrometers can collect hundreds or even thousands of reflectance spectra in the same amount of time. These automated instruments have been designed to collect larger amounts of reflectance spectra at smaller spatial resolutions than their non-automated counterparts. Many of the interpretation difficulties encountered when analyzing reflectance spectra are due to the effects of grain size, porosity, and compaction because changes in the physical properties

of a sample can change the shape and intensity of most spectral features, especially in the mid-infrared (e.g., Adams and Filice, 1967; Lyon, 1964; Conel, 1969; Hunt and Logan, 1972; Logan et al., 1973; Hapke, 1981; Morris et al., 1985; Hapke, 1986; Salisbury et al., 1987; Salisbury et al., 1991; Salisbury and Wald, 1992; Mustard and Hays, 1997; Cooper et al., 2002). When reflectance spectra are collected in sufficiently large numbers (e.g., > 5,000 spectra/dataset), and/or at small spatial resolutions (e.g., 2 x 2 mm), many of the complexities introduced by grain size, porosity, and compaction are minimized. As a result, reflectance spectra collected by modern automated spectrometers can be used for qualitative purposes like the spectra collected by their predecessors, but they can also be used to quantify mineral abundance, analyze mineral chemistry, and determine crystal orientation.

There are two types of spectrometers that can collect reflectance spectra in an automated manner for mineralogical and geological purposes:

(1) Line scanning spectrometers collect individual spectra in a straight line and they are primarily used to log drill cores (e.g., Huntington et al., 2006; Mauger et al., 2007; Mauger and Hore, 2009; Mason and Huntington, 2010; Smith 2010; Tappert et al., 2011; Tappert, 2012a). These instruments produce a spectrum approximately every 1 cm, with a pixel size of ~1 x 1 cm. The size of the spectral dataset is dependent on the length of the drill core, but a typical dataset can contain a few thousand to a hundred thousand spectra. These instruments are best suited for identifying the presence or absence of target minerals along a drill core, and the results are often presented as depth profiles.

(2) Area scanning spectrometers collect spectral data over the entire surface of a sample, and these instruments produce much larger datasets (>100,000 spectra) than line scanning spectrometers. In addition, they also have the ability to collect spectra at a much smaller spatial resolution (i.e., 50 x 50 µm to 2 x 2 mm spot size) (Tappert, 2012b). These instruments are used to identify the presence and absence of minerals in a thin section or a hand sample, to calculate modal mineral abundances, to evaluate the mineral chemistry of individual phases, and to estimate crystal orientation. The results are often presented as a pixel-based color images.

In general, the data collected by automated reflectance spectrometers provide geologists with detailed mineralogical information that can cover kilometer-sized field areas and the sub-millimeter domains of individual minerals. This will provide us with many opportunities to observe and investigate mineral occurrences that have not yet been documented using other available analytical techniques.

1.2 Why Conduct This Research

The previous section describes the types of automated instrumentation that can be used to collect reflectance spectra. Unfortunately, the manufacturers of instruments rarely provide the tools needed to interpret the spectra. Limited visualization software and processing algorithms are often included with these instruments, but most manufacturers have focused their attentions on data acquisition rather than data analysis. Consequently, there is no standardized

method of data analysis currently in use, and this is different to many of the other analytical techniques. The research presented in this thesis contributes valuable knowledge that will hopefully help with the development of a comprehensive and efficient standardized method of analysis to be used on reflectance spectra.

1.3 Organization of the Thesis

This thesis is comprised of three chapters (Chapters 2, 3, 4) that contain manuscripts, and an additional chapter (Chapter 5) that provides a general discussion and conclusions. Chapter 2 (Automated drill core logging using visible and near-infrared reflectance spectroscopy: A case study from the Olympic Dam IOCG deposit, South Australia**)** examines the challenges associated with the automated drill core logging of mineralized drill core from the iron oxide-copper-gold deposits at Olympic Dam, South Australia. The contents of this Chapter were published in 2011 in Economic Geology (Vol. 106, pp. 289-296). Chapter 3 (The mineral chemistry, near-infrared, and mid-infrared reflectance spectroscopy of phengite from the Olympic Dam IOCG deposit, South Australia) continues with the analysis of the drill core from Olympic Dam. This research compares the reflectance spectroscopy and mineral chemistry of phengites in the ore-bearing zone to the phengites in the barren zone. Chapter 4 (Natural variability in the mid-infrared reflectance spectra of quartz caused by crystal orientation) explores the effect that crystallographic orientation has on the mid-infrared reflectance spectra of quartz collected at very small spatial resolutions (e.g., 100 x 100 μm). Finally, Chapter 5 (General Discussion and Conclusions) discusses the research that has

been presented in this thesis, particularly the usage of reflectance spectroscopy as a qualitative and quantitative analytical tool.

1.4 References

Adams, J.B., and Filice, A.L. (1967) Spectral reflectance 0.4 to 2.0 microns of silicate rock powders. Journal of Geophysical Research, 72, 5,705-5,715.

Burns, R.G. (1993) Mineralogical applications of crystal field theory. 551 p. Cambridge University Press, Cambridge.

Clark, R.N. (2004) Chapter 2: Spectroscopy of rocks and minerals, and principles of spectroscopy. In M.S. Ramsey, P.L. King, and G.A. Swayze, Eds. Infrared Spectroscopy in Geochemistry, Exploration Geochemistry, and Remote Sensing, p. 17-55. Mineralogical Association of Canada, London, Ontario.

Coates, J.P. (1996) The interpretation of infrared spectra: Published reference sources. Applied Spectroscopy Reviews, 31(1), 179-192.

Coblentz, W.W. (1906) Infra-red absorption and reflection spectra. Physical Review (Series I), 23(2), 125.

Conel, J.E. (1969) Infrared emissivities of silicates: experimental results and a cloudy atmosphere model of spectral emission from condensed particulate mediums. Journal of Geophysical Research, 74, 1,614-1,623.

Cooper, B.L., Salisbury, J.W., Killen, R.M., and Potter, A.E. (2002) Midinfrared spectral features of rocks and their powders. J. Geophys. Res., 107(E4), 5,017.

Farmer, V.C. (1974) The infrared spectra of minerals. 539 p. Mineralogical Society, London.

Hapke, B. (1986) Bidirectional reflectance spectroscopy. 4. The extinction coefficient and the opposition effect. Icarus, 67, 264-280.

Hapke, B., and Wells, E. (1981) Bidirectional reflectance spectroscopy 2. Experiments and observations. Journal of Geophysical Research, 86, 3,055-3,060.

Hunt, G.R., and Logan, L.M. (1972) Variation of single particle mid-infrared emission spectrum with particle size. Applied Optics, 11,142-147.

Huntington, J.F., Mauger, A.J., Skirrow, R.G., Bastrakov, E.N., Connor, P., Mason, P., Keeling, J.L., Coward, D.A., Berman, M., Phillips, R., Whitbourn, L.B., and Heithersay, P.S. (2006) Automated mineralogical core logging at Emmie Bluff iron oxide-copper-gold prospect. MESA Journal, 41, 38-44.

Logan, L.M., Hunt, G.R., Salisbury, J.W., and Balsamo, S.R. (1973) Compositional implications of christiansen frequency maximums for infrared remote sensing applications. Journal of Geophysical Research, 78(23), 4,983-5,003.

Lyon, R.J.P. (1964) Evaluation of infrared spectrophotometry for compositional analysis of lunar and planetary soils. Part II: Rough and powdered surfaces. 262 p. NASA-CF-100, Washington, D.C.

Lyon, R.J.P., Tuddenham, W.M., and Thompson, C.S. (1959) Quantitative mineralogy in 30 minutes. Economic Geology, 54(6), 1,047-1,055.

Mason, P., and Huntington, J.F. (2010) HyLogger 2 components and pre-processing: an overview. In T. Munson, and K. Johnston, Eds.

Technological Note 2010-001, p. 9. Northern Territory Geological Survey, Darwin.

Mauger, A., and Hore, S. (2009) Integrating mineralogical interpretation of HyLogger data with HyMap mineral mapping, Mount Painter, South Australia. In K.R.S. Jones and K. Reinke Eds. Innovations in Remote Sensing and Photogrammetry: Lecture Notes in Geoinformation and Cartography. Springer-Verlag Berlin Heidelberg, 271-280

Mauger, A., Keeling, J.L., and Huntington, J.F. (2007) Alteration mapping of the Tarcoola Goldfield (South Australia) using a suite of hyperspectral methods. Applied Earth Science, 116(1), 2-12.

Morris, R.V., Lauer Jr., H.V., Lawson, C.A., Gibson Jr., E.K., Nace, G.A., and Stewart, C. (1985) Spectral and other physicochemical properties of submicron powders of hematite (α-Fe_2O_3), maghemite (γ-Fe_2O_3), magnetite (Fe_3O4), goethite (α-FeOOH), and lepidocrocite (γ-FeOOH). Journal of Geophysical Research, 90, 3,126–3,144.

Mustard, J.F., and Hays, J.E. (1997) Effects of hyperfine particles on reflectance spectra from 0.3 to 25 μm. Icarus, 125, 145-163.

Saksena, B. (1940) Analysis of the Raman and infra-red spectra of α-quartz. Proceedings Mathematical Sciences, 12(1), 93-139.

Salisbury, J.W., Hapke, B., and Eastes, J.W. (1987) Usefulness of weak bands in mid-infrared remote sensing of particulate planetary surfaces. Journal of Geophysical Research, 92, 702-710.

Salisbury, J.W., and Wald, A. (1992) The role of volume scattering in reducing spectral contrast of Reststrahlen bands in spectra of powdered minerals. Icarus, 92, 121-128.

Salisbury, J.W., Walter, L.S., Vergo, N., and D'Aria, D.M. (1991) Infrared (2.1-25 μm) spectra of minerals. Johns Hopkins University Press, Baltimore.

Smith, B.R. (2010) Drillhole report for 09CPD002, Irindina Province, Northern Territory: National Virtual Core Library NTGS Node: HyLogger 2-7. In T.J. Munson, and K.J. Johnston, Eds. Northern Territory Geological Survey, Record 2010-006.

Tappert, M., Rivard, B., Giles, D., Tappert, R., and Mauger, A. (2011) Automated drill core logging using visible and near-infrared reflectance spectroscopy: a case study from the Olympic Dam IOCG deposit, South Australia. Economic Geology, 106, 289-296.

Tappert, M., (2012a) The mineral chemistry, near-infrared, and mid-infrared reflectance spectroscopy of phengite from the Olympic Dam IOCG deposit, South Australia, Chapter 3, this thesis.

Tappert, M., (2012b) Natural variability in the mid-infrared reflectance spectra of quartz caused by crystal orientation, Chapter 4, this thesis.

Chapter 2: Automated drill core logging using visible and near-infrared reflectance spectroscopy: a case study from the Olympic Dam IOCG deposit, South Australia[1]

2.1 Introduction

With the development of automated drill core scanning spectrometers, visible and near-infrared (400-2500 nm) reflectance spectra can be collected directly from the surface of drill core, and these spectra contain information about mineral chemistry, mineral abundance, and the physical state of the drill core (e.g., porosity, grain size, degree of coherence) (Hunt, 1977; Clark et al., 1990; Clark, 1999, and references therein). Automated scanning spectrometers have been used to identify zones of hydrothermal alteration, to log drill core, and to grade ore (e.g., Gallie et al., 2002; Keeling et al., 2004; Huntington et al., 2006; Kupsch and Catuneanu, 2007; Mauger et al., 2007). As these instruments become more widely available, they are more likely to be used for the in-situ identification of minerals, particularly in situations where large amounts of drill core are recovered.

Collecting reflectance spectra directly from the surface of drill core using automated drill core logging instruments is a well-established and straightforward

[1] A version of this chapter has been published in *Economic Geology*, 106: 289-206.

technique, which usually produces large datasets (>10,000 spectra). However, the interpretation of the resulting data, which is the key to gaining the correct mineralogical information, requires an in-depth knowledge about the spectral properties of the minerals and rocks involved. In general, interpreting the spectral dataset can be difficult when the rocks are comprised of many minerals and when the physical properties of the rocks interfere with the amplitude and position of absorption features (Lyon, 1962; Clark, 1999, and references therein), which is often the case in and around many hydrothermal ore deposits. As a result, algorithms are often used to interpret the spectra, but many of these algorithms are computationally intensive, and this is detrimental if high turnover is required—such as at mine sites or in large drilling programs. In addition, many of the algorithms are not designed to interpret spectra collected from rocks containing complex mineral mixtures or metallic minerals. This means that the logs produced using these algorithms for mineralized drill core are often inaccurate or are only rough approximations.

Olympic Dam is located 560 kilometres north of Adelaide, South Australia, near the town of Roxby Downs. In addition to containing iron oxides, copper, and gold (i.e., IOCG), the Olympic Dam deposit hosts uranium, silver, and rare-earth elements (REEs). The ore body occurs within the Olympic Dam Breccia Complex, which is hosted by the Roxby Downs Granite. The center of the Olympic Dam Breccia Complex consists mainly of barren hematite-quartz breccias. Cu-Fe sulfide-bearing breccias are located northwest and southeast of this center zone, and beyond this are altered and barren Roxby Downs Granite

(Roberts and Hudson, 1983; Hauck, 1990; Reeve et al., 1990; Oreskes and Einaudi, 1992; Cross et al., 1993).

Hematitic and sericitic alteration types are dominant at Olympic Dam and are often diagnostic when identifying ore-bearing or barren zones. Hematite-rich assemblages are closely associated with the presence of ore minerals, such as the Cu-Fe sulfides (e.g., chalcocite (Cu_2S), bornite (Cu_5FeS_4), and chalcopyrite ($CuFeS_2$)). Rocks that are affected by intense sericitic alteration, on the other hand, are usually barren. At Olympic Dam, zones of sericitic alteration are dominated by phengite as the main alteration product of feldspar, and it is notable that rocks closer to the ore-bearing zones are more intensely sericitized (i.e., more phengite-rich) than those further away (Hitzman et al., 1992; Haynes et al., 1995). Multiple episodes of brecciation caused by hydrothermal fluid flow have produced a complex intermingling of hematite-rich and phengite-rich rocks. As a result, subtle changes in mineralogy along the drill core are often not easily observed during visible inspection (Cross et al., 1993).

Reflectance spectroscopy is particularly useful when logging the drill core from Olympic Dam because hematite and phengite are the dominant alteration minerals, and they are spectrally active at different wavelengths between 400 and 2500 nm. For example, the iron-bearing minerals containing ferric iron (Fe^{3+}), like hematite, goethite, and lepidocrocite produce absorption features between 850 and 970 nm due to the electronic transitions that occur in unfilled d-orbitals (White and Keester, 1966; Adams, 1968; Hunt and Salisbury, 1970; Hunt and Ashley, 1979; Sherman et al, 1982; Morris et al., 1985; Burns, 1993; Cudahy and

Ramanaidou, 1997; Cornell and Schwertman, 2003). Due to their position and their intensity, the spectral features of these minerals are rarely influenced by the presence of non-iron-bearing minerals. Phengite can be characterized by the absorption feature produced by the Al-OH bond, which is observed between 2,190 and 2,230 nm (Hunt, 1979; Hunt and Ashley, 1979; Swayze et al., 1992; Post and Noble, 1993; Duke, 1994; Clark, 1999). Given the relative simplicity of the alteration mineralogy that is active in the visible and near-infrared, we present a method of analysing spectra that does not require complex algorithms. It is straightforward and easily performed on reflectance spectra collected from the mineralised drill core at Olympic Dam.

2.2 Samples and Methods

Drill core RU39-5371 is 300 meters in length and was examined visually and scanned using the HyLogger instrument at the PIRSA facilities in Adelaide. The spectral data were compared to whole rock analyses. In addition, 16 samples were collected from the drill core for petrographic analysis and to collect compositional data for their mineral components, with particular emphasis on the composition of the phengites.

In general, the drill core contains three visibly distinct zones:

- 0 to 30 meters contains ore-bearing hematite breccias. This portion of the drill core is comprised of dull-red and specular hematite that forms clasts and matrix. Quartz is also present, in addition to chalcocite and bornite, uranium-bearing and REE-bearing minerals.

- 30 to 202 meters contains complexly intermingled hematite breccias, hematite-rich breccias, and heterolithic breccias. This part of the drill core is very heterogenous and is characterized by the first appearance of sericite (i.e., phengite) at ~30 meters. A zone of strongly altered granite, which may represent a large country-rock clast, is located between ~35 and 40 meters. Chlorite, fluorite, barite, and carbonate are also present in some lithologies. From 0 to 51 meters, chalcocite and bornite are the dominant Cu-Fe sulfides, but below 51 meters, chalcopyrite is most common.
- 202 to 300 meters contains the hematite-poor, barren rocks of the Roxby Downs Granite suite. This portion of the drill core is only weakly brecciated or unbrecciated. Hematite-rich rocks are absent, but small grains of hematite can be present as a minor mineral component. The rocks are mainly comprised of K-feldspar, quartz, phengite, in addition to chlorite, carbonate, barite, and fluorite.

The hole was drilled in 2003, but the scanning did not occur until 2006. Due to the fact that the drill core was kept outside for an undisclosed amount of time between 2003 and 2006 before being scanned by HyLogger, the drill core showed signs of surface oxidization. This surface oxidation was characterized by the presence of orange and light brown staining, probably caused by fine-grained varieties of iron hydroxides, such as goethite and lepidocrocite (Cornell and Schwertmann, 2003). This oxidation was most apparent on rocks that were composed of altered granites but was less obvious on hematite-rich rocks.

2.2.1 Spectra Collection Using HyLogger

Reflectance spectra from the drill core were collected using the HyLogger instrument, which continuously scans at a rate of 60 mm/s. Visible and near-infrared (400-2500 nm) bi-directional reflectance measurements were collected over 196 spectral channels (~16 nm band spacing) (Huntington et al., 2006). The spectra were collected every millimetre with a spot size of 8 x 8 mm. These scans were averaged for approximately 8 mm of travel, yielding a total of 125 spectra per meter. Digital pictures of the core were taken using a linescan camera to build a continuous image of the drill core at a spatial resolution of 0.1 mm, which is useful for the visual identification of minerals after the drill core has been scanned. A laser profilometer was used to measure the distance from the sensor to the core at a vertical resolution of 0.25 mm. HyLogger is equipped with three bore-sighted grating spectrophotometers. The spectrometers measured calibrated radiance, which was afterwards converted to spectral reflectance via calibration to a spectralon standard. This standard was measured before each core tray was scanned.

2.2.2 Quality Control

The spectra collected by HyLogger include those from non-mineralogical materials, such as wooden blocks, plastic depth markers, and the core tray. Spectra from these non-mineralogical materials were identified and excluded from the analysis. Spectra from rubble or fractures were also identified and excluded.

The reflectance spectra collected from the Olympic Dam drill core using the HyLogger instrument lack detail due to the fact that the instrument only

collects 196 bands between 400 and 2,500 nm. This relatively low spectral resolution, however, allows the HyLogger instrument to collect spectra very rapidly. Due to the abundance of hematite at Olympic Dam, much of the drill core is highly reflective. This high reflectivity can saturate the detectors and further decrease the quality of the spectra. As a result of these limitations, it was only possible to reliably identify the absorption features belonging to minerals found in high abundance in the drill core (e.g., hematite and phengite). In most cases, minerals present in low (<10%) abundance (e.g., chlorite, carbonate, etc.) could not be accurately identified in the spectra because their diagnostic absorption features were too weak.

2.2.3 Spectral Calculations

In the preliminary stages of analysis, a number of different techniques were utilized to interpret the reflectance spectra (e.g., linear unmixing, unsupervised classification, supervised classification), but due to the lack of spectral detail inherent in the HyLogger data, these techniques did not produce accurate results. However, three simple spectral metrics were calculated for each spectrum that produced results that matched the results of the visual drill core log and the whole rock geochemical data.

The presence of hematite and iron-bearing minerals were identified in the reflectance spectrum by determining the wavelength position of the most intense trough between 850 and 970 nm. These results not only capture the presence of hematite, but also the presence of the iron hydroxides, such as goethite and lepidocrocite on the surface of the drill core. It was found that this metric is

accurate even if performed on drill core that is slightly surface oxidized, as in our case.

Two metrics were performed between 2,190 and 2,230 nm to identify phengite. The first metric for phengite was determined using the second derivative spectrum. In this case, the maximum value between 2,190 and 2,230 nm was identified. The second metric for phengite was performed using the reflectance spectrum with the continuum removed. The continuum was removed using the curvature of the second derivative spectrum (see Berman, 2006). Once the continuum was removed, the wavelength position of the most intense trough between 2,190 and 2,230 nm was identified. The spectral range between 2,190 and 2,230 nm was selected to identify phengite because this range was large enough to characterize the presence and chemical composition of phengite without capturing the spectral features related to chlorite. If no spectral feature was present in this wavelength range, no values were produced for these calculations.

Depth profiles of the results from the first two calculations were created using a moving-average window that encompassed 301 spectra. These smoothed results were binned at a scale of 6 centimeters, and the average value was plotted for each bin. These specific smoothing and binning values were chosen because they show the changes in composition along the drill core with a high-level of detail, yet the visible clutter produced by outliers is removed.

2.2.4 Additional Compositional Information

Whole rock geochemical analyses (ICP-MS major, minor, and trace elements) for the drill core were provided by BHP Billiton at 2.5 meter (0-210 meters) or 5 meter (210-300 meters) depth intervals. In addition, the major and minor element compositions of phengites from samples collected at depths of 38 and 245 meters were determined using a CAMECA SX-51 electron microprobe at the University of Adelaide and JEOL8900R electron microprobes at the University of Frankfurt and the University of Alberta.

2.3 Results

In total, 49,500 spectra were collected from 300 meters of drill core. Of these spectra, 4,512 (8.5%) were identified as non-mineralogical. The remaining 45,285 spectra were analyzed between 850 and 970 and 2,190 and 2,230 nm.

2.3.1 Spectral Range I: 850-970 nm

Absorption features between 850 and 970 nm were present in 32,347 spectra. The most common and most intense absorption feature was located at ~890 nm, but less common and weaker absorption features were also located at ~915, ~940, and ~960 nm. Figure 2-1 (a-b) illustrates that the position of the most intense absorption feature, if plotted as a function of depth, correlates with the iron concentration along the drill core determined by whole rock geochemical analysis. This means that rocks with higher iron concentrations produce spectral features between 850 and 970 nm at lower wavelengths, and vice versa. Similar correlations also exist for copper (Figure 2-1c) and sulfur (Figure 2-1d), which

tend to be concentrated in the iron-rich zones. This correlation between the iron concentration and the absorption feature position is also illustrated in Figure 2-2a, which shows the wavelength of the most intense absorption feature between 850 and 970 nm averaged over each geochemical sampling interval (i.e., 2.5 or 5 meters) plotted against the concentration of iron for that same sampling interval.

2.3.2 Spectral Range II: 2,190-2,230 nm

In total, 29,840 spectra contained an absorption feature between 2,190 and 2,230 nm that appears as a maximum in the second derivative spectral layer. The intensity of this absorption feature plotted as a function of depth (Figure 2-1e) correlates with the concentration of aluminum in the rocks determined by whole rock geochemical analysis (Figure 2-1f). The aluminum-rich rocks also contain high concentrations of potassium (Figure 2-1g). Over each geochemical sampling interval (i.e., 2.5 or 5 meters), the intensities of the absorption features were averaged, and this value was plotted against the corresponding concentration of aluminum for that same sampling interval (Figure 2-2b).

The wavelength position of 33,836 absorption features were identified between 2,190 and 2,230 nm in the reflectance spectra after the continuum was removed. The shifting of this absorption feature on a broad scale—as the distance to the ore-bearing region changes—becomes apparent if these results are averaged over 100 meter depth intervals (Figure 2-3). From 0 to 200 meters (i.e., the main ore zone), average wavelength for the absorption feature was 2,209 nm, and from 200 to 300 meters (i.e., the barren granite zone), the average wavelength was 2,217 nm.

Microprobe analysis of micas > 2 μm in size from 38 and 245 meters reveal that they belong to the phengite series (Table 2-1). Phengites typically contain greater than 3 cations of silicon per formula unit (calculated using 11 oxygens), and contain considerable amounts of magnesium and iron (Rieder et al., 1998; Cibin, et al., 2008). In our case, the phengites contain between 3.16 and 3.51 cations of silicon and plot along the linear trend defined by the coupled-substitution of $Al^{VI}Al^{IV} \leftrightarrow Mg^{VI}Si^{IV}$ and Fe ↔ Mg (Figure 2-4) (see Schaller, 1950; Velde, 1965; Duke, 1994). Although the phengites analyzed at 38 meters contain more aluminum, per formula unit than the phengites located at 245 meters, they are still identified as phengites based on the amounts of silicon, iron, and aluminum that they contain. In general, the phengites from 245 meters contain more silicon, iron, magnesium, and potassium than the phengites from 38 meters.

2.4 Discussion

2.4.1 Hematite

The absorption features observed in the reflectance spectra at ~890 nm are produced by the electronic processes of ferric iron (Fe^{3+}) in the mineral hematite (White and Keester, 1966; Adams, 1968; Hunt and Salisbury, 1970; Hunt and Ashley, 1979; Sherman et al, 1982; Morris et al., 1985; Burns, 1993; Cudahy and Ramanaidou, 1997; Cornell and Schwertman, 2003). In the drill core, this spectral feature is observed mainly between 0 and 202 meters where it is associated with dull and specular hematite. Its presence is also linked to zones with high

abundances of other ore minerals.

Weaker absorption features are observed at ~915, ~940, and ~960 nm. These are mainly found in spectra that do not have an intense spectral feature at ~890 nm. They are most prevalent in the barren phengite-rich and hematite-poor rocks located between 202 and 300 meters, and in specific horizons between 0 and 202 meters (e.g., 35 to 40 meters). Due to the weak intensity of some of these absorption features, it is not possible to assign each to a specific mineral (Burns, 1993); however, some of these weak absorption features can be attributed to minerals such as goethite (α-FeOOH) (e.g., ~915 nm) and lepidocrocite (γ-FeOOH) (e.g., ~960 nm), which are common weathering products on the surface of iron-bearing rocks (Cornell and Schwertman, 2003). These weak absorption features are prominent in those parts of the drill core that are affected by orange and light brown staining. If the absorption features of hematite and goethite/lepidocrocite are present in a single spectrum, the hematite spectral feature is always the strongest. This means that the presence of minor amounts of iron hydroxides does not hinder the identification of hematite.

It is notable that a relationship exists between the average wavelength position of the strongest absorption feature between 850 and 970 nm and the iron concentration determined by the whole rock geochemistry (Figure 2-1b, Figure 2-2a). This means that by plotting the average wavelength position of the largest absorption feature (i.e., a single metric), the presence of multiple iron-bearing mineral phases along the drill core can be captured. For the Olympic Dam drill core, the results from this metric have been averaged over 2.5 or 5 meter sampling

intervals. The data points in the upper right part of Figure 2-2a represent data that are dominated by hematite. Data plotting in the lower left part represent sampling intervals that are dominated by lepidocrocite. Points in the middle are either mixtures of hematite, lepidocrocite, and/or goethite, or they may represent sampling intervals that are dominated by goethite.

2.4.2 Phengite

As mentioned previously, micas in the Olympic Dam drill core have a sericitic texture (i.e., fine-grained and highly birefringent) and belong to the phengite series (Table 2-1, Figure 2-4). The phengites from the heavily-brecciated ore zone produce troughs at ~2,209 nm, whereas the phengites contained in the Roxby Downs Granite produce troughs at ~2,217 nm (Figure 2-3).

It appears as if there are two populations in the data collected from the heavily-brecciate ore zone. This bimodal distribution is an artifact of the spectral resolution of the HyLogger instrument, which has a band space of ~16 nm in this portion of the spectrum. An identical analysis of the spectra collected with the HyLogger-2 instrument, which has a ~ 4 nm band spacing, was conducted, and no bimodal relationship was detected in that data (Chapter 3: Figure 3-8).

Yang et al., (2001) attributed the troughs located at ~2,215 nm to phengite, whereas the shorter wavelength troughs are often attributed to muscovite (Swayze et al., 1992; Post and Noble, 1993; Duke 1994). Since all micas in the present study were found to contain greater than 3 silicon cations per formula unit (Table 2-1), it is more likely that the troughs observed at ~2,209 nm are linked to aluminum-rich phengites, rather than muscovite. This means that the variation in

the wavelength position of the troughs between 2,190 and 2,230 nm relates to the aluminum content of phengites, which, in turn, can be related to the type and extent of hydrothermal alteration observed throughout the drill core.

The microprobe data collected from phengites at 38 meters confirm that the phengites in the ore-bearing rocks have a higher per formula unit abundance of aluminum (Table 2-1, Figure 2-4). These rocks are heavily altered and no feldspar remains. In contrast, the phengites at 245 meters, which are found in the Roxby Downs Granite where primary feldspar is still present, have lower abundances of aluminum and higher abundances of silicon, iron, and magnesium. It is likely that phengite having more aluminum in octahedral sites bound to hydroxyl (~ more total aluminum) produce the spectral features observed at shorter wavelengths, and phengite having less aluminum in octahedral sites bound to hydroxyl (~ less total aluminum; more silicon, magnesium, and iron) produce the spectral features observed at longer wavelengths (Swayze et al., 1992; Post and Noble, 1993; Duke 1994; Clark, 1999).

In this dataset, it is the abundance of phengite that changes the intensity of the spectral features identified between 2,190 and 2,230 nm (Hunt, 1979; Hunt and Ashley, 1979; Swayze et al., 1992; Post and Noble, 1993; Duke, 1994; Clark, 1999). The intensity of this absorption feature can also be related to the total concentration of aluminum along the drill core (Figure 2-1e, Figure 2-2b). This relationship, however, is affected by the presence of other aluminum-bearing minerals, such as K-feldspar and chlorite. Minerals such as K-feldspar and chlorite do not produce absorption features between 2,190 and 2,230 nm, and

they, therefore, do not contribute to the results of the spectral metric. Their presence, however, does contribute aluminum to the whole rock geochemistry totals. The scatter seen in Figure 2-2b, particularly for the higher intensity values is likely caused by the presence of K-feldspar and chlorite in addition to variable amounts of aluminum in the phengite.

2.5 Conclusions

In total, 49,500 visible and near-infrared reflectance spectra (400-2,500 nm) were collected from 300 meters of drill core originating from the Olympic Dam IOCG deposit, South Australia, using the automated scanning reflectance spectrometer HyLogger. The spectral data were limited by the level of spectral detail and by the high abundance of specular minerals (e.g., hematite and sulfides). Once it was established that the typical methods of spectral analysis were not successful in interpreting this spectral dataset, three simple metrics were derived to capture the presence and abundance of hematite and phengite. One calculation was performed between 850 and 970 to identify hematite, and two calculations were performed between 2,190 and 2,230 nm to identify phengite.

Using the results of these calculations, the major and minor compositional units were identified along the drill core, and the resulting log correlated very well with the visual inspection of the drill core and the whole rock geochemical data. In addition, the presence of oxidation minerals on the surface of the drill core, which had been left outside for an extended period of time, did not preclude the detection of hematite-rich rocks.

Automated drill core scanning spectrometers have the ability to rapidly

collect compositional data from the surface of drill core, and these datasets can provide compositional data at a much higher spatial resolution (e.g., every 8 mms) than traditional geochemical techniques (e.g., every 2.5 or 5 meters). Even though this dataset lacks spectral detail, the techniques described herein can be used to log the drill core of the heavily mineralised rocks from Olympic Dam.

2.6 Acknowledgements

The authors would like to thank Kathy Ehrig at BHP Billiton (Australia); Georgina Gordon and John Keeling at PIRSA (Australia); Sasha Pontual at AusSpec (Australia); Jon Huntington at CSIRO (Australia); and Sergei Matveev and Karlis Muehlenbachs at the University of Alberta (Canada). This project was sponsored financially between October 2007 – December 2008 by the Department of Primary Industry and Resources SA through AusScope/NCRIS.

2.7 Tables

Table 2-1. The EPMA results of phengites from 38 (n =102) and 245 meters (n=62). Data are sorted based on high, median, low, and average silicon cation content for each sample calculated using 11 oxygens.

Description	Sample Names							
	38 meters				245 meters			
	High	Med.	Low	Avg.	High	Med.	Low	Avg.
SiO_2	51.29	49.36	47.82	**48.62**	53.03	50.04	47.56	**50.60**
TiO_2	0.05	0.03	0.00	**0.03**	0.06	0.05	0.07	**0.04**
Cr_2O_3	0.02	n/a	n/a	**0.01**	0.03	0.00	0.00	**0.01**
Al_2O_3	26.83	31.90	34.74	**31.48**	26.18	28.70	32.66	**28.79**
FeO	3.15	3.32	2.12	**3.20**	4.31	4.04	2.73	**3.90**
MgO	2.11	0.64	0.38	**0.69**	2.35	1.46	1.09	**1.39**
MnO	0.00	0.00	0.00	**0.02**	0.00	0.00	0.00	**0.01**
CaO	0.02	0.96	0.56	**0.64**	0.03	0.02	0.00	**0.03**
BaO	n/a	0.10	0.13	**0.05**	0.00	0.05	0.01	**0.02**
NiO	0.00	n/a	n/a	**0.01**	0.00	0.00	0.01	**0.01**
Na_2O	0.20	0.08	0.14	**0.14**	0.19	0.18	0.13	**0.14**
K_2O	9.52	9.03	9.14	**9.23**	9.74	10.23	10.68	**9.91**
P_2O_5	0.03	n/a	n/a	**0.02**	0.02	0.01	0.00	**0.01**
F	n/a	0.00	0.00	**0.00**	1.41	0.79	0.52	**0.79**
Cl	n/a	0.03	0.00	**0.04**	n/a	n/a	n/a	**n/a**
Total	93.22	95.45	95.03	**94.13**	97.35	95.58	95.46	**95.65**
Cations								
Si	3.48	3.28	3.17	**3.27**	3.51	3.37	3.19	**3.39**
Ti	0.00	0.00	0.00	**0.00**	0.00	0.00	0.00	**0.00**
Cr	0.00	n/a	n/a	**0.00**	0.00	0.00	0.00	**0.00**
Al	2.14	2.49	2.71	**2.50**	2.04	2.28	2.58	**2.28**
Al-iv	0.52	0.73	0.83	**0.73**	0.49	0.63	0.81	**0.61**
Al-vi	1.62	1.77	1.88	**1.77**	1.56	1.65	1.78	**1.67**
Fe	0.18	0.18	0.12	**0.18**	0.24	0.23	0.15	**0.22**
Mg	0.21	0.06	0.04	**0.07**	0.23	0.15	0.11	**0.14**
Mn	0.00	0.00	0.00	**0.00**	0.00	0.00	0.00	**0.00**
Ca	0.00	0.07	0.04	**0.05**	0.00	0.00	0.00	**0.00**
Ba	n/a	0.00	0.00	**0.00**	0.00	0.00	0.00	**0.00**
Ni	0.00	n/a	n/a	**0.00**	0.00	0.00	0.00	**0.00**
Na	0.03	0.01	0.02	**0.02**	0.02	0.02	0.02	**0.02**
K	0.82	0.76	0.77	**0.79**	0.82	0.88	0.91	**0.85**
11[O] Total	6.87	6.87	6.87	**6.89**	7.18	7.10	7.09	**7.07**
Si+Mg+Fe	3.87	3.52	3.32	**3.52**	3.98	3.75	3.46	**3.75**
VI	2.02	2.02	2.04	**2.02**	2.03	2.03	2.04	**2.03**
VIII	0.85	0.84	0.83	**0.86**	0.85	0.90	0.93	**0.87**

2.8 Figures

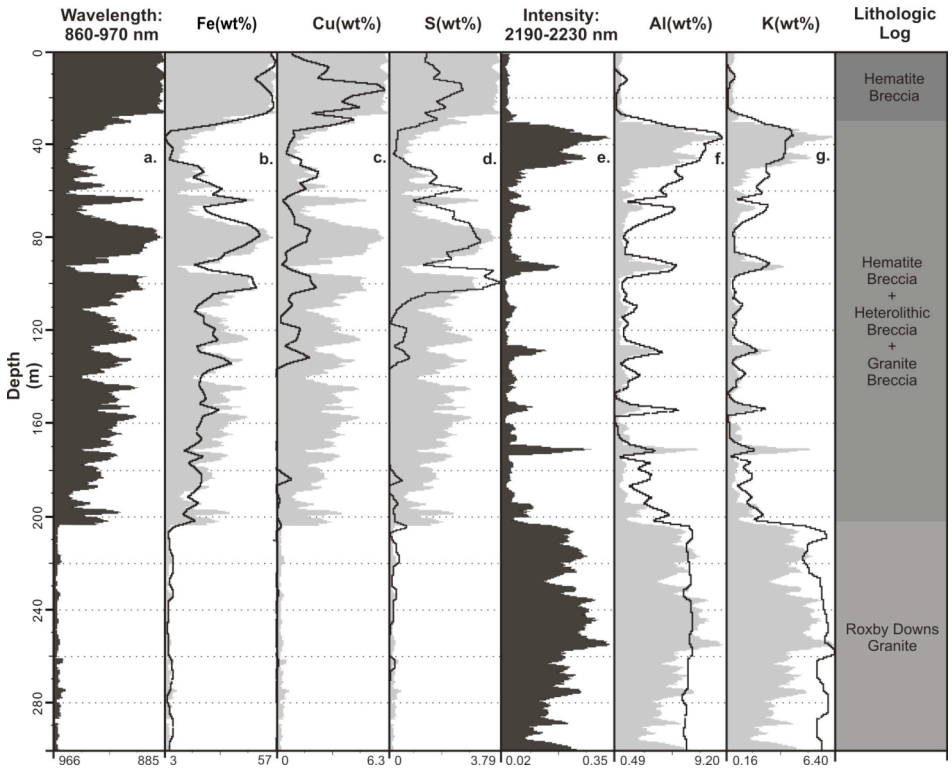

Figure 2-1. Depth profile: (a) The wavelength position of the largest absorption feature between 850 and 970 nm compared to the whole rock geochemistry results for (b) iron, (c) copper, and (d) sulfur. (e) The intensity of the largest spectral feature between 2,190 and 2,230 nm compared to the whole rock geochemistry results for (f) aluminum, and (g) potassium.

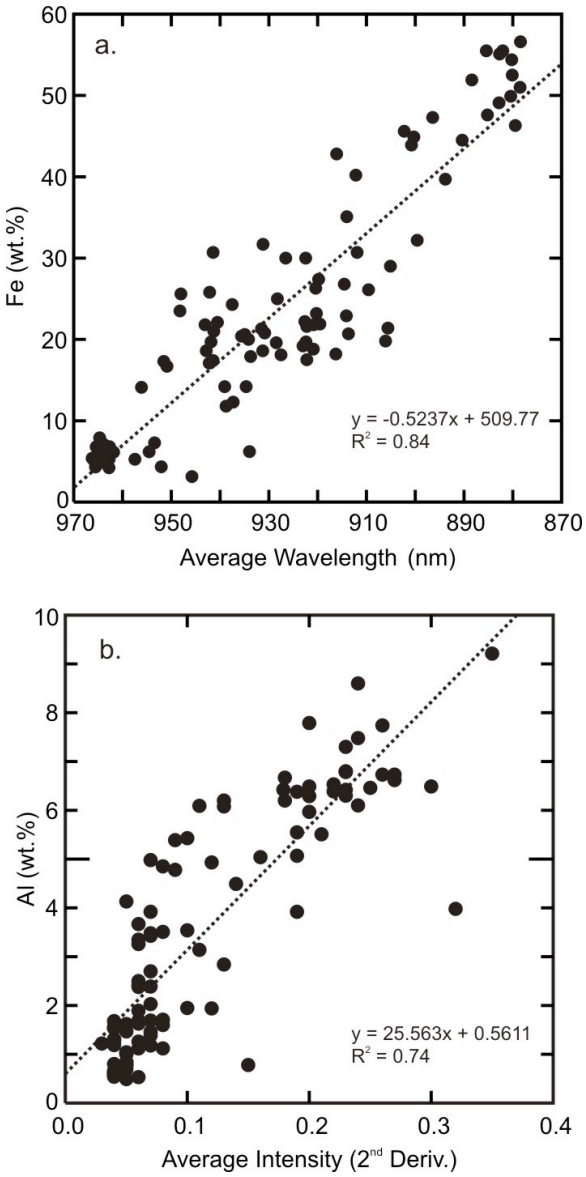

Figure 2-2. Plots showing the relationship between the calculations performed on the absorption features (averaged over 2.5 and 5 meter intervals) and the results from the geochemical analysis. (a) Average wavelength position of the largest absorption feature between 850 and 970 nm versus iron content. (b) Average intensity of the absorption feature between 2,190 and 2,230 nm versus aluminum content. Trend lines and R^2-values are provided for comparison.

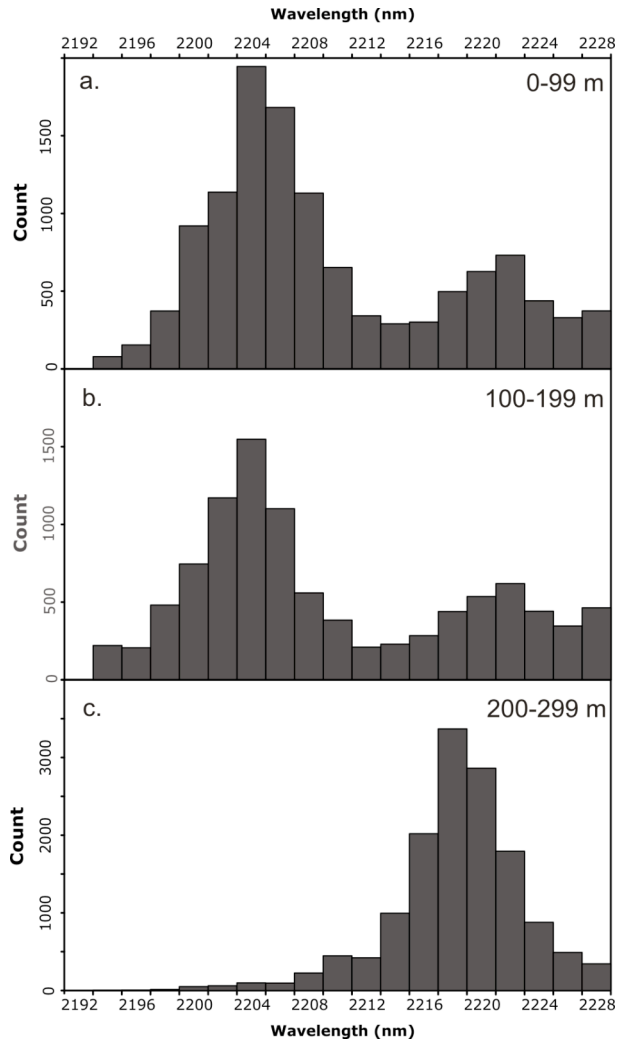

Figure 2-3. Histogram showing the wavelength position of the most intense absorption features between 2,190 and 2,230 nm at 100-meter depth intervals.

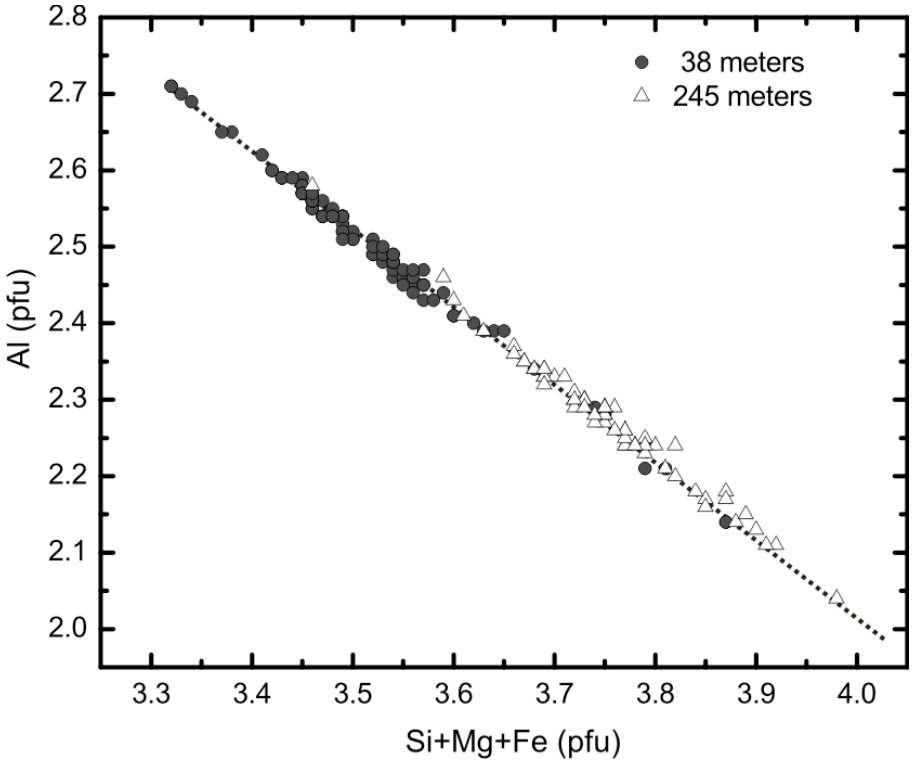

Figure 2-4. Composition of phengites at ~38 (n = 102) and ~245 meters (n = 62). The cations were calculated using 11 oxygens.

2.9 References

Adams, J.B. (1968) Lunar and Martian surfaces: petrologic significance of absorption bands in the near-infrared. Science, 159(3822), 1,453-1,455.

Berman, M. (2006) Some unmixing problems and algorithms in spectroscopy and hyperspectral imaging. 35th Applied Imagery and Pattern Recognition Workshop (AIPR'06), p. 15.

Burns, R.G. (1993) Mineralogical applications of crystal field theory. 551 p. Cambridge University Press, Cambridge.

Cibin, G., Cinque, G., Marcelli, A., Mottana, A., and Sassi, R. (2008) The octahedral sheet of metamorphic $2M_1$-phengites: a combined EMPA and AXANES study. American Mineralogist, 93, 414-425.

Clark, R.N. (1999) Spectroscopy of rocks and minerals, and principles of spectroscopy. In A.N. Rencz, Ed. Manual of Remote Sensing, Volume 3, Remote Sensing for the Earth Sciences, p. 3-58. John Wiley and Sons, New York.

Clark, R.N., King, T.V.V., Klejwa, M., and Swayze, G.A. (1990) High spectral resolution reflectance spectroscopy of minerals. Journal of Geophysical Research, 95(B8), 12,653-12,680.

Cornell, R.M., and Schwertmann, U. (2003) The iron oxides. 664 p. VCH Verlag, Weinheim.

Cross, K.C., Daly, S.J., and Flint, R.B. (1993) Mineralisation associated with the GRV and the Hiltaba suite granitoids. In J.F. Drexel, W.V. Preiss, and A.J. Parker, Eds. The geology of South Australia, 1: The Precambrian, p.

132-137. Geological Survey of South Australia, Adelaide, South Australia.

Cudahy, T.J., and Ramanaidou, E.R. (1997) Measurement of the hematite:goethite ratio using field visible and near-infrared reflectance spectrometry in channel iron deposits, Western Australia. Australian Journal of Earth Sciences, 44(4), 411-420.

Duke, E.F. (1994) Near infrared spectra of muscovite, Tschermak substitution, and metamorphic reaction progress: Implications for remote sensing. Geology, 22, 621-624.

Gallie, A., McArdle, S., Rivard, B., and Francis, H. (2002) Estimating sulphide ore grade in broken rock using visible/infrared hyperspectral reflectance spectra. International Journal of Remote Sensing, 23(11), 2,229-2,246.

Hauck, S.A. (1990) Petrogenesis and tectonic setting of middle Proterozoic iron oxide-rich ore deposits—and ore deposit model for Olympic Dam-type mineralization, 1932, p. 4-39. U.S. Geological Survey Bulletin.

Haynes, D.W., Cross, K.C., Bills, R.T., and Reed, M.H. (1995) Olympic Dam ore genesis: a fluid-mixing model. Economic Geology, 90, 281-307.

Hitzman, M.W., Orekes, N., and Einaudi, M.T. (1992) Geological characteristics and tectonic settings of Proterozoic iron oxide (Cu-U-Au-REE) deposits. Precambrian Research, 58, 241-287.

Hunt, G.R. (1977) Spectral signatures of particulate materials in the visible and near infrared. Geophysics, 42(3), 501-513.

Hunt, G.R. (1979) Near-infrared (1.3-2.4 um) spectra of alteration minerals—potential for use in remote sensing. Geophysics, 44(12), 1,979-1,986.

Hunt, G.R., and Ashley, R.P. (1979) Spectra of altered rocks in the visible and near infrared. Economic Geology, 74, 1,613-1,629.

Hunt, G.R., and Salisbury, J.W. (1970) Visible and near-infrared spectra of minerals and rocks: I Silicate minerals. Modern Geology, 1, 283-300.

Huntington, J.F., Mauger, A.J., Skirrow, R.G., Bastrakov, E.N., Connor, P., Mason, P., Keeling, J.L., Coward, D.A., Berman, M., Phillips, R., Whitbourn, L.B., and Heithersay, P.S. (2006) Automated mineralogical core logging at Emmie Bluff iron oxide-copper-gold prospect. MESA Journal, 41, 38-44.

Keeling, J.L., Mauger, A.J., and Huntington, J.F. (2004) Spectral core logger update—preliminary results from the Barns gold prospect. MESA Journal, 33, 32-36.

Kupsch, B.G., and Catuneanu, O. (2007) Alteration features and geochemical signatures of the Maybelle River uranium zone, Athabasca Basin, Alberta. In C.W. Jefferson, and G. Delaney, Eds. EXTECH IV: Geology and Uranium EXploration TECHnology of the Proterozoic Athabasca Basin, Saskatchewan and Alberta, p. 347-361.

Lyon, R.J.P. (1964) Evaluation of infrared spectrophotometry for compositional analysis of lunar and planetary soils. Part II: Rough and powdered surfaces. 262 p. NASA-CF-100, Washington, D.C.

Mauger, A., Keeling, J.L., and Huntington, J.F. (2007) Alteration mapping of the Tarcoola Goldfield (South Australia) using a suite of hyperspectral methods. Applied Earth Science, 116(1), 2-12.

Morris, R.V., Lauer Jr., H.V., Lawson, C.A., Gibson Jr., E.K., Nace, G.A., and Stewart, C. (1985) Spectral and other physicochemical properties of submicron powders of hematite (α-Fe_2O_3), maghemite (γ-Fe_2O_3), magnetite (Fe_3O_4), goethite (α-FeOOH), and lepidocrocite (γ-FeOOH). Journal of Geophysical Research, 90, 3,126–3,144.

Oreskes, N., and Einaudi, M.T. (1992) Origin of hydrothermal fluids at Olympic Dam: preliminary results from fluid inclusions and stable isotopes. Economic Geology, 87, 64-90.

Post, J.L., and Noble, P.N. (1993) The near-infrared combination band frequencies of dioctahedral smectites, micas, and illites Clay and Clay Minerals, 41(4), 639-644.

Reeve, J.S., Cross, K.C., Smith, R.N., and Oreskes, N. (1990) Olympic Dam copper-uranium-gold-silver deposit. In F.E. Hughes, Ed. Geology of the Mineral Deposits of Australia and Papua New Guinea, 2, p. 1,009-1,035. The Australasian Institute of Mining and Metallurgy, Melbourne.

Rieder, M. (1998) Nomenclature of the micas. The Canadian Mineralogist, 36, 905-912.

Roberts, D.E., and Hudson, G.R.T. (1983) The Olympic Dam copper-uranium-gold deposit, Roxby Downs, South Australia. Economic Geology, 78(5), 799-822.

Schaller, W.T. (1950) An interpretation of the composition of high-silica sericites. Mineral Magazine, 29, 406-415.

Sherman, D.M., Burns, R.G., and Burns, V.M. (1982) Spectral characteristics of the iron oxides with application to the martian bright region mineralogy. Journal of Geophysical Research, 87, 10,169-10,180.

Swayze, G.A., Clark, R.N., Kruse, F., Sutley, S., and Gallagher, A. (1992) Ground-truthing AVIRIS mineral mapping at Cuprite, Nevada. Summaries of the Third Annual JPL Airborne Geoscience Workshop, Volume 1: AVIRIS Workshop, p. 47-49. JPL Publications.

Velde, B. (1965) Phengite micas: synthesis, stability, and natural occurrence. American Journal of Science, 263, 886-913.

White, W.B., and Keester, K.L. (1966) Optical absorption spectra of iron in the rock-forming silicates. American Mineralogist, 51, 774-791.

Yang, K., Huntington, J.F., Cudahy, T.J., Mason, P., and Scott, K.M. (2001) Spectrally mapping the compositional variation of white micas in hydrothermal systems and the application in mineral exploration. Geoscience and Remote Sensing Symposium, 2001, 7, p. 3294-3296. IGARSS '01. IEEE 2001 International, Sydney, NSW, Australia.

Chapter 3: The mineral chemistry, near-infrared, and mid-infrared reflectance spectroscopy of phengite from the Olympic Dam IOCG deposit, South Australia

3.1 Introduction

Mica formation in hydrothermal ore deposits is controlled by the composition of the mineralizing fluids, the bulk-rock chemistry, and the pressure-temperature conditions of formation (Hemley and Jones, 1964; Meunier and Velde, 1982; Bishop and Bird, 1987; Eberl et al., 1987; Hitzman et al., 1992). As a result, a wide range of micas are associated with hydrothermal ore deposits, including muscovite, paragonite, illite, the mixed-layer illites/smectites (I/S), and phengite (e.g., Heinrich et al. 1953). Although phengite is widely known as a metamorphic mineral (e.g., Ernst, 1963; Crowley and Roy, 1964; Velde, 1965; Velde, 1967; Frey, 1983; Massonne and Schreyer, 1987; Shau et al., 1991; Gouzu et al., 2005; Cibin et al., 2008), it is also a common product of hydrothermal alteration (Velde, 1965; Roberts and Hudson, 1983). Phengite is the main potassic dioctahedral mica at the iron oxide-copper-gold (IOCG) deposit at Olympic Dam, South Australia—which is the largest known IOCG deposit and one of the largest polymineralic ore deposits in the world (e.g., Roberts and Hudson, 1983; Hitzman et al., 1992; Haynes et al., 1995). Consequently, the study of phengite, its mineral

chemistry, and its near- and mid-infrared spectroscopy is important to those who want to identify additional IOCG deposits like Olympic Dam.

At Olympic Dam, phengite is found within the brecciated, intensely altered, ore-bearing lithologies and in the unbrecciated, less-altered, barren rocks that surround the deposit (Roberts and Hudson, 1983). Despite its ubiquitous presence, little information is available about the composition of phengite or how it can be detected using near- or mid-infrared reflectance spectroscopy at Olympic Dam. This information is valuable because phengite can be used as a marker mineral to identify rocks that have been altered by hydrothermal fluids, and the identification of altered rocks is typically the prime objective in many base metal exploration programs.

In this paper, we examine how phengite can be distinguished from other micas, such as muscovite and celadonite, using quantitative compositional data from electron probe micro analyses. In addition, we examine the different types of phengite at Olympic Dam, and demonstrate how near-infrared and mid-infrared reflectance spectroscopy can be used to identify, characterize, and quantify phengite in drill core and hand samples. Tappert et al. (2011) showed that reflectance spectroscopy can be used to identify zones of hydrothermal alteration at Olympic Dam. Based on this work, we now expand upon the spectral ranges and address the mineralogical causes of the different types of phengites observed at Olympic Dam. In summary, we provide the information required to effectively detect the presence of phengite spectroscopically and mineralogically.

3.2 Background

3.2.1 Phengite Mineral Chemistry

Compositionally, phengite can be distinguished from muscovite by a higher silicon, iron, and magnesium content, and a lower aluminum content (Winchell, 1927; Pauling, 1930; Schaller, 1950; Foster, 1956; Velde, 1965; Ogorodova et al., 2006). According to Rieder et al. (1998), the phengite series includes the potassic dioctahedral micas that fall compositionally between, or close to, the joins of muscovite-aluminoceladonite and muscovite-celadonite. This definition by Rieder et al. (1998), however, does not address the presence of iron in phengite, which substitutes readily for magnesium. To account for the presence of iron in phengite, we have devised a ternary diagram with three endmembers: muscovite ($[K(Al_2)AlSi_3O_{10}(OH)_2]_2$), and the two hypothetical end members $[KFe_2Si_4O_{10}(OH)_2]_2$ and $[KMg_2Si_4O_{10}(OH)_2]_2$ (Figure 3-1). This ternary diagram shows the location of the phengite series in relation to muscovite and the celadonite series, taking into consideration the magnesium-number (Mg-number) of the mineral.

The relationship between the three endmembers is defined by the coupled heterovalent Tschermak substitution of $Al^{VI}Al^{IV} \leftrightarrow Mg^{VI}Si^{IV}$, and $Fe \leftrightarrow Mg$. The substitution of magnesium and iron for aluminum in the octahedral sites produces a layer charge, which facilitates the incorporation of silicon into more tetrahedral sites (Figure 3-2) (Foster, 1956; Brigatti et al, 1998; Schmidt, 2001; Gouzu et al., 2005). Muscovite contains between 3.0 and 3.1 cations of silicon per formula unit (p.f.u.) calculated using 11 oxygens (Rieder et al., 1998). Minerals belonging to

the celadonite series typically have between 3.5 and 4.0 cations of silicon p.f.u. (e.g., Hendricks and Ross, 1941; Li et al., 1997). Potassic dioctahedral micas located between these two extremes—3.1 to 3.5 cations silicon p.f.u.—fall into the phengite series.

3.2.2 Reflectance Spectroscopy

The potassic dioctahedral micas produce a spectral absorption feature—which is observed as a trough in reflectance spectra—between 2.195 and 2.225 μm. This trough is due to the presence of hydroxyl bound to aluminum (Al-OH) in the octahedral layer (Figure 3-2), and it is produced by the combination of the O-H stretch with the fundamental Al-O-H bending mode (Vedder, 1964; Hunt, 1977; Clark et al., 1990). The position of this trough is dependent on mineral chemistry, and it has typically been documented between 2.195 and 2.215 μm for muscovite and between 2.215 and 2.220 μm for phengite (e.g., Hunt and Salisbury, 1970; Hunt, 1979; Duke, 1994; Clark, 1999).

This shift in trough position is caused by changes in the Al-OH bond strength, which is governed by the amount of aluminum contained within octahedral sites (Figure 3-1). More aluminum in the octahedral sites produces a spectral feature at shorter wavelengths (Swayze et al., 1992; Post and Noble, 1993; Longhi et al., 2000; Duke and Lewis, 2010). Conversely, as the celadonite component of the mineral increases (i.e., less aluminum in octahedral sites), this trough shifts to longer wavelengths.

In addition, the intensity of the Al-OH trough is related to the number of Al-OH bonds (Clark, 1999). As a result, the intensity of the Al-OH spectral

feature can be used to quantify the amount of mica and/or aluminum present in metamorphic rocks (van Ruitenbeek et al., 2006) and in hydrothermally altered rocks (Tappert et al., 2011).

Muscovite and phengite also produce spectral features between 6 and 15 μm (Farmer, 1974; Moenke, 1974; Eberl et al., 1987). Intense peaks between 8 and 10 μm are attributed to the fundamental asymmetric stretch of the Si-O bonds in tetrahedral sites (Vedder, 1964). These peaks are sensitive to the substitution of differently charged ions, and the substitution of Al^{3+} for Si^{4+} in tetrahedral sites will shift these peaks towards longer wavelengths, regardless of the ions present in octahedral sites (Lyon et al., 1959; Stubican and Roy, 1961).

A weak peak is also observed between 10.6 and 11.0 μm in the spectra of some dioctahedral micas, which is caused by the OH liberation motion. The OH liberation motion for micas can be described as the movement of the OH ion proton in the octahedrally bound Al-OH groups parallel to the mica cleavage plane (Vedder and McDonald, 1963; Vedder, 1964; Beran, 2002). This peak is sensitive to the substitution of divalent cations (e.g., Mg^{2+} or Fe^{2+}) for aluminum in octahedral sites. An increase in the divalent ion content, which would correspond to a decrease in aluminum content, will decrease the intensity of this peak. Additional weak peaks between 11.0 and 13.0 μm are also present, and they relate to the Al/Si ratio in the tetrahedral sites and the amount of aluminum in octahedral sites (Stubican and Roy, 1961; Farmer and Russell, 1964; Franz et al., 1977; Beran, 2002). As the aluminum content in tetrahedra and/or octahedral sites of the phengite increases, the intensity of these spectral features will also increase.

3.3 Site, Samples, and Methods

The rocks investigated for this study originate from the Olympic Dam iron oxide-copper-gold (IOCG) deposit at Roxby Downs, South Australia, which is located ~560 km northeast of Adelaide. Worldwide, IOCG deposits are found in a range of rocks, but many Proterozoic deposits, such as Olympic Dam, are found within granitoids (Davidson and Large, 1998). Regardless of the age of the deposit, most investigators agree that IOCG formation is the product of hydrothermal fluids using faults and/or shear zones as conduits (e.g. O'Driscoll, 1985). These structural lineaments have been observed in extension or neutral settings, and they have also been identified in compressional settings (e.g. Dirreen and Lyons, 2007).

On a regional or a cratonic scale, it has been noted that IOCG deposits are often found in groups, and they are commonly associated with other types of hydrothermal ore deposits (e.g., gold deposits). A number of sub-economic and potentially economic IOCG deposits of similar geologic age have been found on the Gawler Craton close to Olympic Dam (e.g., Prominent Hill, Carrapateena, Murdie-Murdi, Titan, Emmie-Bluff, Torrens Dam, etc.), including the nearby Tarcoola goldfields (Blastrakov et al., 2007; Budd and Skirrow, 2007; Davidson, et al., 2007). The crystallization age of the Roxby Downs Granite, which hosts the Olympic Dam deposit, is 1,588 ± 4 Ma, and this places a limit on the oldest age of the Olympic Dam deposit (Creaser and Cooper, 1993). At nearby Prominent Hill, mineralization occurred at a similar age (~1,585 Ma) (Belperio et al., 2007). The spatial and temporal relationship between these deposits is likely related to the

formation of the rocks of the Gawler Craton (Johnson and McCulloch, 1995). The presence of barren and sub-economic deposits, however, might represent a fundamental difference in the manner in which these deposits formed, or it might represent a lack of metal sources (e.g. sulphur) at certain localities.

It has been postulated that the intensely brecciated Olympic Dam IOCG deposit was formed by repetitive explosive hydrothermal activity in a near-surface environment (Gow et al., 1994; Haynes et al., 1995; Davidson and Large, 1998; Pollard, 2000; Williams et al., 2005; Belperio et al., 2007). Most likely, the deposit was formed by an initial high temperature (~400°C) reduced hydrothermal fluid, which precipitated magnetite, and then this magnetite was completely altered by a lower temperature (200-400°C) oxidized hydrothermal fluid to produce hematite (Oreskes and Einaudi, 1992; Gow et al., 1994; Williams et al., 2005; Belperio et al., 2007).

It is difficult to observe magnetite at Olympic Dam because the entire deposit has sustained extensive hematitic alteration (Gow et al., 1994). Any magnetite present is not found in association with ore minerals, but all of the copper-, uranium-, and rare-earth element (REE)-bearing minerals are found within the hematitic-bearing rocks. The formation of REE-enriched hematite phases at Olympic Dam was likely caused by the transport and circulation of hydrothermal fluids (Oreskes and Einaudi, 1990). Texturally, much of the copper sulphide mineralization either post-dates or is coeval with coexisting hematite (Cross et al., 1993).

The exact fluid conditions leading to the formation of the deposit are not

well constrained because few primary fluid inclusions were preserved, but the source of the reduced fluids likely had a magmatic origin, whereas the oxidized fluids were likely derived from non-magmatic sources; in addition, the source of copper and other metals has been shown to be partly external to the host rock, and their deposition involved mantle-derived rocks and magmas (Haynes et al., 1995; Johnson and McCulloch, 1995). Sulfur isotope data are consistent with a magmatic sulfur component at Olympic Dam (Hauck, 1990), but the nearby sub-economic IOCG deposits indicate a recycling of metals and sulfur from local host rocks, with limited or no input from mantle-derived sources (Skirrow et al., 2007).

A zone of quartz breccias form the core of the Olympic Dam complex, and all of the known copper and uranium mineralization occurs outside this zone in the intermingled hematite-rich and altered granite breccias that flank this inner core (Cross et al., 1993). Due to gradational boundaries between units, and the diverse range of mineral assemblages and textures, it is difficult to identify and map the breccias in this zone. Around the outer limits of this zone, there is a ~3km alteration halo comprised of brecciated or un-brecciated altered Roxby Downs Granite. In general, it is the intense alteration observed in the country rocks that distinguishes IOCG deposits from other ore deposits, like porphyry Cu systems.

The major alteration phases at Olympic Dam are hematite, sericite, chlorite, and silica (Reeve et al., 1990). Silicic alteration occurrs locally in discrete zones of the hematite-quartz breccias. Chloritic alteration is sporadic but widespread, and it is more intense at depth. It generally only occurs at a low to

moderate intensity. Hematitic alteration is very widespread and most intense towards the center of the deposit. Sericitic alteration—where phengite is the main mineral byproduct—is also very widespread; however, it is particularly intense in the granite breccias. Most of the granite-rich breccias and the granite clasts in the hematite-rich breccias exhibit some hydrothermal alteration of feldspar to phengite, and some feldspar grains may be entirely pseudomorphed, but the alteration of the matrix is generally more intense than that of the clasts (Reeve et al., 1990).

Hitzman et al. (1992) refers to the alteration of IOCG deposits as metasomatism, where the alteration mineralogy is controlled by the bulk-rock chemistry, the compositions of the mineralizing fluids, and the P-T conditions of formation. On the Gawler Craton, the smaller IOCG deposits are less brecciated, they have different sulfur, oxygen, and neodymium isotope signatures, and they have a higher component from local host-rock sources (Bastrakov et al., 2007; Skirrow et al., 2007). The spatial and temporal association of other types of ore deposits with economic and barren Proterozoic IOCG deposits indicates that IOCG deposits are a hydrothermal expression of a regional event, with hematitic and sericitic hydrothermal alteration being the two most important markers of IOCG deposit formation.

In total, 300 m of drill core (RU39-5371) from Olympic Dam were examined. The drill core originates from the northern tip of the deposit, in GDA94/MGA zone 53, at 681181.62 easting and 6630999.9 northing. The drill core consists of three visibly distinct zones. From 0 to 30 meters, the drill core is

intensely brecciated and contains hematite breccias. The product of intense hematitic alteration, the hematite breccias are comprised of dull-red and specular hematite that forms both the clasts and the matrix. Quartz is present, in addition to chalcocite, bornite, uranium-bearing minerals, and REE-bearing minerals; yet, no phengite is present.

From 30 to 202 m, the drill core is intensely brecciated and contains complexly intermingled hematite breccias, hematite-rich breccias, and heterolithic breccias. Chalcocite, bornite, uranium-bearing minerals, and REE-bearing minerals are present. Chalcocite and bornite are the dominant Cu-Fe sulfides until 51 m depth, where chalcopyrite appears and becomes the most common Cu-Fe sulfides. Evidence of sericitic alteration is observed at ~30 m with the first appearance of phengite. A zone of strongly sericitically altered granite, which may represent a large country-rock clast of Roxby Downs Granite, is observed between ~35 and 40 m. Hematitic alteration is still widespread between 30-202 m, as demonstrated by the presence of the hematite and hematite-rich breccias. Weak chloritic alteration is observed in discrete locations, usually in conjunction with mafic intrusives or mafic clasts. Fluorite, barite, and carbonate are also minor phases in some lithologies.

From 202 to 300 m, the drill core contains the sericitically altered lithologies of the Roxby Downs Granite suite, which are weakly brecciated or unbrecciated. These barren rocks are mainly comprised of K-feldspar, quartz, phengite, and they also contain chlorite, carbonate, barite, fluorite, and minor hematite.

In total, 16 samples were collected from the drill core. Of these samples, five were collected from areas that had sustained sericitic alteration and contained phengite.

3.3.1 Petrography and Mineral Chemistry

We investigated the five phengite-bearing samples to conduct a detailed petrographic analysis and to determine the composition of the mineral components, focusing mainly on phengite: OD05 (38.8 m), OD12 (183.8 m), OD13 (206.5 m), OD14 (245.3 m), and OD15 (293.4 m). Compositional information was obtained from thin sections and thick sections (>300 μm) using a CAMECA SX-51 electron microprobe at the University of Adelaide, and a JEOL 8900R electron microprobe at the University of Frankfurt and the University of Alberta.

The microprobe data were collected in such a manner that minerals belonging to the phengite series—which were first identified in the preliminary microprobe sessions by their mineral chemistry, backscattered-electron image contrast, and texture—were specifically sought out and analyzed in later sessions. The final analyses focused exclusively on phengite grains > 2 μm in size. The measurements were collected using a 15 kV accelerating voltage, a 15 to 20 nA probe current, and a 1 micron beam diameter. Peak and backgrounds count times varied between 15 to 40 seconds. Natural standards were used, which were measured before the beginning of each experiment. The instrument calibration was deemed successful when the composition of secondary standards was reproduced within the error margins defined by the counting statistics. The data

presented herein include the data presented in Tappert et al. (2011) from OD05 and OD14, and over 300 new measurements from OD05, OD12, OD13, OD14 and OD15. The cations for each phengite analysis were calculated using 11 oxygens.

3.3.2 Instrumentation and Analysis

Visible and near-infrared reflectance spectra were collected from the drill core using the HyLogger 2 instrument (0.4-2.5 μm) at the Glenside drill core library, Adelaide (Mason and Huntington, 2010). Additional mid-infrared reflectance spectra were collected from the five phengite-bearing samples using a Bomem MB100 Fourier Transform Infrared (FTIR) spectrometer (6-15.5 μm) and a Thermo Nicolet Nexus 470 FTIR instrument mounted with a Nicolet Continuum infrared microscope (2.5-15.5 μm) at the University of Alberta, Edmonton (Table 3-1).

3.3.2.1 HyLogger 2

The HyLogger 2 collected visible and near-infrared reflectance spectra (0.4-2.5 μm) from the surface of drill core RU39-5371 with the drill core in its core tray. The instrument collected spectra continuously, and the translation table holding the core box moved at a rate of 48 mm/s. When the instrument is operated at its standard speed, twelve spectra can be collected each second, and ~600 m of drill core can be scanned in an eight hour day. The HyLogger 2 instrument collected a measurement from the surface of the intact drill core every 4 mm. To improve the signal-to-noise ratio, measurements were averaged, and the actual

area covered by a single output spectrum was about 18 mm in length and 8 mm in width (Mason and Huntington, 2010). Spectra were output at 8 mm intervals, resulting in ~125 spectra for each meter of drill core. The two spectrometers mounted on HyLogger 2 have a spectral resolution ranging from 1.4 to 9 nm. The spectra were re-sampled to have a 4 nm spectral resolution.

The bidirectional spectra were measured in uncalibrated radiance and were converted into absolute reflectance using three standards: 'dark' shutter-closed spectra, spectra of the light source from a Teflon transfer standard, and an external standard Spectralon calibration file. Digital color pictures were taken of the drill core using a Basler piA1900-32gc line-scan camera. A continuous image of the drill core was then constructed by stitching together individual images. In addition to photographing the drill core, the HyLogger 2 instrument measures the distance of the spectrometer to the drill core using a profilometer. This information is used for identifying sections along the core tray where drill core is absent.

The analysis of the HyLogger 2 dataset focused on the wavelength region between 2.190 and 2.230 μm, where two calculations were performed. The first calculation was conducted using the reflectance spectrum with the continuum removed according to the hull correction procedure described in Berman (2006). After the continuum was removed, the wavelength position of the most intense trough between 2.190 and 2.230 μm was identified. The second calculation used the second derivative spectrum, and the maximum value between 2.190 and 2.230 μm was identified. The usefulness of the second derivative spectrum in measuring

the intensity of spectral features is presented in Huguenin and Jones (1986), Farrington et al. (1994), Ben-Dor et al. (1997), and Feng et al. (2004). If no spectral feature was present in this wavelength range, no values were produced for these calculations. Depth profiles were constructed using the results of these two calculations, and to remove some of the variability in the data, the results were smoothed as a function of depth using a moving average window that encompassed 50 spectra.

3.3.2.2 Bomem MB100 Fourier Transform Infrared (FTIR) Spectrometer

Mid-infrared reflectance spectra were collected from cut surfaces of phengite-bearing hand samples using a Bomem MB100 Fourier Transform Infrared (FTIR) spectrometer. The spectrometer operates with a similar field-of-view (8 x 8 mm) as HyLogger 2, yet it collects spectral data between 2.5 and 22 µm. Much of the spectral data collected between 2.5 and 6 µm, and 14 and 22 µm lacked specific spectral detail for these samples, and, therefore, the subsequent analysis was focused on the wavelengths between 6 and 14 µm.

Bidirectional reflectance measurements were collected using a globar light source and a viewing angle of 35°. Spectra were collected at a spectral resolution of 8 cm^{-1}, and sixty-four scans were averaged at each location using a gold standard for computation of reflectance. In total, 5 to 10 spectra were collected from each of the five phengite-bearing samples. Each spectrum was examined individually to identify the presence of common and well-known spectral features associated with quartz, feldspar, phengite, and chlorite.

3.3.2.3 Thermo Nicolet Nexus 470 FTIR and Nicolet Continuum Infrared Microscope

Additional mid-infrared reflectance spectra were obtained from the five phengite-bearing samples. These reflectance spectra were collected from the surface of polished thick sections (>300 μm) using a Thermo Nicolet Nexus 470 FTIR instrument mounted with a Nicolet Continuum infrared microscope (Micro-FTIR). Similar to HyLogger 2, the Micro-FTIR can collect reflectance spectra in an automated manner. The Micro-FTIR collected spectral data between 2.5 and 15.3 μm, but only the data between 6 and 14 μm contained enough spectral detail to conduct a suitable analysis. The Nicolet Continuum infrared microscope allows spectra to be collected over a much smaller field-of-view (100 x 100 μm) compared to the Bomem FTIR (8 x 8 mm).

For each of the five phengite-bearing samples, 625 reflectance spectra were collected over an area of 1.2 x 1.2 cm in a grid configuration—25 rows x 25 columns—with 500 μm separating each line in the grid. Twenty scans were averaged per spectrum, which were collected with a spectral resolution of 4 cm^{-1}. The spectra were collected in radiance and were converted into reflectance using a gold standard.

Phengite-bearing spectra were identified in the dataset by the presence of a spectral feature at ~9.6 μm. The spectra of pure phengite were identified by masking all spectra containing the spectral features of quartz, feldspar, chlorite, hematite, and the sulfide-bearing minerals. The remaining spectra were then visually examined to confirm that they were solely a product of phengite. The

mid-infrared reflectance spectrum of phengite shares many similarities with the reflectance spectra of muscovite and chlorite. Muscovite has two peaks at approximately 8.9 and 9.6 μm. whereas phengite only has one intense peak at ~9.6 μm, which is distinct from the most intense peak of chlorite, which is observed at 9.7 μm (Figure 3-3).

3.4 Results

The thin sections from the five selected phengite-bearing samples show visible differences in composition and texture (Figure 3-4). The two samples collected from the ore-bearing, brecciated zone (OD05 and OD12) have been completely transformed by sericitic alteration—and as a consequence, any type of feldspar is absent (Figure 3-4A, 3-4B). The three samples from the unbrecciated, barren Roxby Downs Granite (OD13, OD14, OD15) also show evidence of sericite alteration but to a lesser extent (Figure 3-4C, 3-4D, 3-4E). In these sections, some of the primary K-feldspar is preserved, and phengite occurs at the rims of the larger K-feldspar grains, and also replaces all plagioclase grains and some small K-feldspar grains.

3.4.1 Phengite Composition

The potassic dioctahedral micas from the Olympic Dam deposit have the following abundance ranges for the major elements: 45.3-54.0 wt% SiO_2, 25.7-35.1 wt% Al_2O_3, 2.1-7.2 wt% FeO, 0.1-3.4 wt% MgO, and 8.2-11.0 wt% K_2O (Table 3-2, 3-3). These ranges conform well to the phengite data published in

Roberts and Hudson (1983): 50.1 wt% SiO_2, 31.2 wt% Al_2O_3, 3.7 wt% FeO, 0.6 wt% MgO, and 10.2 wt%.

The average number of silicon cations per formula unit ranges from 3.3 to 3.4. This range is too high to classify these micas as muscovite, and it is also too low—with the exception of a few measurements—to classify them as celadonite. These findings are well illustrated using a ternary diagram that relates the mineral chemistry of the micas to celadonite substitution and their Mg-number (Figure 3-1, 3-5). The micas from Olympic Dam plot entirely within the phengite series where they form two distinct clusters: phengites from OD05 and OD12 (i.e., the brecciated, ore-bearing zone) have a lower Mg-number, and they are Al-rich and Si-poor. In contrast, phengites from OD13, OD14, and OD15 (i.e., the unbrecciated, barren Roxby Downs Granite) have a higher Mg-number, and they are Al-poor and Si-rich.

These two groups of phengites can also be observed by plotting the total Al cations per formula unit (p.f.u.) against the summed total of the Si + Mg + Fe cations (Figure 3-6). The data define a linear array, which presumably reflects Tschermak substitution (i.e., silicon, iron, and magnesium substituting for aluminum). In this case, phengites from the brecciated rocks plot towards higher Al values and lower Si + Mg + Fe values. Conversely, phengites from the unbrecciated rocks plot towards lower Al values and higher Si + Mg + Fe values.

It is notable that there is some scatter in the data, particularly for the data plotting at higher Si + Mg + Fe values (Figure 3-6). This scatter is likely due to the presence of ferric iron (Fe^{3+}), which substitutes for aluminum and/or silicon in

the tetrahedral sites (Cardile, 1989; Besson and Drits, 1997). In our cation calculations, we have assumed that all of the iron in phengite is ferrous (Fe^{2+}). In reality, ferric iron (Fe^{3+}) can also be present, which means that errors can arise when calculating the mineral chemistry of ferric iron-bearing minerals (Guidotti et al., 1994; Longhi et al., 2000). As a result, phengites that contain a high Fe^{3+} content will plot above the general trend in Figure 3-6 (Gouzu et al., 2005).

The compositional cutoff between these two groups was determined by examining the distribution of aluminum cations within each group. For OD05 and OD12, the average aluminum cation values were 2.49 ($\delta = 0.11$). For OD13, OD14, and OD15, the average aluminum cation values were 2.30 ($\delta = 0.06$), 2.28 ($\delta = 0.09$), and 2.29 ($\delta = 0.06$), respectively. The boundary between these two groups is visually estimated to be 2.37 aluminum cations p.f.u..

The substitution of silicon, magnesium, and iron for aluminum in phengite can be quantified by dividing the summed value of the Si + Mg + Fe cations by the total Al cations, and we refer to the result as the substitution index. Muscovite with a chemical formula of $[K(Al_2)AlSi_3O_{10}(OH)_2]_2$ has a substitution index of 1. Values >1 indicate an increased celadonite component. Phengite in the brecciated, ore-bearing zones has an average substitution index between 1.42 and 1.43, whereas phengite in the Roxby Downs Granite has an average substitution index between 1.63 and 1.65 (Figure 3-7). Quantile-quantile plots reveal that each sample displays a range of values centered on the mean with some skewing. For OD05 and OD12, most of the data are centered around 1.42 or 1.43, but the data are positively skewed. In addition, there is a small population at 1.64, which

corresponds to the data centered around the means at 1.63 and 1.65 for sample OD13, OD14, and OD15. In addition, these samples are negatively skewed, with small populations of data between 1.30 and 1.40.

Three important observations can be drawn from the compositional data obtained from the micas at Olympic Dam: (1) they plot within the phengite series, (2) the phengites fall into two distinct compositional groups, and (3) each of these two populations has compositional outliers that resemble the phengites from the other group.

3.4.2 Near-IR Reflectance Spectroscopy

In total, 41,700 reflectance spectra were collected from the Olympic Dam drill core using HyLogger 2. Phengite was identified by the presence of a trough between 2.190 and 2.230 μm. In total, 32,728 spectra (78%) possessed a trough in this wavelength range. Along the length of the drill core, the position of the trough was variable (Figure 3-8). In the brecciated, ore-bearing zone (0-202 m), the average trough position for phengite was 2.206 μm; in the Roxby Downs Granite (202-300 m), however, the average trough position was 2.213 μm (Figure 3-9). Quantile-quantile plots show that both populations are comprised of a single population with a normal distribution.

The trough position of this spectral feature is controlled by the amount of aluminum bound to hydroxyl (Al-OH) in the octahedral sites (Figure 3-2). Substituting silicon for aluminum in the octahedral sites weakens the bond strength for the remaining Al-OH bonds, which shifts the position of this trough to longer wavelengths (e.g., Swayze et al., 1992; Longhi et al., 2000; Post and

Noble, 1993). Based on the mineral chemistry results (Table 3-2, 3-3), all of the potassic dioctahedral micas from Olympic Dam were identified as phengite (Figures 3-1, 3-5). Troughs observed at shorter wavelengths were produced by phengites that have a high abundance of aluminum in their octahedral sites (i.e., high-Al phengites), whereas phengites with a low abundance of aluminum in their octahedral sites (i.e., low-Al phengites) produce troughs at longer wavelength.

The interpretation of the spectroscopic data is consistent with the results of the microprobe data. In sections of the drill core where high-Al phengites were identified using infrared spectroscopy (e.g., OD05 and OD12) (e.g., Figure 3-8), high-Al phengites were also identified in the microprobe data (Figure 3-6, Table 3-2A). Conversely, samples that were located in sections of the drill core where low-Al phengites were identified using infrared spectroscopy (e.g., OD13, OD14, and OD15) also had low-Al phengites identified in the microprobe data.

It is widely accepted that muscovite is responsible for the absorption feature observed in near-infrared reflectance spectra between 2.195 and 2.210 μm (Hunt and Salisbury, 1970; Hunt, 1979; Hunt and Ashley, 1979; Duke, 1994; Clark, 1999). However, our data show that high-Al phengite can also absorb at these wavelengths. This overlap is presumably due to similarities in the crystallographic environment of the Al-OH bond in the octahedral sites of these two minerals.

The intensity of the Al-OH spectral feature was measured using the second derivative spectrum, and the results varied between -0.01 and 1.5 (Figure 3-8). Previously, Tappert et al. (2011) used the intensity of the Al-OH spectral

feature to identify phengite-bearing rocks in the drill core. They also established that a correlation between the intensity of the Al-OH spectral feature and the aluminum content (Al wt%) of the whole rock exists. It should be noted that this previous work was based on HyLogger data, which is of poorer quality than the HyLogger 2 data presented here. The spectra from HyLogger 2 contain more spectral information than those from HyLogger due to the improved setup and configuration of the HyLogger 2 instrument (e.g., 4 nm band spacing compared to 16 nm band spacing). As a result, very little smoothing or binning of the HyLogger 2 data is required and a more detailed depth profile, such as those showing the relative abundance of phengite can be produced (Figure 3-8).

Using the depth profile created by plotting the intensity of the Al-OH spectral feature, sections of the drill core that contain a high abundance of phengite can easily be identified. The phengite-poor sections are those where the second derivative intensities are near zero. The second derivative intensities increase with the amount of phengite present. The depth profile indicates that little phengite is present between 0 and 30 m, and most of the phengite is located between 202 and 300 m. Phengite-bearing rocks are also located between 30 and 50, 95, and 170 m, and many additional thin zones are located throughout the drill core between 30 and 202 m. With respect to phengite abundance, the results of the spectral analysis correspond closely with the results of the visual inspection.

3.4.3 Mid-Infrared Reflectance Spectroscopy

The reflectance spectra collected using the Bomem MB100 FTIR were obtained at five to ten discrete locations along the surface of each sample. As a

result, the heterogeneous distribution of minerals on the surface produced a unique reflectance spectrum at each location (Figure 3-10). Despite this variability, patterns are observed.

The spectra collected from samples OD05 and OD12 are dominated by quartz (Figure 3-10). A typical quartz spectrum has two large peaks at 8.5 and 9.0 μm, and two moderate peaks at 12.5 and 12.8 μm (e.g., Saksena, 1940; Simon and McMahon, 1953). The spectra from samples OD05 and OD12 have two moderate peaks at 12.5 and 12.8 μm, but the two larger peaks, which should be located at 8.5 and 9.0 μm, have been shifted to 8.2 and 9.2 μm. A very weak peak at 10.98 is also observed, which can be attributed to the presence of phengite. There is no evidence for the presence of feldspar in the spectra because feldspar produces distinct features between 8 and 15 μm, which are absent in these spectra (e.g., Laves and Hafner, 1962; Ishii et al., 1971; Christensen et al., 2000).

The spectra collected from samples OD13, OD14, and OD15 are much more variable than those collected from samples OD05 and OD12. The spectral features of quartz and K-feldspar dominate these spectra (Figure 3-10). Spectral features relating to the presence of phengite are not visible, which is consistent with a much lower abundance of phengite in these samples compared to OD05 and OD12.

To observe the characteristic spectral features of phengite, additional spectra were collected from individual phengite grains using a Thermo Nicolet Nexus 470 FTIR with a Nicolet Continuum infrared microscope (Micro-FTIR), which operates with a spatial resolution of 100 x 100 μm. In total, 625 spectra

were collected from each of the five phengite-bearing samples. Numerous spectra contained the spectral features of phengite in combination with one or two other minerals (e.g., quartz and/or K-feldspar), but only a small percentage of pure phengite spectra were obtained: OD05: 97 (16%); OD12: 15 (2%); OD13: 23 (4%); OD14: 11 (2%); and OD15: 9 (1%).

The reflectance spectrum of phengite between 6 and 14 μm is characterized by the presence of an intense peak at 9.59 μm (OD05 and OD12) or 9.57 μm (OD13, OD14, and OD15) (Figure 3-11). Three weaker, less defined peaks were also observed at 10.98, 12.22, and 13.40 μm. In addition, the Christiansen Feature (i.e., the wavelength at which the minimum reflectance occurs) was identified at 8.24 μm (OD05), 8.26 μm (OD12), 8.20 μm (OD13), 8.14 μm (OD14), and 8.14 μm (OD15). The Christiansen Feature is found at longer wavelengths in samples OD05 and OD12 compared to OD13, OD14, and OD15, which is consistent with a lower silicon content in the phengite from the ore-bearing zone (e.g., Logan et al., 1973; Salisbury and Walter, 1989).

The most intense peak in the reflectance spectrum of phengite is caused by Si-O stretching that occurs within the tetrahedral sites (Figure 3-2). This fundamental stretch primarily involves the displacement of the oxygen atoms, resulting in an asymmetric stretching mode (Vedder, 1964). This peak is located at 9.59 μm for the high-Al phengites (i.e., brecciated, ore-bearing zone), and at 9.57 μm for low-Al phengites (i.e., barren Roxby Downs Granite) (Figure 3-11, inset). The shift of this spectral feature by 0.02 μm between these two groups is due to differences in the amount of Al^{3+} that substitutes for Si^{4+} in the tetrahedral

sites. There is greater Al^{3+} substitution in the high-Al phengites, and this shifts this spectral feature to longer wavelengths (Lyon et al., 1959; Stubican and Roy, 1961).

The peak at 10.98 μm is the product of the Al-OH liberation motion, and any change in its intensity can be attributed to the substitution of Mg^{2+} and Fe^{2+} for Al^{3+} in octahedral sites, with more substitution of the divalent ions weakening the intensity of this spectral feature (Vedder and McDonald, 1963; Vedder, 1964; Beran, 2002). Consequently, this spectral feature is most intense in the spectra collected from the high-Al phengites, whereas it is weaker in the spectra collected from the low-Al phengites.

The two weak peaks at 12.22 and 13.40 μm mimic the peak at 10.98 μm, and their intensity decreases with a decrease in aluminum content. Unlike the peaks at 9.57 and 9.59 μm, which are caused by the presence of highly ordered Si-O bonds, these peaks are not strong, and they are not readily resolved. This suggests that the peaks at 12.22 and 13.40 μm are the result of bonds that are poorly ordered. Beran (2002) attributed similar peaks in the spectra of muscovite and paragonite to Al-O-Al vibrations occurring in tetrahedral sites. Regardless of their specific cause, both peaks are less intense in the spectra from the low-Al phengites compared to the spectra from the high-Al phengites. This is consistent with the possibility that they are related to the vibration of aluminum within the octahedral and/or tetrahedral sites.

3.5 Discussion

Phengite is the product of sericitic alteration at Olympic Dam (e.g., Roberts and Hudson, 1983), and granitic clasts and matrixes with granitic origins from the brecciated, ore-bearing zone show intense sericitization; however, rocks outside of the ore zone, in the Roxby Downs Granite, show evidence of only weak sericitization (Figure 3-4) (e.g., Hemley, 1959; Hemley and Jones, 1964; Meunier and Velde, 1982; Bishop and Bird, 1987; Eberl et al., 1987; Reeve et al., 1990 Hitzman et al., 1992; Johnson and McCulloch, 1995). The phengites from these two locations have distinct compositions—the phengites from the ore zone have a higher aluminum content than the those from the barren zones—and this compositional difference can be observed using microprobe data (Figure 3-5, Tables 3-2, 3-3) and reflectance spectroscopy (Figure 3-6, 3-7).

This difference in aluminum content is due to differences in the acidity of the fluids that sericitized the rocks in the ore-bearing and barren zone. In the ore-bearing zone, the flow of highly acidic fluids (< 4.5 pH) resulted in the complete conversion of K-feldspar to phengite, quartz, and potassium ions; in the Roxby Downs Granite, only a partial conversion of K-feldspar occurred because the fluids were less acidic (e.g., Hemley and Jones, 1964).

$$3KAlSi_3O_8 + 2H^+ (aq.) \rightarrow KAl_3Si_3O_{10}(OH)_2 + 2K^+ (aq.) + 6\ SiO_2$$

K-Feldspar — Potassic Dioctahedral Mica (Phengite) — Silica (Quartz)

As a rule, potassic dioctahedral micas that form in the hottest parts of the deposit—where hydrothermal fluids can be the most acidic—have higher

aluminum contents, whereas micas that form in cooler, distal regions contain less aluminum (Bishop and Bird, 1987; Evens, 1993; Yang et al., 2001).

Although this research is focused on the micas contained within the sericitic alteration zones associated with IOCG deposits, sericitic alteration has also been observed around other types of hydrothermal ore deposits, such as gold deposits (e.g. Callaghan, 2001). It has also been identified at porphyry copper systems—where it acts to separate the potassic core of the deposit from the surrounding zones of prophylitic alteration (Rose, 1970; Dilles and Einaudi, 1992; Silltoe, 2010), and nearly all volcanogenic massive sulfide (VMS) ore deposits have zones of sericitic alteration around the main ore-bearing regions of the deposit (Brauhart et al., 1998; Large et al., 2001). In general, many hydrothermal ore deposits show evidence of sericitic alteration, and although the research presented here focuses on the phengites from IOCG deposits, the results should be transferable to phengites contained within hydrothermal gold, porphyry copper, and VMS deposits.

The Fe-rich oxidized fluids that hematitically altered the deposit (e.g., Oreskes and Einaudi, 1992; Haynes et al., 1995) also influenced the composition of the potassic dioctahedral micas produced by sericitic alteration: it resulted in the formation of phengites with high iron contents, particularly in the ore-bearing zone. The phengites from the Roxby Downs Granite, however, contain less iron because hematitic alteration was much less in these rocks. As a result, the phengites from the barren country rocks around Olympic Dam have higher Mg-numbers than the phengites from the ore-bearing zone.

It is important to note that while most of the important changes in mineral presence and abundance can be determined using traditional analytical techniques (i.e., EPMA), they can also be determined using reflectance spectroscopy. For example, changes in the aluminum content of phengite will shift the position of the Al-OH trough between 2.195 and 2.225 μm, with higher aluminum contents producing shorter wavelength troughs. Reflectance spectroscopy requires very little sample preparation and data can be collected quickly and continuously along a drill core in a straightforward manner. As a result, potassic dioctahedral micas like phengite can be identified in a drill core, their compositions can be inferred, and changes in their mineral chemistry along the drill core can be recognized.

At Olympic Dam, the Al-OH troughs are found at shorter wavelengths in the ore-bearing zones, and the trough position—and presumably the aluminum content of phengite—is highly variable. This can be explained by the heterogeneous nature of this deposit, where multiple episodes of brecciation have produced a complex arrangement of mineral assemblages. In the barren zone, the Al-OH troughs are found at longer wavelengths, and there is less variation in their position. The mineral chemistry of the phengites in the barren zone were examined over a ~100 m distance from the ore-bearing zone, and no change in their composition with respect to their distance to the ore body was observed.

In all likelihood, a distance of 100 m is not large enough to observe a systematic change in the mineral chemistry of phengites in the Roxby Downs Granite as a function of distance to the ore body. It is anticipated, however, that on a larger scale (e.g., ~1 km), there will be changes in the mineral chemistry of

phengite (e.g., Hitzman et al., 1993; Sillitoe, 2010). In particular, we expect the more distal phengites to have a lower aluminum content and a higher Mg-number.

3.6 Conclusions

A mineralogical and spectroscopic analysis of the potassic dioctahedral micas from the Olympic Dam iron oxide-copper-gold (IOCG) deposit has revealed that two chemically distinct phengite populations are present. The mineral chemistries of the two populations of phengites plot into two fields on a ternary diagram that we devised, which compares the number of silicon cations to the relative abundance of magnesium and iron (Figure 3-5).

Until now, very little has been published regarding the near- and mid-infrared reflectance spectroscopy of phengite although it can provide valuable information about phengite abundance and phengite mineral chemistry. For example, we show how the near-infrared spectrum of phengite between 2.190 and 2.230 μm can be used to identify phengite and analyze its aluminum content. The intensity of this spectral feature was plotted and used as a proxy to infer phengite abundance along the drill core. The position of the Al-OH spectral features was then used to infer the aluminum concentration of phengite.

Although the near-infrared reflectance spectra are typically used to identify and analyze potassic dioctahedral micas like phengite, we show that important information can also be obtained by examining the mid-infrared reflectance spectra between 6 and 14 μm. For the first time, we present the mid-infrared reflectance spectrum of phengite (Figure 3-3 and 3-11), and show how three mid-infrared spectral features can be used to analyze the aluminum content

of phengite and its placement within the mineral. First, the Christiansen Feature, shifts to longer wavelengths with an increase in total aluminum concentrations; second, the peak at 9.6 μm shifts to longer wavelengths with a higher degree of Al^{3+} substitution in tetrahedral sites; and third, the peaks at 10.98, 12.22, and 13.40 μm increase in their intensity as the amount of aluminum contained within tetrahedral and/or octahedral sites increases.

Determining the aluminum content of potassic dioctahedral micas such as phengite is extremely important when examining hydrothermal ore deposits such as Olympic Dam because it provides valuable information about the extent of sericitic alteration that has taken place. Sericitic alteration is more intense near the ore-bearing zones, and it decreases as the distance to the ore zone increases. Using reflectance spectroscopy, this information about the degree of sericitization can be obtained rapidly and with very little sample preparation.

3.7 Acknowledgements

The authors would like to thank Kathy Ehrig at BHP Billiton (Australia); Georgina Gordon and John Keeling at PIRSA (Australia); Sasha Pontual at AusSpec (Australia); Jon Huntington at CSIRO (Australia); and Sergei Matveev, Karlis Muehlenbachs, and Thomas Stachel (De Beers Diamond Research Lab) at the University of Alberta (Canada). This project was sponsored financially between October 2007 and December 2008 by the Department of Primary Industry and Resources SA through AusScope/NCRIS. This research was also supported by a Discovery grant to Benoit Rivard from the National Science and Engineering Research Council of Canada.

3.8 Tables

Table 3-1. Selected characteristics for the near-infrared and mid-infrared reflectance spectrometers used to collect spectra from Olympic Dam drill core RU39-5371.

Instrument Name	Description	Spectral Range	Footprint	Band Width
HyLogger 2	Automated Drill Core Logger	0.4-2.5µm	8 x 8 mm	4 nm
Bomem MB100 FTIR	Laboratory Instrument	2.5-22 µm	8 x 8 mm	2-16 cm^{-1}
Thermo Nicolet Nexus 470 FTIR and Nicolet Continuum Infrared microscope	Automated Scanning Spectrometer	6-15 µm	100 x 100 µm	2-16 cm^{-1}

Table 3-2. Summary of phengite mineral chemistry from brecciated rocks from the ore-bearing zone at Olympic Dam, South Australia, based on EMPA results (values given in wt%). Data are sorted based on high, low, and average silicon cation content for each sample calculated using 11 oxygens.

	OD5 (n = 106)				OD12 (n = 148)			
	Low	High	Avg	*Std*	Low	High	Avg	Std
SiO_2	46.3	51.3	48.6	*1.23*	46.2	51.7	48.9	*1.19*
TiO_2	0.22	0.05	0.04	*0.04*	0.15	0.00	0.05	*0.08*
Al_2O_3	31.1	26.8	31.4	*1.57*	32.9	27.2	31.5	*1.47*
FeO	3.84	3.15	3.28	*0.70*	4.05	5.97	3.84	*0.78*
MgO	2.02	2.11	0.70	*0.37*	0.52	0.54	0.71	*0.59*
MnO	0.00	0.00	0.02	*0.01*	0.02	0.00	0.00	*0.01*
CaO	0.00	0.02	0.64	*0.38*	0.05	0.00	0.03	*0.03*
Na_2O	0.31	0.20	0.14	*0.08*	0.04	0.01	0.06	*0.03*
K_2O	10.8	9.52	9.24	*0.46*	11.0	9.47	10.07	*0.38*
Total	94.7	93.2	94.2	*1.50*	94.9	95.0	95.1	*1.33*
Si	3.15	3.48	3.27	*0.06*	3.13	3.48	3.27	*0.05*
Ti	0.01	0.00	0.00	*0.00*	0.01	0.00	0.00	*0.00*
Al	2.50	2.14	2.49	*0.11*	2.63	2.16	2.49	*0.11*
Fe	0.22	0.18	0.18	*0.04*	0.23	0.34	0.22	*0.04*
Mg	0.21	0.21	0.07	*0.04*	0.05	0.05	0.07	*0.06*
Mn	0.00	0.00	0.00	*0.00*	0.00	0.00	0.00	*0.00*
Ca	0.00	0.00	0.05	*0.03*	0.00	0.00	0.00	*0.00*
Na	0.04	0.03	0.02	*0.01*	0.01	0.00	0.01	*0.00*
K	0.94	0.82	0.79	*0.04*	0.95	0.81	0.86	*0.04*
Si+Mg+Fe	3.58	3.87	3.53	*0.11*	3.42	3.87	3.56	*0.11*
(Si+Mg+Fe) /Al	1.43	1.80	1.42	*0.11*	1.30	1.79	1.43	*0.11*
Al-IV	0.85	0.52	0.73	*0.06*	0.87	0.52	0.73	*0.05*
Al-VI	1.65	1.62	1.77	*0.06*	1.77	1.64	1.76	*0.07*
VI	2.09	2.02	2.02	*0.01*	2.06	2.03	2.05	*0.02*
VIII	0.98	0.85	0.86	*0.03*	0.96	0.82	0.87	*0.04*
V	0.94	0.82	0.79	*0.04*	0.95	0.81	0.86	*0.04*

Al-IV: tetrahedrally bound aluminum; Al-VI: octahedrally bound aluminum; VI: total octahedrally bound cations; VIII: total dodecahedrally bound cations

Table 3-3. Summary of phengite mineral chemistry from unbrecciated rocks from the barren Roxby Downs Granite at Olympic Dam, South Australia, based on EMPA results (values given in wt%). Data are sorted based on high, low, and average silicon cation content for each sample calculated using 11 oxygens.

	OD13 (n = 129)				**OD14** (n = 62)				**OD15** (n = 130)			
	Low	**High**	**Avg**	**Std**	**Low**	**High**	**Avg**	**Std**	**Low**	**High**	**Avg**	**Std**
SiO_2	46.2	53.7	50.6	*1.45*	47.6	53.0	50.6	*1.17*	46.7	52.0	50.4	*1.53*
TiO_2	0.04	0.04	0.03	*0.02*	0.07	0.06	0.04	*0.02*	0.50	0.05	0.05	*0.07*
Al_2O_3	31.1	28.0	29.2	*0.91*	32.7	26.2	28.8	*1.21*	28.6	26.8	28.9	*1.01*
FeO	5.97	3.53	4.15	*0.86*	2.73	4.31	3.90	*0.70*	4.94	4.49	3.74	*0.66*
MgO	0.09	1.85	1.34	*0.31*	1.09	2.35	1.39	*0.32*	2.33	2.22	1.57	*0.31*
MnO	0.03	0.00	0.01	*0.01*	0.00	0.00	0.01	*0.01*	0.02	0.00	0.01	*0.01*
CaO	0.07	0.01	0.04	*0.09*	0.00	0.03	0.03	*0.02*	0.02	0.01	0.05	*0.08*
Na_2O	0.10	0.06	0.08	*0.03*	0.13	0.19	0.14	*0.04*	0.15	0.04	0.08	*0.02*
K_2O	9.99	9.47	9.62	*0.30*	10.7	9.74	9.91	*0.30*	10.76	9.61	9.58	*0.36*
Total	94.0	96.6	95.1	*1.55*	95.5	97.4	95.6	*0.95*	94.0	95.2	94.4	*1.75*
Si	3.19	3.50	3.38	*0.05*	3.19	3.51	3.39	*0.06*	3.22	3.47	3.39	*0.05*
Ti	0.00	0.00	0.00	*0.00*	0.00	0.00	0.00	*0.00*	0.03	0.00	0.00	*0.00*
Al	2.53	2.15	2.30	*0.06*	2.58	2.04	2.28	*0.09*	2.33	2.11	2.29	*0.06*
Fe	0.35	0.19	0.23	*0.05*	0.15	0.24	0.22	*0.04*	0.29	0.25	0.21	*0.04*
Mg	0.01	0.18	0.13	*0.03*	0.11	0.23	0.14	*0.03*	0.24	0.22	0.16	*0.03*
Mn	0.00	0.00	0.00	*0.00*	0.00	0.00	0.00	*0.00*	0.00	0.00	0.00	*0.00*
Ca	0.01	0.00	0.00	*0.01*	0.00	0.00	0.00	*0.00*	0.00	0.00	0.00	*0.01*
Na	0.01	0.01	0.01	*0.00*	0.02	0.02	0.02	*0.00*	0.02	0.00	0.01	*0.00*
K	0.88	0.79	0.82	*0.03*	0.91	0.82	0.85	*0.03*	0.95	0.82	0.82	*0.04*
Si+Mg+ Fe	3.55	3.87	3.75	*0.06*	3.46	3.98	3.75	*0.09*	3.75	3.95	3.75	*0.06*
(Si+Mg +Fe) /Al	1.40	1.80	1.63	*0.07*	1.34	1.95	1.65	*0.10*	1.61	1.87	1.64	*0.07*
Al-IV	0.81	0.50	0.62	*0.05*	0.81	0.49	0.61	*0.06*	0.78	0.53	0.61	*0.05*
Al-VI	1.73	1.65	1.68	*0.03*	1.78	1.56	1.67	*0.04*	1.55	1.58	1.68	*0.04*
VI	2.08	2.03	2.05	*0.02*	2.04	2.03	2.03	*0.01*	2.10	2.06	2.05	*0.02*
VIII	0.90	0.79	0.83	*0.03*	0.93	0.85	0.87	*0.03*	0.97	0.82	0.83	*0.04*
V	0.88	0.79	0.82	*0.03*	0.91	0.82	0.85	*0.03*	0.95	0.82	0.82	*0.04*

Al-IV: tetrahedrally bound aluminum; Al-VI: octahedrally bound aluminum; VI: total octahedrally bound cations; VIII: total dodecahedrally bound cations

3.9 Figures

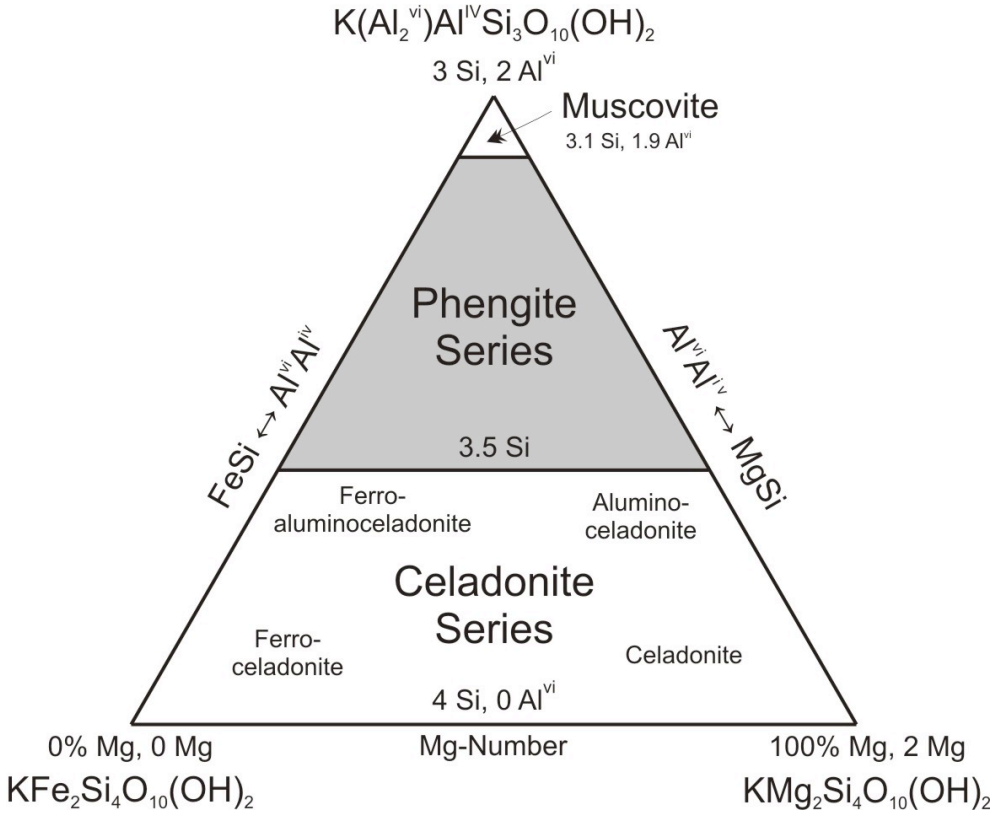

Figure 3-1. Ternary diagram showing the three endmembers used to classify phengite: muscovite $K(Al_2)AlSi_3O_{10}(OH)_2$, $KFe_2Si_4O_{10}(OH)_2$, and $KMg_2Si_4O_{10}(OH)_2$. The phengite series occupies the space between muscovite and the celadonite series. Potassic dioctahedral micas having 3.1 to 3.5 Si cations p.f.u. (11 oxygens) belong to the phengite series.

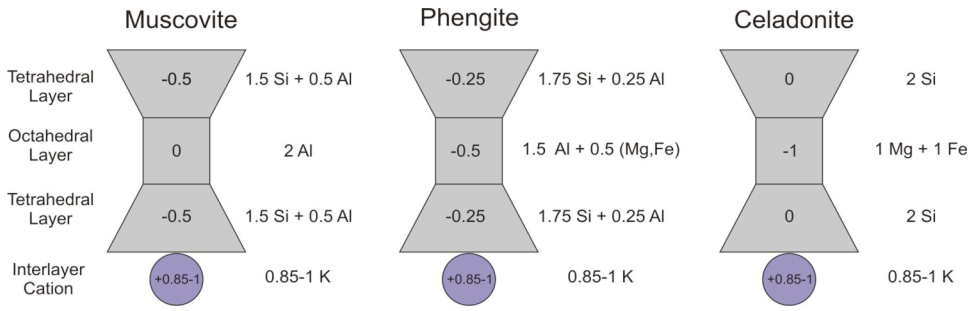

Figure 3-2. The composition, charges, and arrangement of the tetrahedral layer, octahedral layer, and dodecahedral interlayer for muscovite, phengite, and celadonite. In these idealized diagrams, it is assumed that iron (Fe^{2+}) is only present in the octahedral layers. In reality, iron (Fe^{3+}) can also be present in the tetrahedral layers.

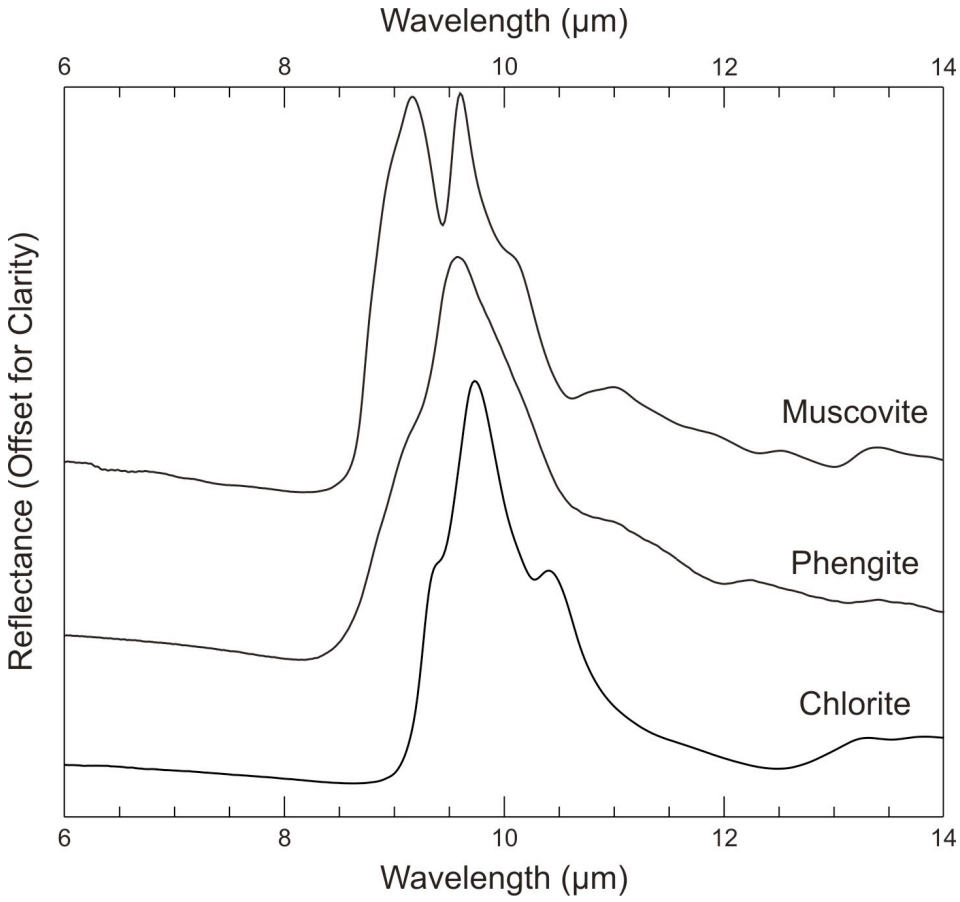

Figure 3-3. Reflectance spectra (6-14 μm) of muscovite, phengite, and chlorite collected at an aperture size of 100 x 100 μm. The spectra of muscovite and chlorite were obtained from the cleavage planes of pure hand samples (2 x 2 x 1 cm). The spectrum of phengite was taken from this study.

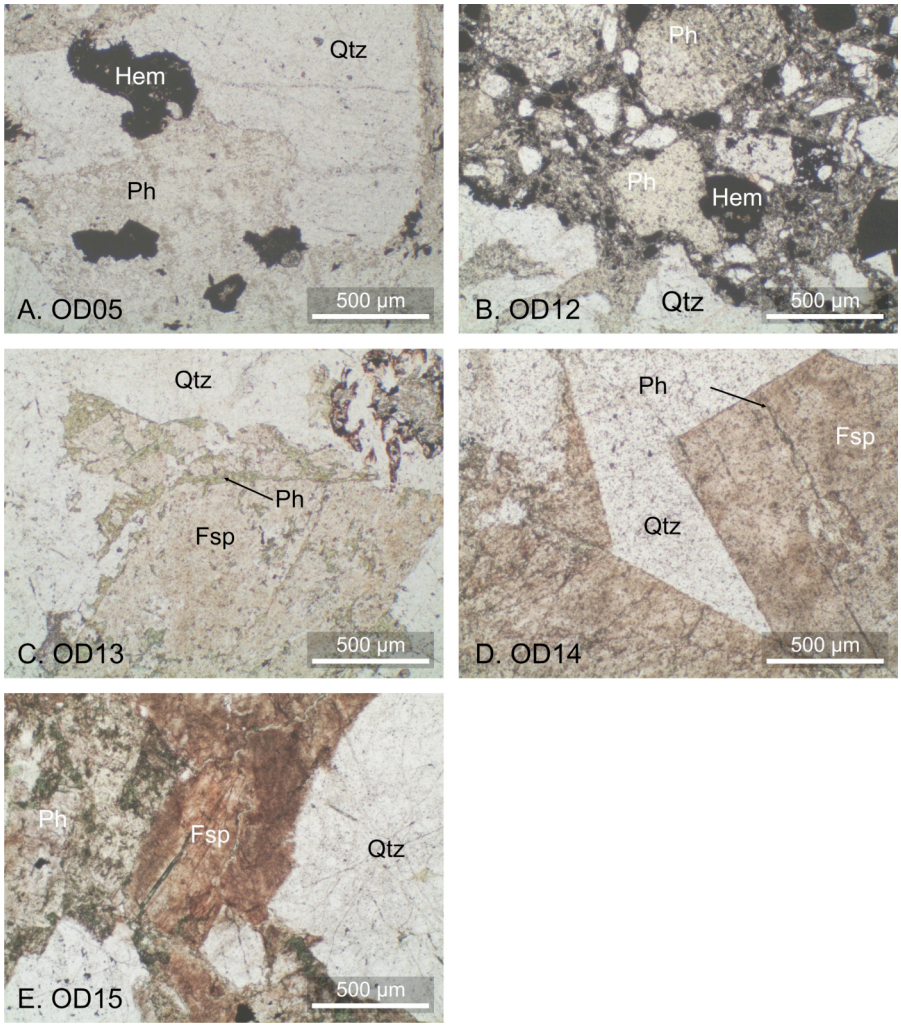

Figure 3-4. Photomicrographs of thin sections of phengite-bearing rocks from Olympic Dam drill core RU39-5371: (A) OD05 (38.8 m), (B) OD12 (183.8 m), (C) OD13 (206.5 m), (D) OD14 (245.3 m), and (E) OD15 (293.4 m). Samples OD05 and OD12 are from intensely altered, ore-bearing rocks; they contain mainly quartz and phengite. Samples OD13, OD14, and OD15 are from weakly-altered, barren rocks; they contain mainly quartz, feldspar, and phengite. The ore-bearing rocks are heavily brecciated, whereas the barren rocks are unbrecciated or only slightly brecciated. Hem = Hematite, Ph = phengite, Fsp = feldspar, Qtz = quartz.

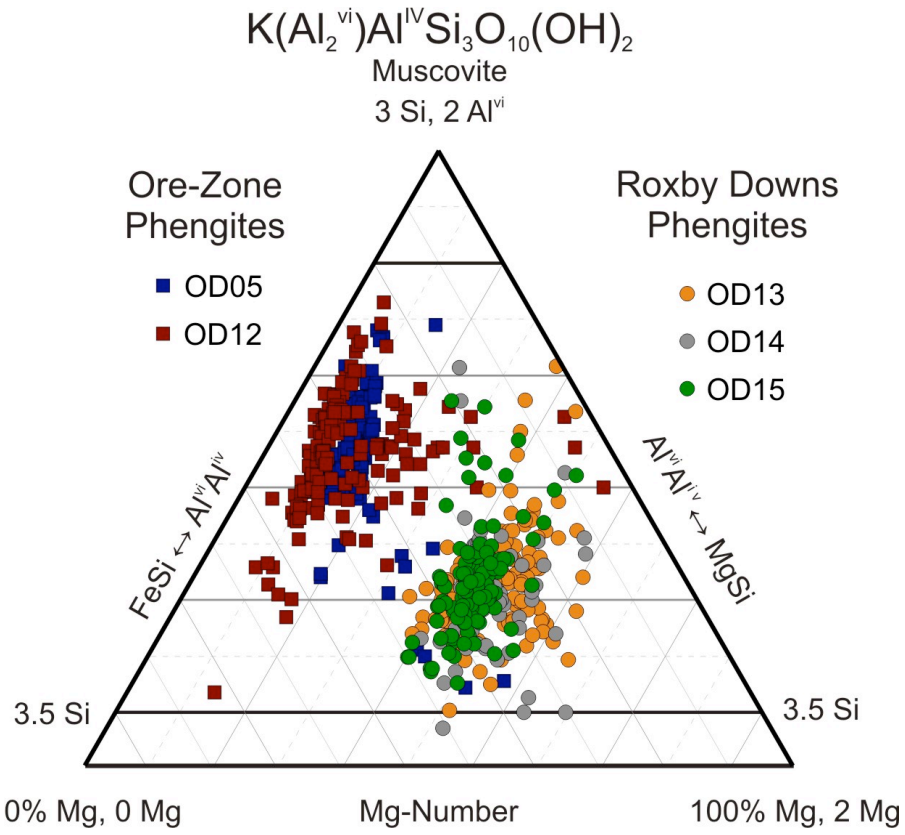

Figure 3-5. The phengite series: ternary diagram representing the potassic dioctahedral micas from Olympic Dam. The number of silicon cations is plotted against the relative proportion of iron cations to magnesium cations, calculated using 11 oxygens. The micas from Olympic Dam plot into two groups within the phengites series.

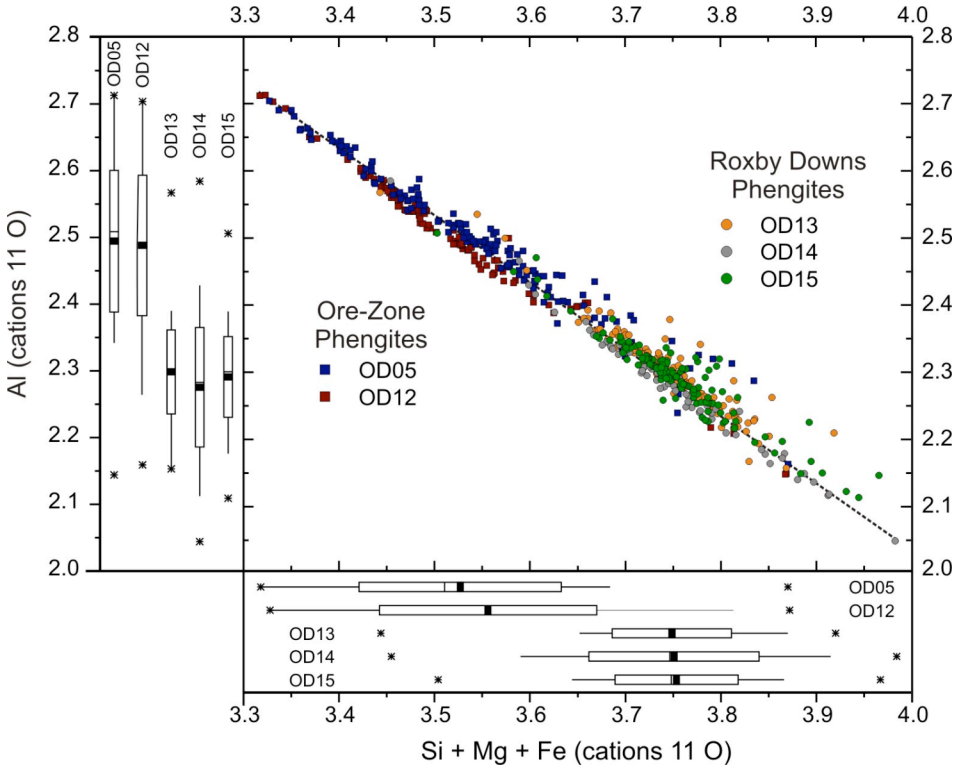

Figure 3-6. The cation results of 597 potassic dioctahedral micas analyzed from fives samples from the Olympic Dam deposit. Cations were calculated using 11 oxygens. Samples OD05 and OD12 are from the brecciated, ore-bearing zone, whereas samples OD13, OD14, and OD15 are from the unbrecciated, barren Roxby Downs Granite. The box diagrams along each axis show the mean value for each sample (filled squares), the minimum and maximum values (stars), and one standard deviation (unfilled boxes).

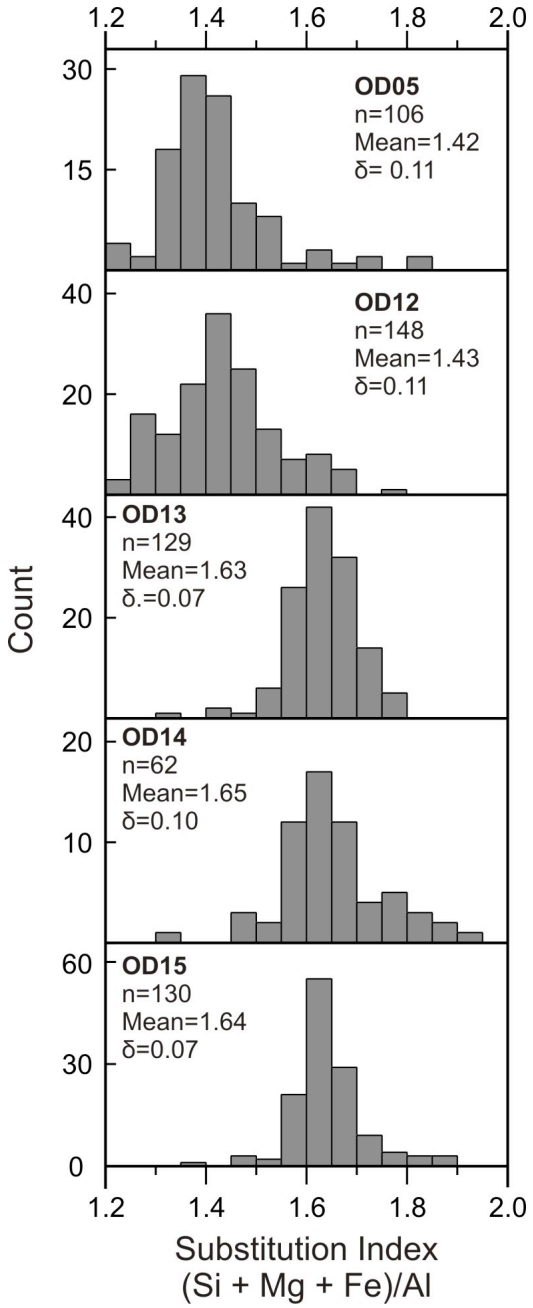

Figure 3-7. Histograms showing the substitution index ((Si + Mg + Fe)/Al) of 597 phengites from Olympic Dam. Samples OD05 and OD12 are from ore-bearing rocks, whereas samples OD13, OD14, and OD15 are from barren rocks. The value for endmember muscovite should be ~1.

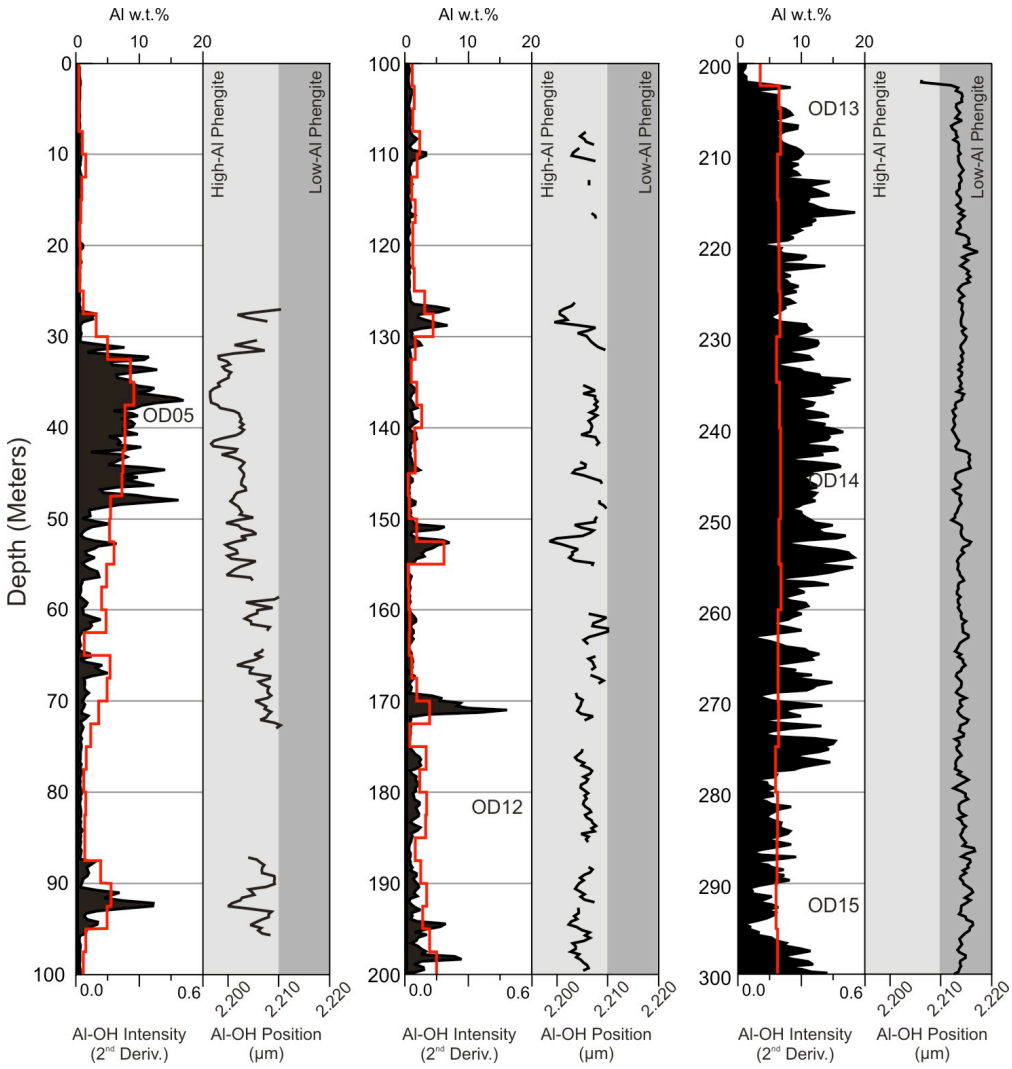

Figure 3-8. Depth profile of drill core RU39-5371. Intensity of the Al-OH spectral feature is shown using black fill (only spectra with troughs >0.03 intensity are included), the position of the Al-OH spectral feature is shown using black lines, and the abundance of Al wt% determined by whole rock geochemistry is shown using red lines. The high-Al and low-Al phengite fields are indicated in grey. Spectral data were smoothed using a moving average encompassing 50 spectra.

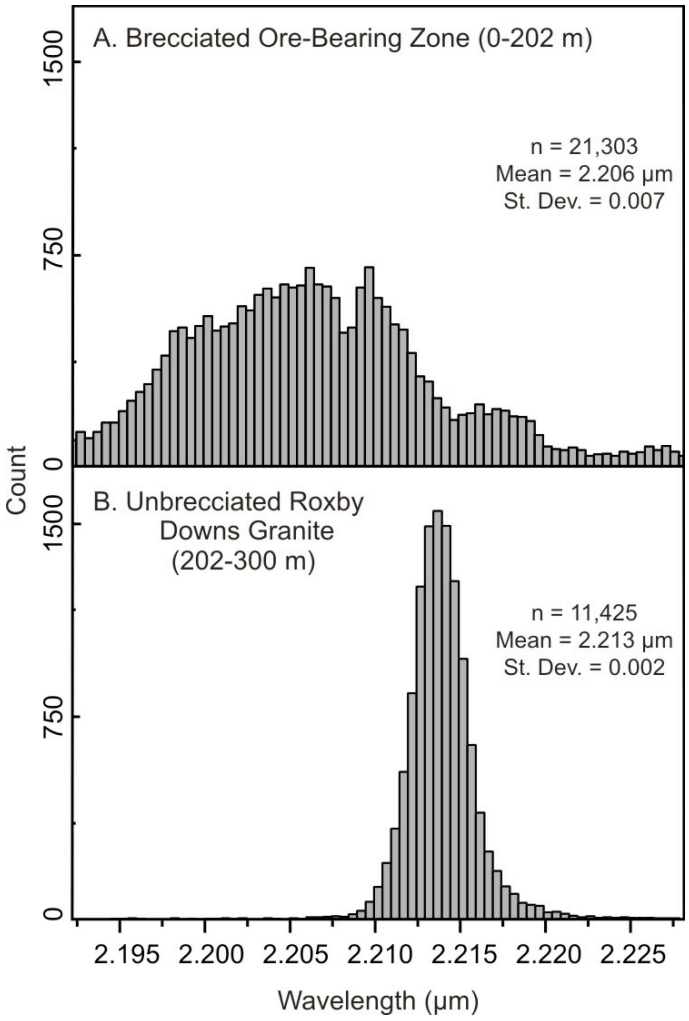

Figure 3-9. Histogram showing the frequency distribution of trough position obtained from the reflectance spectrum with the continuum removed. The data have been subdivided into two groups: phengites from the brecciated, ore-bearing rocks (0-202 m), and phengites from the unbrecciated Roxby Downs Granite (202-300 m).

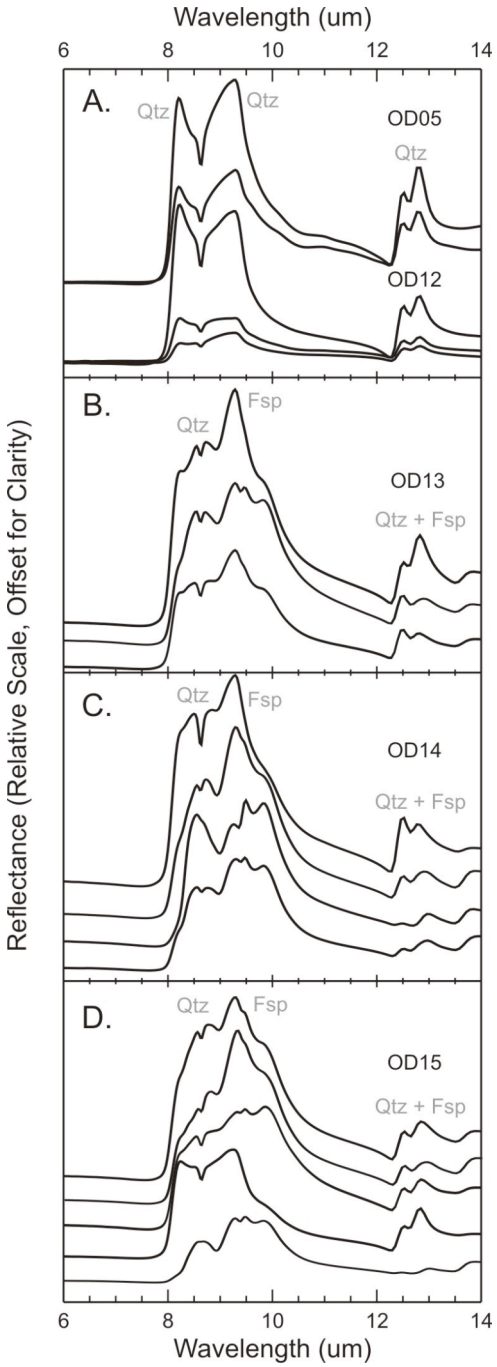

Figure 3-10. Mid-infrared reflectance spectra (6-14 μm) measured from 5 phengite-bearing samples from Olympic Dam: (A) OD05 and OD12, (B) OD13, (C) OD14, and (D) OD15. These spectra were collected using a Bomem FTIR, which collects spectra with a field of view of 8 x 8 mm. Broad spectral features relating to the presence of major mineral phases have been labeled (Qtz = quartz, Fsp = feldspar).

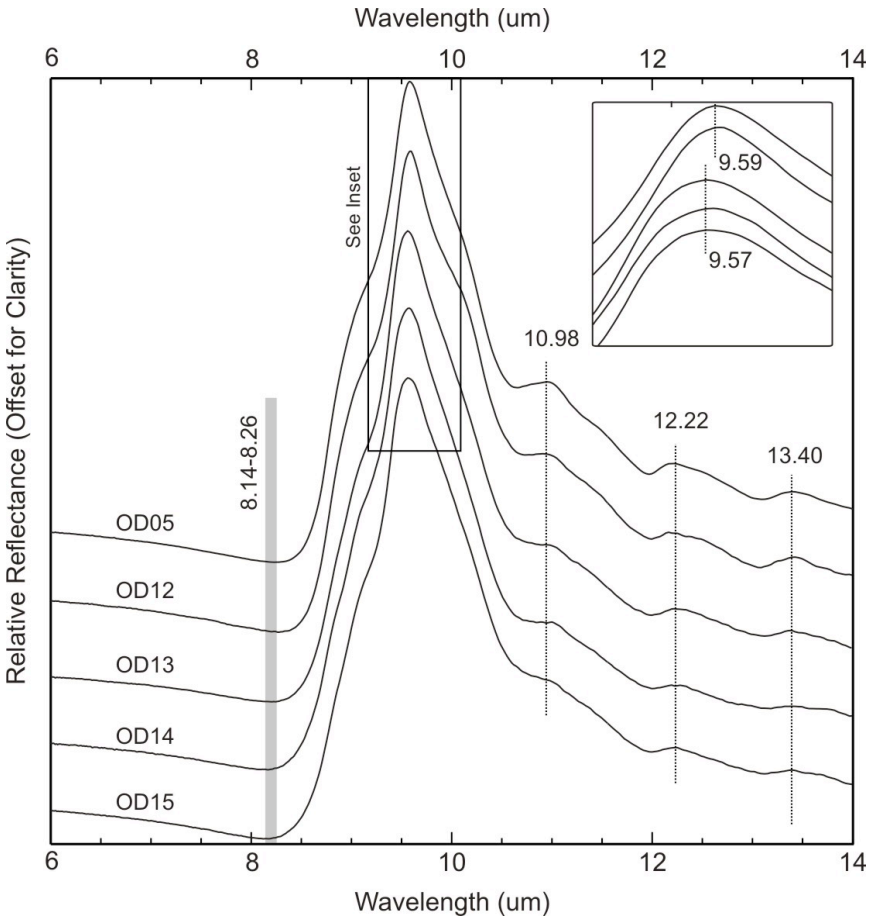

Figure 3-11. Mid-infrared reflectance spectra (6-14 μ) of phengite from the Olympic Dam IOCG deposit. These spectra were collected using the Micro-FTIR spectrometer, which operates with a field of view of 100 x 100 μm. These spectra were produced by averaging all of the pure mineral spectra identified for each sample. (OD05, n = 97; OD12, n = 15; OD13, n = 23; OD14, n = 11; and OD15, n = 9).

3.10 References

Belperio, A., Flint, R., and Freeman, H. (2007) Prominent Hill: a hematite-dominated, iron oxide copper-gold system. Economic Geology, 102(8), 1,499-1,510.

Ben-Dor, E., Inbar, Y., and Chen, Y. (1997) The reflectance spectra of organic matter in the visible near-infrared and short wave infrared region (400-2500 nm) during a controlled decomposition process. Remote Sensing of Environment, 61(1), 1-15.

Beran, A. (2002) Infrared spectroscopy of micas. Reviews in Mineralogy and Geochemistry, 46(1), 351-369.

Berman, M. (2006) Some unmixing problems and algorithms in spectroscopy and hyperspectral imaging. 35th Applied Imagery and Pattern Recognition Workshop (AIPR'06), p. 15.

Besson, G., and Drits, V.A. (1997) Refined relationships between chemical composition of dioctahedral fine-grained micaceous minerals and their infrared spectra within the OH stretching region. Part II: the main factors affecting OH vibrations and quantitative analysis. Clays and Clay Minerals, 45(2), 170-183.

Bishop, B.P., and Bird, D.K. (1987) Variation in sericite compositions from fracture zones within the Coso Hot Springs geothermal system. Geochimica et Cosmochimica Acta, 51, 1,245-1,256.

Bastrakov, E.N., Skirrow, R.G., and Davidson, G. (2007) Fluid evolution and origins of iron oxide Cu-Au prospects in the Olympic Dam district, Gawler Craton, South Australia: Economic Geology, 102, p. 1,415-1,440.

Brauhart, C.W., Groves, D.I., and Morant, P. (1998) Regional alteration systems associated with volcanogenic massive sulfide mineralization at Panorama, Pilbara, Western Australia. Economic Geology, 93, p. 292-302.

Brigatti, M.F., Frigieri, P., and Poppi, L. (1998) Crystal chemistry of Mg-, Fe-bearing muscovites-2M1. American Mineralogist, 83, 775-785.

Budd, A., and Skirrow, R.G. (2007) The nature and origin of gold deposits of the Tarcoola Goldfield and implications for the central Gawler gold province, South Australia: Economic Geology, 102, p. 1,541-1,563.

Callaghan, T., (2001) Geology and host-rock alteration of the Henty and Mount Julia gold deposits, western Tasmania. Economic Geology, 96, p. 1,073-1,088.

Cardile, C.M. (1989) Tetrahedral iron in smectite: a critical comment. Clays and Clay Minerals, 37(2), 185-188.

Christensen, P.R., Bandfield, J.L., Hamilton, V.E., Howard, D.A., Lane, M.D., Piatak, J.L., Ruff, S.W., and Stefanov, W.L. (2000) A thermal emission spectral library of rock-forming minerals. Journal of Geophysical Research, 105(E4), 9735-9739.

Cibin, G., Cinque, G., Marcelli, A., Mottana, A., and Sassi, R. (2008) The octahedral sheet of metamorphic 2M1-phengites: a combined EMPA and

AXANES study. American Mineralogist, 93, 414-425.

Clark, R.N. (1999) Spectroscopy of rocks and minerals, and principles of spectroscopy. In A.N. Rencz, Ed. Manual of Remote Sensing, Volume 3, Remote Sensing for the Earth Sciences, p. 3-58. John Wiley and Sons, New York.

Clark, R.N., King, T.V.V., Klejwa, M., and Swayze, G.A. (1990) High spectral resolution reflectance spectroscopy of minerals. Journal of Geophysical Research, 95(B8), 12,653-12,680.

Creaser, R.A., and Cooper, J.A. (1993) U-Pb geochronology of middle Proterozoic felsic magmatism surrounding the Olympic Dam Cu-U-Au-Ag and Moonta Cu-Au-Ag deposits, South Australia: Economic Geology, 88, p. 187-197.

Cross, K.C., Daly, S.J., and Flint, R.B. (1993) Mineralisation associated with the GRV and the Hiltaba suite granitoids. In J.F. Drexel, W.V. Preiss, and A.J. Parker, Eds. The geology of South Australia, 1: The Precambrian, p. 132-137.

Crowley, M.S., and Roy, R. (1964) Crystalline solubility in the muscovite and phlogopite groups. American Mineralogist, 49, 348-362.

Davidson, G.J., and Large, R.R. (1998) Proterozoic copper-gold deposits. Journal of Australian Geology and Geophysics, 17(4), 105-113.

Davidson, G.J., Paterson, H., Meffre, S., and Berry, R.F. (2007) Characteristics and origin of the Oak Dam east breccia-hosted, iron oxide Cu-U-(Au)

deposit: Olympic Dam region, Gawler Craton, South Australia: Economic Geology, 102, p. 1,471-1,498.

Dilles, J.H., and Einaudi, M.T. (1992) Wall-rock alteration and hydrothermal flow paths about the Ann-Mason porphyry copper deposit, Nevada—a 6 km vertical reconstruction: Economic Geology, 87, p. 1,963−2,001.

Direen, N.G., and Lyons, P., (2007) Regional crustal setting of iron oxide Cu-Au mineral systems of the Olympic Dam region, South Australia: Insights from potential-field modeling: Economic Geology, 102, p. 1,397-1,414.

Duke, E.F. (1994) Near infrared spectra of muscovite, Tschermak substitution, and metamorphic reaction progress: implications for remote sensing. Geology, 22, 621-624.

Duke, E.F., and Lewis, R.S. (2010) Near infrared spectra of white mica in the Belt Supergroup and implications for metamorphism. American Mineralogist, 95, 908-920.

Eberl, D.D., Srodon, J., Lee, M., Nadeau, P.H., and Northrop, H.R. (1987) Sericite from the Silverton caldera, Colorado: correlation among structure, composition, origin, and particle thickness. American Mineralogist, 72, 914-934.

Ernst, W.G. (1963) Significance of phengitic micas from low-grade schists. American Mineralogist, 48, 1,357-1,373.

Evens, A. M. (1993), Ore geology and industrial minerals: an introduction. Blackwell Science, 390 p.

Farmer, V.C. (1974) The layer silicates. In V.C. Farmer, Ed. The infrared spectra of minerals, p. 331-363. Mineral Society of London, London.

Farmer, V.C., and Lazarev, A.N. (1974) Symmetry and crystal vibrations. In V.C. Farmer, Ed. The infrared spectra of minerals, p. 51-68. Mineralogical Society, London.

Farmer, V.C., and Russell, J.D. (1964) The infra-red spectra of layer silicates. Spectrochimica Acta, 20(7), 1,149-1,173.

Farrington, G.A., Hoogenboom, H.J., Dekker, A.G., and Malthus, T.J. (1994) Understanding spectra derivatives of water reflectance from high resolution airborne imagery. Proceedings of the 1st International Airborne Remote Sensing Conference and Exhibition, 3, p. 46-55. Ann Arbor, Environmental Research Institute of Michigan, France.

Feng, J., Rivard, B., Gallie, A., Sanchez-Azofeifa, A., and Francis, H. (2004) Rock-type identification in a simulated underground environment using second-derivative thermal infrared reflectance spectra. Geological Society of America Bulletin, 116(11/12), 1,318-1,326.

Foster, M.D. (1956) Correlation of dioctahedral potassium micas on the basis of their charge relations. Geological Survey Bulletin, 1036-D, 57-67.

Franz, G., Hinrichsen, T., and Wannemacher, E. (1977) Determination of the miscibility gap on the solid solution series paragonite-margarite by means of the infrared spectroscopy. Contributions to Mineralogy and Petrology, 59, 307-316.

Frey, M., Hunziker, J.C., Jager, E., and Stern, W.B. (1983) Regional distribution

of white K-mica polymorphs and their phengite content in the central Alps. Contributions to Mineralogy and Petrology, 83, 185-197.

Gouzu, C., Itaya, T., and Takeshita, H. (2005) Interlayer cation vacancies of phengites in calcshists from the Piemonte zone, western Alps, Italy. Journal of Mineralogical and Petrological Sciences, 100, 142-149.

Gow, P.A., Wall, V.J., Oliver, N.H.S., and Valenta, R.K. (1994) Proterozoic iron oxide (Cu-U-Au-REE) deposits: further evidence of hydrothermal origins. Geology, 22(7), 633-636.

Guidotti, C.V., Yates, M.G., Dyar, M.D., and Taylor, M.E. (1994) Petrogenetic implications of the Fe^{3+} content of muscovite in pelitic schists. American Mineralogist, 79, 793-795.

Hauck, S.A. (1990) Petrogenesis and tectonic setting of middle Proterozoic iron oxide-rich ore deposits—and ore deposit model for Olympic Dam-type mineralization 1932, U.S. Geological Survey Bulletin, p. 4-39.

Haynes, D.W., Cross, K.C., Bills, R.T., and Reed, M.H. (1995) Olympic Dam ore genesis: a fluid-mixing model. Economic Geology, 90, 281-307.

Heinrich, E.W., Levinson, A.A., Levandowski, D.W., and Hewitt, C.H. (1953) Studies in the natural history of micas, M978, p. 258. Engineering Research Institute, University of Michigan, Ann Arbor.

Hemley, J.J. (1959) Some mineralogical equilibria in the system K_2O-Al_2O_3-SiO_2-H_2O. American Journal of Science, 257, 241-270.

Hemley, J.J., and Jones, W.R. (1964) Chemical aspects of hydrothermal alteration with emphasis on hydrogen metasomatism. Economic Geology, 59(4),

538-569.

Hendricks, S.B., and Ross, C.S. (1941) Chemical composition and genesis of glauconite and celadonite. Journal of the Mineralogical Society of America, 26(12), 683-708.

Hitzman, M.W., Orekes, N., and Einaudi, M.T. (1992) Geological characteristics and tectonic settings of Proterozoic iron oxide (Cu-U-Au-REE) deposits. Precambrian Research, 58, 241-287.

Huguenin, R.L., and Jones, J.L. (1986) Intelligent information extraction from reflectance spectra: absorption band positions. Journal of Geophysical Research, 91(B9), 9,585-9,598.

Hunt, G.R. (1977) Spectral signatures of particulate materials in the visible and near infrared. Geophysics, 42(3), 501-513.

Hunt, G.R. (1979) Near-infrared (1.3-2.4 μm) spectra of alteration minerals—potential for use in remote sensing. Geophysics, 44(12), 1,979-1,986.

Hunt, G.R., and Ashley, R.P. (1979) Spectra of altered rocks in the visible and near infrared. Economic Geology, 74, 1,613-1,629.

Hunt, G.R., and Salisbury, J.W. (1970) Visible and near-infrared spectra of minerals and rocks: I Silicate minerals. Modern Geology, 1, 283-300.

Iiishi, K., Tomisaka, T., Kato, T., and Umegaki, Y. (1971) Isomorphous substitution and infrared and far infrared spectra of the feldspar group. Neues Jahrbuch fur Mineralogie Abhandlungen, 115, 98-119.

Johnson, J.P., and McCulloch, M.T. (1995) Sources of mineralising fluids for the Olympic Dam deposit (South Australia): Sm-Nd isotopic constraints.

Chemical Geology, 121(1-4), 177-199.

Large, R.R., Allen, R.L., Blake, M.D., and Herrmann, W. (2001) Hydrothermal alteration and volatile element halos for the Rosebery K lens volcanic-hosted massive sulfide deposit, western Tasmania. Economic Geology, 96, p. 1,055-1,092.

Laves, F., and Hafner, S. (1962) Infrared absorption effects, nuclear magnetic resonance and structure of feldspars. Norsk Geologisk Forening, 42: Feldspar Volume, 57-71.

Li, G., Peacor, D.R., Coombs, D.S., and Kawachi, Y. (1997) Solid solution in the celadonite family: the new minerals ferroceladonite, $K_2Fe_2^{2+}Fe_2^{3+}Si_8O_{22}(OH)_4$, and ferraluminoceladonite, $K_2Fe_2^{2+}Al_2Si_8O_{20}(OH)_4$. American Mineralogist, 82, 503-511.

Logan, L.M., Hunt, G.R., Salisbury, J.W., and Balsamo, S.R. (1973) Compositional implications of Christiansen frequency maximums for infrared remote sensing applications. Journal of Geophysical Research, 78(23), 4,983-5,003.

Longhi, I., Mazzoli, C., and Sgavetti, M. (2000) Determination of metamorphic grade in siliceous muscovite-bearing rocks in Madagascar using reflectance spectroscopy. Terra Nova, 12(1), 21-27.

Lyon, R.J.P., Tuddenham, W.M., and Thompson, C.S. (1959) Quantitative mineralogy in 30 minutes. Economic Geology, 54(6), 1,047-1,055.

Mason, P., and Huntington, J.F. (2010) HyLogger 2 components and pre-processing: an overview In T. Munson, and K. Johnston, Eds.

Technological Note 2010-001, p. 9. Northern Territory Geological Survey, Darwin.

Massonne, H.J., and Schreyer, W. (1987) Phengite geobarometry based on the limiting assemblage with K-feldspar, phlogopite, and quartz. Contributions to Mineralogy and Petrology, 96(2), 212-224.

Meunier, A., and Velde, B. (1982) Phengitization, sericitizaion and potassium-beidellite in a hydrothermal-altered granite. Clay Minerals, 17, 285-299.

Moenke, H.H.W. (1974) Chapter 16: Silica, the three dimensional silicates, borosilicates and beryllium silicates. In V.C. Farmer, Ed. The infrared spectra of minerals, No. 4, p. 365-382. Mineralogical Society (Great Britain), London.

O'Driscoll, E.S.T. (1986) Observations of the lineaments-ore relation: Philosophical Transactions of the Royal Society of London, 317, p. 195-218.

Ogorodova, L.P., Kiseleva, I.A., Mel'chakova, L.V., and Shuriga, T.N. (2006) Thermochemical study of natural phengite. Geochemistry International, 44(2), 196-198.

Oreskes, N., and Einaudi, M.T. (1990) Origin of rare element-enriched hematite breccias at the Olympic Dam Cu-U-Au Deposit, Roxby Downs, South Australia. Economic Geology, 85(1), 1-28.

Pauling, L. (1930) The structure of the micas and related minerals. Proceedings of the National Academy of Science, 16(2), 123-129.

Pollard, P. (2006) An intrusion-related origin for Cu–Au mineralization in iron

oxide-copper-gold (IOCG) provinces. Mineralium Deposita, 41(2), 179-187.

Post, J.L., and Noble, P.N. (1993) The near-infrared combination band frequencies of dioctahedral smectites, micas, and illites. Clay and Clay Minerals, 41(4), 639-644.

Reeve, J.S., Cross, K.C., Smith, R.N., and Oreskes, N. (1990) Olympic Dam copper-uranium-gold-silver deposit. In F.E. Hughes, Ed. Geology of the Mineral Deposits of Australia and Papua New Guinea, p. 1,009-1,035. The Australasian Institute of Mining and Metallurgy, Melbourne.

Rieder, M. (1998) Nomenclature of the micas. The Canadian Mineralogist, 36, 905-912.

Roberts, D.E., and Hudson, G.R.T. (1983) The Olympic Dam copper-uranium-gold deposit, Roxby Downs, South Australia. Economic Geology, 78(5), 799-822.

Rose, A.W., 1970, Zonal relations of wallrock alteration and sulfide distribution at porphyry copper deposits: Economic Geology, 65, p. 920-936.

Saksena, B. (1940) Analysis of the Raman and infra-red spectra of α-quartz. Proceedings Mathematical Sciences, 12(1), 93-139.

Salisbury, J.W., and Walter, L.S. (1989) Thermal infrared (2.5-13.5 μm) spectroscopic remote sensing of igneous rock types on particulate planetary surfaces. Journal of Geophysical Research, 94, 9,192-9,202.

Schaller, W.T. (1950) An interpretation of the composition of high-silica sericites. Mineral Magazine, 29, 406-415.

Schmidt, M.W., Dugnani, M., and Artioli, G. (2001) Synthesis and characterization of white micas in the join muscovite-aluminoceladonite. American Mineralogist, 86, 555-565.

Shau, Y.-H., Feather, M.E., Essene, E.J., and Peacor, D.R. (1991) Genesis and solvus relations of submicroscopically intergrown paragonite and phengite in a blueschist from northern California. Contributions to Mineralogy and Petrology, 106, 367-378.

Sillitoe, R.H. (2010) Porphyry copper systems. Economic Geology, 105, 3-41.

Simon, I., and McMahon, H.O. (1953) Study of the structure of quartz, cristobalite, and vitreous silica by reflection in infrared. The Journal of Chemical Physics, 21(1), 23-30.

Skirrow, R.G., Bastrakov, E.N., Barovich, K., Fraser, G.L., Creaser, R.A., Fanning, C.M., Raymond, O.L., and Davidson, G.J. (2007) Timing of iron oxide Cu-Au-(U) hydrothermal activity and Nd isotope constraints on metal sources in the Gawler Craton, South Australia: Economic Geology, 102, p. 1,441-1,470.

Stubican, V., and Roy, R. (1961) Infrared spectra of layer-structure silicates. Journal of the American Ceramic Society, 44(12), 625-627.

Swayze, G.A., Clark, R.N., Kruse, F., Sutley, S., and Gallagher, A. (1992) Ground-truthing AVIRIS mineral mapping at Cuprite, Nevada. Summaries of the Third Annual JPL Airborne Geoscience Workshop, Volume 1: AVIRIS Workshop, p. 47-49. JPL Publications.

Tappert, M., Rivard, B., Giles, D., Tappert, R., and Mauger, A. (2011) Automated

drill core logging using visible and near-infrared reflectance spectroscopy: a case study from the Olympic Dam IOCG deposit, South Australia. Economic Geology, 106, 289-296.

van Ruitenbeek, F.J.A., Debba, P., van der Meer, F.D., Cudahy, T., van der Meijde, M., and Hale, M. (2006) Mapping white micas and their absorption wavelengths using hyperspectral band ratios. Remote Sensing of Environment, 102(3-4), 211-222.

Vedder, W. (1964) Correlations between infrared spectrum and chemical composition of mica. The American Mineralogist, 49, 736-768.

Vedder, W., and McDonald, R.S. (1963) Vibrations of the OH ions in muscovite. Journal of Chemical Physics, 38, 1,583-1,590.

Velde, B. (1965) Phengite micas: synthesis, stability, and natural occurrence. American Journal of Science, 263, 886-913.

Velde, B. (1967) Si^{+4} Content of natural phengites. Contributions to Mineralogy and Petrology, 14(3), 250-258.

Williams, P.J., Barton, M.D., Johnson, C., Fontbote, L., and de Haller, A. (2005) Iron oxide copper-gold deposits: geology, space-time distribution, and possible modes of origin. Economic Geology, 100th Anniversary Volume, 371-405.

Winchell, A.N. (1927) Further studies in the mica group. American Mineralogist, 12(7), 267-279.

Chapter 4: Natural variability in the mid-infrared reflectance spectra of quartz caused by crystal orientation

4.1 Introduction

Quartz is one of the most thoroughly studied minerals on Earth, and early investigations into its behavior in the mid-infrared were conducted on single crystals. These investigations revealed that quartz produces two distinct reflectance spectra in the mid-infrared (6-15 μm): one collected parallel to the optic axis (i.e., the c-axis), and another collected perpendicular to the optic axis (i.e., the a-axis) (Figure 4-1) (Coblentz, 1906; Reinkober, 1911; Plyler, 1929; Saksena, 1940; Simon and McMahon, 1953; Sptitzer and Kleinman, 1961; Lyon and Burns, 1963; Wald and Salisbury, 1995). This effect was well documented in these earlier studies, but it was often viewed as a nuisance because these variations added an undesirable level of complexity and did not provide additional compositional information. After this realization, most reflectance spectra were collected from powdered materials—which produced an 'average' spectrum that contained no orientation information—and this simplified the analysis procedure greatly (e.g., Conel 1969; Salisbury et al., 1991; Wald and Salisbury, 1995; Wenrich and Christensen, 1996). As a result, the majority of spectra in publicly available mineral spectral libraries are from powdered rocks and minerals, and the spectra were measured at the centimeter scale.

The recent development of high spatial resolution reflectance spectrometers (e.g., instruments that operate with a 3 x 3 μm to 150 x 150 μm spot size) means that spectra are, once again, being collected from single crystals. For non-isotropic minerals, like quartz, the spectra collected from single crystals at these scales are strongly influenced by crystal orientation. It is, therefore, difficult to interpret these spectra using traditional spectral libraries because these spectral libraries lack the spectral detail required to interpret crystallographic information. To assist with the interpretation of the datasets collected using these high-resolution instruments, new and more detailed spectral libraries containing the spectra from oriented mineral crystals are required.

To assist with the creation of these new spectral libraries, we collected reflectance spectra from an oriented quartz crystal. These spectra were then used to document how the position and intensity of absorption features changed in the mid-infrared (7-15 μm) as the quartz crystal was rotated from the c-axis. These spectra were then compared to a second set of quartz spectra that were obtained from an igneous rock (i.e., the measurements were collected in-situ). Finally, we demonstrate that band ratios performed on quartz spectra can be used to derive orientation information, which can be used to determine if a rock containing quartz has been deformed.

4.2 Background

In the mid-infrared (6-15 μm) reflectance spectra of quartz, there are nine spectral features of importance. Three of these spectral features are reflectance minima, one is a reflectance trough, and five are reflectance peaks. The three

minima are located at 7.38 (i.e., the Christiansen feature), 12.2, and 14.2 μm (Table 4-1). The Christiansen feature and the minima at 12.2 μm are located where the refractive index of quartz is equal to one (e.g., Henry, 1948; Conel, 1969; Logan et al., 1973; Salisbury et al., 1991; Wald and Salisbury, 1995). The minimum at 14.2 μm is located where the refractive index is small (e.g., $1 < n < 2$) (Conel, 1969).

Two intense peaks are located at 8.5 and 9.0 μm, and they are found at wavelengths where the absorption coefficient of quartz is very high (e.g., $\kappa = 6\text{-}9$) and where the index of refraction is very low (e.g., $n = \sim 0$). The very strong absorption coefficient produces a mirror-like opacity, and the spectrum at these wavelengths is dominated by simple Fresnel reflectance to produce Reststrahlen bands (Salisbury et al., 1991). The peak at 8.5 μm is produced by the fundamental Si-O asymmetric stretch between adjacent Si-O tetrahedra, whereas the peak at 9.0 μm is produced by the fundamental Si-O asymmetric stretch within the Si-O tetrahedra (McCracken et al., 1983; Salisbury et al., 1991).

Located between these two peaks is a distinct trough at 8.63 μm. This trough is not a gap between the two partially overlapping peaks; rather, it is a distinct absorption band produced by a sharp drop in the absorption coefficient ($\kappa = \sim 2.5$) combined with an increase in the refractive index (Simon and McMahon, 1963). This trough is produced by the absorption of ordinary rays by the quartz crystal (Reinkobor, 1911; Simon and McMahon, 1953; Conel, 1969; McCracken et al., 1995).

A peak at 12.5 μm is present in all quartz spectra, and this spectral feature is caused by the reflection of ordinary rays by the quartz crystal. It occurs when the absorption coefficient of quartz (κ = <2) is higher than the index of refraction (n = >1). Most quartz spectra also contain a peak at 12.8 μm, and this peak is related to the reflection of the extraordinary ray. It occurs where the index of refraction (κ = ~4) is much higher than the absorption coefficient (n = ~0.5) (Reinkobor, 1911; Saksena, 1940; Simon and McMahon, 1953; Lyon and Burns, 1963). In addition, the weak peak at 14.4 μm is also produced by the reflection of the ordinary ray by the quartz crystal (Saksena, 1940; Simon and McMahon, 1953).

4.3 Methods

4.3.1 Samples and Data Collection

4.3.1.1 Single Crystal Quartz Measurements

A natural well-formed, clear and colorless, chemically pure, unstrained, hydrothermal quartz crystal (2.5 cm long, 1 x 1 cm wide) from Brazil with a prismatic-pyramidal shape was cut perpendicular to the c-axis to produce two crystal fragments (Figure 4-2). Reflectance spectra were collected from the c-axis (0°), the a-axis (90°), and an intermediate crystal face (38°) (Figure 4-3). Three spectra were collected from the c-axis; two spectra were collected from each a-axis, totaling six spectra; and four spectra were collected from the intermediate crystal face. Without exception, the spectra collected from each orientation were

identical. The spectra obtained from each orientation were averaged to produce a single representative spectrum.

The spectra were collected using a Brucker Vertex 3000 micro-FTIR instrument. The aperture was square, and it was set to a size of 100 x 100 μm. The incident radiation was un-polarized, and each spectrum was comprised of 32 scans with a spectral resolution of 4 cm^{-1}. The spectra were collected in radiance and converted to reflectance using a gold standard.

4.3.1.2 In-Situ Quartz Measurements

A sample of Archean granite (Inco-37) collected at surface in the Sudbury region, Ontario, containing minerals such as quartz, feldspar, biotite, and hornblende was mounted to a slide and polished to a thickness of ~300 μm. Reflectance spectra were collected from the polished surface using a Thermo Nicolet Nexus 470 FTIR instrument mounted with a Nicolet Continuum infrared microscope. The incident radiation was un-polarized, and the square aperture was set to a size of 100 x 100 μm. Each spectrum was comprised of 30 scans with a spectral resolution of 2 cm^{-1}. The spectra were collected in radiance and converted to reflectance using a gold standard.

Spectra were collected in four quadrants, with each quadrant containing 25 rows and 25 columns, totaling 625 spectra in each quadrant. There was a 300 μm spacing between each row and each column. In total, 2,500 spectra were collected from an area of 1.5 x 1.5 cm.

4.3.2 Spectral Identification of Quartz

The 2,500 reflectance spectra collected from the Inco-37 thick section included the reflectance spectra of many rock-forming minerals. Three steps were performed to identify the pure quartz spectra in this dataset.

First, the AuxMatch algorithm contained within the TSG software (CSIRO & AusSpec) was used to determine how similar each spectrum in the dataset was to spectra contained within a user-provided spectral library (Berman, 2006). The first spectral library was comprised of the three reflectance spectra produced by the oriented quartz crystal (Figure 4-3). The AuxMatch algorithm used a Pearson correlation, which produced a numerical value or 'similarity index' between 0 and 1—with 1 being a perfect spectral match.

Using the full spectral range, a similarity index was assigned for each of the three spectra to each spectrum in the dataset. The output was the similarity index with the highest value, and this value was linked to the spectrum in the spectral library that was deemed to be the most similar. This run of the algorithm was successful at identifying spectra within the Inco-37 dataset that most closely resembled the quartz spectra collected from the oriented quartz crystal, but the values for the similarity index were not very high.

To increase the similarity index values, the algorithm was run a second time using a spectral library comprised of five quartz spectra that were manually and visually selected from the Inco-37 dataset. The five spectra were selected because they appeared to be pure quartz spectra. In addition, they showed the same variation in their spectral shape as the oriented quartz crystal.

After the algorithm was run a second time using spectra obtained from the Inco-37 dataset, a threshold value of ~0.85 was set for the similarity index. All of the spectra in the Inco-37 dataset with a value below this number were masked and not included in the subsequent analyses. Spectra with a similarity index <0.85 frequently contained the spectral features of quartz in combination with the spectral features of other minerals, such as feldspar or biotite, and were not collected from pure quartz. The majority of spectra with a similarity index >0.85 contained only the spectral features of quartz, but some spectra also contained weak spectral features from other minerals.

Second, in order to distinguish between pure quartz spectra and quartz spectra that also contained the spectral features of feldspar, the reflectance of each spectrum at 8.90 μm was subtracted from that at 9.00 μm (Eq. 1).

(Eq. 1) $$Ref_{9.00} - Ref_{8.90}$$

In a spectrum of pure quartz, the peak at 9.00 μm is the most intense peak between 7 and 15 μm, and any modification to the intensity of this peak can be explained by the presence of feldspar, which has an intense absorption feature at 9.00 μm. In the Inco-37 dataset, spectra from pure quartz produced a value close to zero for this calculation. A spectrum dominated by quartz but also displays an absorption feature at 9.00 μm—which is caused by the presence of feldspar—produces a negative value for this calculation. For the Inco-37 dataset, any

spectrum that produced a result outside the range of 0 to -0.37 was not obtained from pure quartz and was not included in the subsequent steps.

Third, each spectrum that produced a result between 0 and -0.37 was visually inspected to ensure that the spectrum was collected from pure quartz. This was done visually by examining the second derivative spectrum between 10 and 12 μm. In this wavelength range, the second derivative spectrum of pure quartz should resemble a horizontal line centered on the zero value. Any marked deviation from zero between 10 and 12 μm indicates the presence of another mineral, such as biotite and/or hornblende. Micas and amphiboles often produce moderate to intense peaks between 10 and 12 μm, and their presence—however small—would be observed within this wavelength range in the second derivative spectrum. As a result, any spectrum with a deviation from zero between 10 and 12 μm were masked, and the remaining spectra were classified as pure quartz. In total, 285 (11%) pure quartz spectra were identified.

4.3.3 Quartz Spectral Analysis

We mathematically identified the exact position at which the nine spectral features of quartz were located in the 285 pure quartz spectra from the Inco-37 dataset and the three spectra from the oriented quartz crystal. To identify the position of each spectral feature, the spectral intensity within a specified wavelength range was examined in either the reflectance or second derivative spectrum (Table 4-1). The wavelength at which the maximum or minimum value for intensity occurred was calculated for each wavelength range. The following statistics were calculated on the results obtained from the 285 spectra from the

Inco-37 dataset: average wavelength, standard deviation, minimum, median, and maximum. In addition, it was then determined if there was any displacement of the spectral features within each dataset.

Five relevant band ratios were calculated to capture changes in the intensity of the major spectral features of quartz, which allows us to examine how the quartz spectra vary with orientation. The specific wavelengths used to calculate the band ratios were based on the average wavelength position of each spectral feature identified in the Inco-37 dataset (see Table 4-1). Equations 2 and 3 determine the intensity of the trough at 8.63 μm in relation to the two peaks at 8.48 and 9.01 μm; equations 4 and 5 determine the intensity of the peaks at 12.50 and 12.79 μm in relation to a point between them at 12.64 μm; equation 6 compares the spectral features at 8.48 and 9.01 μm with those at 12.50 and 12.79 μm; and equation 7 determines the intensity of the peak at 14.44 μm in relation to the minima at 14.23 μm.

(Eq. 2) $Ref_{8.48} / Ref_{8.63}$

(Eq. 3) $Ref_{9.01} / Ref_{8.63}$

(Eq. 4) $Ref_{12.50} / Ref_{12.64}$

(Eq. 5) $Ref_{12.79} / Ref_{12.64}$

(Eq. 6) $Ref_{12.50}/Ref_{12.79}$

(Eq. 7) $Ref_{14.44} / Ref_{14.23}$

4.4 Results

4.4.1 The Spectral Features of Quartz

In spectra collected from the a-axis of the oriented quartz crystal, five peaks were observed at 8.51, 8.98, 12.52, 12.83, and 14.44 μm (Table 4-1). These peaks were observed at 8.48, 9.07, 12.50, 12.80, and 14.45 μm in the spectra collected at a 38°-angle from the c-axis. In spectra collected from the c-axis, four main peaks were present: 8.48, 9.10,12.53, and 14.49 μm. In addition, the peak at 8.48 μm is accompanied by a distinctive lobe at 8.28 μm, and a small peak at 9.30 μm is located near the strong peak at 9.10 μm. For the 285 spectra collected from Inco-37, five peaks were identified between 8.46-8.51, 8.94-9.10, 12.48-12.52, 12.68-12.83, and 14.42-14.46 μm (Table 4-1).

In the reflectance spectra collected from the a-axis of the oriented quartz crystal, the three minima and the trough were observed at 7.37, 8.63, 12.27, and 14.25 μm (Table 4-1). These spectral features were observed at 7.40, 8.63, 12.27, and 14.25 μm in spectra collected at a 38°-angle from the c-axis. In reflectance spectra collected from the c-axis, these spectral features were observed at 7.44, 8.63, 12.28, and 14.25 μm. For the 285 quartz spectra collected from Inco-37, these four spectral features were observed at 7.25-7.48, 8.63-8.64, 12.26-12.29, and 14.21-14.25 μm (Table 4-1). Overall, the wavelength ranges at which the nine major spectral features of quartz are observed are very similar between the two datasets, and these results also compare favorably with the historical literature (e.g., Coblentz, 1906; Reinkober, 1911; Plyler, 1929).

The spectra in these two datasets are similar to each other in many respects. Both datasets show that the intensity of the trough at 8.63 μm changes in conjunction with the intensity of the peaks at 12.5, 12.8, and 14.4 μm. For the Inco-37 dataset, equations 2 and 3 were used to calculate band ratios to estimate the intensity of the trough at 8.63 μm. Spectra #1 and #5 (Figure 4-4) produced the endmember values for both of these band ratios, whereas spectra #2 to 4 were identified by their quartile placement between these two endmember based on the $Ref_{9.01}/Ref_{8.63}$ calculation (Figure 4-4, 4-5).

The spectrum with the most intense trough at 8.63 μm (i.e., spectrum #1) (Figure 4-4) has a similar overall shape to the spectrum collected from the c-axis of the oriented quartz crystal (Figure 4-3). Therefore, it is reasonable to assume that spectrum #1 was collected from the c-axis of a quartz crystal contained within the thick section. Additionally, the spectrum with the least intense trough at 8.63 μm (i.e., spectrum #5) has a very similar overall shape to the spectrum collected from the a-axis of the oriented quartz crystal. Therefore, it is also reasonable to assume that spectrum #5 was collected from the a-axis of a quartz crystal contained within the thick section. Furthermore, we can then assume that the remaining quartz spectra were collected from crystals that display intermediate orientations.

There are, however, some important differences between the spectra collected from the oriented quartz crystal and the spectra contained within the Inco-37 dataset. In the spectra collected from the oriented quartz crystal, the spectrum from the c-axis contains two additional peaks at 8.28 and 9.30 μm

(Figure 4-3). The presence of these two additional peaks makes the peaks at 8.48 and 9.10 μm appear broader when compared to the spectra collected from the a-axis and the 38°-angle crystal face (Figure 4-4). For equations 2 and 3, respectively, the results for the oriented quartz crystal are as follows: c-axis = 1.67 and 2.21; 38° = 1.45 and 1.64; a-axis = 1.24 and 1.34. The results for the a-axis and the 38° spectra fall on the linear trend defined by the Inco-37 dataset (Figure 4-5). The results for the c-axis, however, do not plot on this trend line. The results for equation 2 fall within the range established by the Inco-37 dataset, which indicates that there is a consistency in the intensity between the peak at 8.48 μm and the trough at 8.63 μm between the two datasets. The results for equation 3, however, encompass a larger range than the Inco-37 dataset. The spectrum from the c-axis of the oriented quartz crystal has a much larger peak at 9.01 μm in relation to the trough at 8.63 μm than the spectra from the Inco-37 dataset that were also collected from the c-axis.

4.4.2 Variations in Spectral Feature Location and Intensity Caused by Crystal Orientation

All spectral features but one demonstrated a systematic shift in their position as a function of crystal orientation (Table 4-1). In general, the Christensen feature at 7.35, and the peaks at 9.0, 12.5, and 14.4 μm were all documented at longer wavelengths in spectra collected from the c-axis. Furthermore, the peaks at 8.5, 12.2, and 12.8 μm, and the trough at 8.63 μm were all documented at shorter wavelengths. No systematic shift was documented for the minima at 14.4 μm.

Four spectral features showed changes in their intensity as a function of orientation: the trough at 8.63 μm varied in its intensity in relation to the peaks at 8.5 and 9.0 μm; the peaks at 12.5 and 12.8 μm varied in their intensity in relation to each other, and the peak at 14.4 μm varied in its intensity in its relation to the minima at 14.2 μm. Band ratios were used to visualize and characterize these changes in the spectra.

Changes in the intensity of the trough at 8.63 μm are best displayed by plotting the results of equation 2 and equation 3 (Figure 4-5). These band ratios captured changes in the depth of the trough at 8.63 μm with respect to the peaks situated on either side of it. For the Inco-37 dataset, there is a linear relationship between these two band ratios, and the data follow the trend line very closely (R^2 = 0.99). Spectra collected from the c-axis (e.g., spectrum #1) produce a very intense trough at 8.63 μm, whereas spectra collected from the a-axis (e.g., spectrum #5) produce a very weak trough. Between these two endmembers, the change in trough intensity is continuous. The linear trend of this plot, and its very high R^2 value, resulted in these two band ratios being used to select the spectra displayed in Figure 4-3. These five spectra were also included in Figures 4-5 to 4-8 to show how the distribution of the results change depending on the spectral feature being examined.

Changes in the relative intensity of the two peaks at 12.5 and 12.8 μm were quantified using equation 4 and equation 5 (Figure 4-6). These band ratios relate the intensities of these two peaks to the intensity of the reflectance spectrum at 12.64 μm. The relationship between these two band ratios is linear, and the data

closely follow the trend line ($R^2 = 0.96$). In spectra collected from the c-axis (e.g., spectrum #1), only the peak at 12.5 μm is present. In spectra collected from the a-axis (e.g., spectrum #5), both peaks are present, but the peak at 12.8 μm is more intense. Spectra #3, #4, and #5 fall in the lower right range of this plot indicating that the relative intensity of the two peaks at 12.5 and 12.8 μm do not change at the same rate as the intensity of the trough at 8.63 μm.

The non-linear relationship between the change in the intensity of the trough at 8.63 μm and the change in the relative intensity of the peaks at 12.5 and 12.8 μm can be observed in a plot that shows the results of equation 3 and equation 6 (Figure 4-7). Much of the data are concentrated in the lower left portion of this graph, with spectra collected from the c-axis (e.g., spectrum #1) plotting in the upper right and spectra collected from the a-axis (e.g., spectrum #5) plotting in the lower left.

Changes in the intensity of the peak at 14.4 μm can be quantified using the results of equation 7 and equation 3. These band ratios show how the intensity of the peak at 14.4 μm, with respect to the local minimum at 14.2 μm, changes in relation to the intensity of the peak at 8.5 μm with respect to the trough at 8.63 μm (Figure 4-8). This relationship appears to be linear ($R^2 = 0.89$), but there is a very large spread of the data around the trend line, and much of the data plot in the lower left. Spectra collected from the c-axis (e.g., spectrum #1) produce more intense peaks at 14.4 μm, whereas spectra collected from the a-axis (e.g., spectrum #5) produce weaker peaks at 14.4 μm.

4.4.3 Calculation of Orientation Using Reflectance Spectra

For the Inco-37 dataset, the relationship between the two band ratios $Ref_{8.48}/ Ref_{8.63}$ and $Ref_{9.01}/Ref_{8.63}$ was linear, and the relationship displays a high R^2 value (0.99) (Figure 4-5). As a result, band ratio $Ref_{8.48}/ Ref_{8.63}$ was selected to compute a relationship to translate the spectral data into crystal orientation information. The inherent assumption is that the intensity of the trough at 8.63 μm changes linearly with respect to the peak at 8.48 μm in response to linear changes in the orientation of the quartz crystal between the c-axis (0°) and the a-axis (90°).

First, the minimum value (1.181) for the band ratio $Ref_{8.48}/Ref_{8.63}$ was identified and subtracted from the maximum value (1.631). The difference between these two values was divided by 90, and then each degree from 0 to 90° was assigned a $Ref_{8.48}/Ref_{8.63}$ value (Table 4-3). These values were then plotted as a function of the $Ref_{8.48}/Ref_{8.63}$ band ratio values, and the equation of the resulting linear trend line was calculated:

(Eq. 8) $$\text{Degrees from c-axis} = -200.32(Ref_{8.48}/ Ref_{8.63}) + 326.61$$

This equation was used to translate the individual values of the $Ref_{8.48}/Ref_{8.63}$ band ratio into degree values that represent the orientation angle of each quartz crystal in relation to the c-axis (Figure 4-9). The orientation results can be viewed in two ways: as an image that simulates the surface of the sample (Figure 4-10), or as a histogram that can be used to examine how the orientation data are distributed (Figure 4-11).

There are many benefits to examining the orientation data as a function of its spatial position. This presentation form allows the observer to identify any visual patterns in the data. In the Inco-37 dataset, quartz does not appear to have a preferred orientation. However, the histogram reveals that the orientation data do not have a normal distribution. Some orientations are preferred, and the data appear to be multimodal. The average orientation is 49.4°, and the median is 54.4°. The higher occurrence of values between 50 and 75° indicates that there is some alignment of quartz in this rock. At this point, it is difficult to state the importance of this non-normal distribution because there are no other datasets to compare it to, but it appears as if this sample of granite displays a very minor fabric.

4.5 Discussion

4.5.1 How Changes in Crystal Orientation Change the Position and the Intensity of the Spectral Features of Quartz

Variations in the reflectance spectra of quartz were noted in the early 1900s, when it was established that they were caused by the anisotropic properties of quartz. This anisotropy causes radiation incident upon a quartz crystal to be split into two linearly polarized beams that travel in directions perpendicular to each other: one referred to as the ordinary ray and one referred to as the extraordinary ray. However, when radiation travels directly along the optical axis (i.e., the c-axis), all of the radiation travels as ordinary rays. This means that the spectral features produced by the passage of the ordinary ray through quartz will

be strongest in reflectance spectra collected from the c-axis. Also, as quartz is rotated from the c-axis, the number of extraordinary rays increases in proportion to a decrease in the number of ordinary rays. This phenomenon explains most of the variations observed in the mid-infrared reflectance spectra of quartz.

For example, there are four spectral features—8.63, 12.5, 12.8, and 14.4 μm—in the mid-infrared spectra of quartz that are the product of either the ordinary ray or the extraordinary ray (Reinkober, 1911; Saksena, 1940; Simon and McMahon, 1953; Conel, 1969; Lyon and Burns, 1963; McCracken et al., 1995). It is these four spectral features that vary in their intensity as the orientation of quartz changes.

A spectrum collected from the c-axis will only exhibit the spectral features produced by the ordinary ray (i.e., 8.63, 12.5, and 14.4 μm). In spectra collected from the c-axis, the trough at 8.63 μm and the two peaks at 12.5 and 14.4 μm are at their maximum intensity. Spectra collected from the a-axis exhibit the spectral features produced by both the ordinary and extraordinary rays (i.e., 12.8 μm). In spectra collected from the a-axis, the peak at 12.8 μm is at its strongest intensity, but the spectral features at 8.63, 12.5, and 14.4 μm are at their weakest. The change in the intensity is continuous between these two extremes and is dependent on the orientation of the quartz crystal.

The systematic shift of the spectral features can also be explained by the anisotropic properties of quartz. As quartz is rotated, the absorption coefficient and the refractive index change as a function of its crystallographic orientation (Reinkobor, 1911; Simon and McMahon, 1953; Conel, 1969; McCracken et al.,

1995). This slight but systematic change of the absorption coefficient and the refractive index results in a shift of the related spectral features.

4.5.2 The Usefulness of Calculating Orientation Using Reflectance Spectra

The changes observed in the reflectance spectra of quartz collected from single crystals appear to be continuous between two endmembers, and all intermediate forms appear to exist. To estimate the orientation of individual crystals, we calculated the intensity of the trough at 8.63 μm in relation to the peaks at 8.48 and 9.01 μm (i.e., band ratios $Ref_{8.48}/Ref_{8.63}$ and $Ref_{9.01}/Ref_{8.63}$) (Figure 4-5). The trough at 8.63 μm is formed by the absorption of the ordinary ray, and the intensity of this trough changes as the number of ordinary rays absorbed by the crystal changes (Reinkobor, 1911; Simon and McMahon, 1953; Conel, 1969; McCracken et al., 1995). There is little chance that the intensity of this trough is modulated by any nearby spectral features because this trough is not located near spectral features formed by the extraordinary ray.

The band ratio $Ref_{8.48}/Ref_{8.63}$ was used to assign an estimate of orientation to each spectrum based on the intensity of the trough at 8.63 μm(Figure 4-10, 4-11). There is a problem, however, when using spectral data to infer the orientation of quartz grains contained within a rock because it is not possible to know if a single spectrum was collected from an individual quartz crystal or two or more quartz crystals located adjacent to each other. This means that the Inco-37 dataset contains a population of spectra that were collected from two or more adjacent quartz crystals, and the associated spectra were produced by spectral mixing. For

example, two adjacent quartz crystals may be oriented at different angles, and the resulting spectrum is a proportional mixture of these two spectra. Although this type of mixing would be decipherable and avoidable using microscopy and visual interpretation, it is not detectable or avoidable using spectroscopy. This introduces errors into the orientation results shown in figures 4-10 and 4-11; however, it is assumed that this mixing would be randomly distributed over the entire dataset and would not result in the skewing of the data.

In addition, the calculation used to estimate orientation is heavily weighted on the assumption that the intensity of the trough at 8.63 μm changes in a linear manner with a linear change in orientation, and it is quite possible that this assumption is incorrect. In the preliminary phases of this research, it was postulated that the reflectance spectra collected from the intermediate crystal face (38°) of the oriented quartz crystal could be used to verify or falsify this assumption. However, due to subtle differences in the shape of the spectra in the two datasets between 8 and 9.5 μm—which causes the band ratio results from the oriented quartz crystal to plot outside the ranges for the Inco-37 dataset (Figures 4-5, 4-6, 4-7, and 4.8)—it was not possible to verify the orientation estimations.

Although it is not fully understood at this time why the oriented quartz crystal and the Inco-37 dataset produced reflectance spectra with slightly different shapes between 8 and 9.5 μm, it is likely related to the manner in which the samples were formed. The oriented quartz crystal has a hydrothermal origin, whereas the quartz in Inco-37 formed through magmatic processes. Further research will examine differences in the mid-infrared reflectance spectra of

hydrothermal, igneous, and metamorphic quartz from a variety of localities. It is possible that the natural variability observed in the reflectance spectra of quartz may be useful in identifying and characterizing quartz that has formed through different processes.

4.6 Conclusions

Although much of the fundamental research on the reflectance spectroscopy of quartz was conducted approximately 100 years ago, we have revisited this topic to fully document the effect that orientation has on a quartz reflectance spectrum. This work was completed to produce a spectral library for quartz that includes information about mineralogy and crystal orientation, and these reflectance spectra can be used to interpret the datasets collected by high spatial resolution reflectance spectrometers.

Two datasets of quartz spectra were collected—one from an oriented quartz crystal and another from a piece of granite (Inco-37). In total, nine spectral features were examined. All but one of these spectral features show systematic displacement in response to changes in the orientation of quartz. In addition, four of these spectral features vary in their intensity with changes in the orientation of the quartz crystal. This variability is explained by the anisotropic properties of quartz, where the absorption coefficient and the refractive index varies as a function of its orientation. Some of the variations observed were linear, and as a consequence, two band ratios $Ref_{8.48}/Ref_{8.63}$ and $Ref_{9.01}/Ref_{8.63}$ were used to infer the orientation of individual quartz crystal in the Inco-37 sample. In summary, the reflectance spectra presented here can be included in the spectral libraries used to

interpret spectra collected at high spatial resolutions, and, in addition, the analysis methods that we have developed can be used judiciously to identify fabric in rocks.

4.7 Acknowledgments

We thank Thomas Stachel (De Beers Diamond Research Lab, University of Alberta, Canada) and Roland Stalder (University of Innsbruck, Austria) for the use of their spectrometers.

4.8 Tables

Table 4-1: The reflectance spectral features of quartz between 7 and 15 μm

Description	Historical Publications	Calculations Performed on Spectra	Oriented Quartz Crystal (n = 13)			Inco-37 Dataset (n = 285)			
	Position (μm)		C-Axis Avg. μm	38° Avg. μm	A-Axis Avg. μm	Position Range (μm)	Avg. μm & Std. Dev.	Med. (μm)	n
Minimum	7.35	Min. reflectance b/w 7-7.6 μm	7.44	7.40	7.37	7.25-7.48	7.38 (δ = 0.04)	7.38	285
Peak	8.5	Max. reflectance b/w 8.4-8.6 μm	8.29	8.48	8.51	8.46-8.51	8.48 (δ = 0.01)	8.48	285
Trough	8.63	Min. reflectance b/w 8.53-8.73 μm	8.63	8.63	8.63	8.63-8.64	8.63 (δ = 0.00)	8.63	285
Peak	9.0	Max. reflectance b/w 8.8-9.2 μm	9.10	9.07	8.98	8.94-9.10	9.01 (δ = 0.03)	9.01	285
Local Min.	12.2	Max. 2nd derivative b/w 12.15-12.35 μm	12.28	12.27	12.27	12.26-12.29	12.27 (δ = 0.01)	12.27	285
Peak	12.5	Max. reflectance b/w 12.4-12.6 μm	12.53	12.50	12.52	12.48-12.52	12.50 ((δ = 0.01)	12.50	285
Peak	12.8	Max. reflectance b/w 12.7-12.9 μm	---	12.80	12.83	12.68-12.83	12.79 (δ = 0.03)	12.80	246
Local Min.	14.2	Max. 2nd derivative b/w 14.1-14.3 μm	14.25	14.25	14.25	14.21-14.25	14.23 (δ = 0.01)	14.23	285
Peak	14.4	Max. reflectance b/w 14.3-14.5 μm	14.49	14.45	14.44	14.42-14.46	14.44 (δ = 0.01)	14.44	285

Table 4-2: Summary of conversion table for obtaining orientation information using the band ratio $Ref_{8.48}/Ref_{8.63}$

Degrees from C-Axis	Band Ratio Value
0	1.631
5	1.606
10	1.581
15	1.556
20	1.531
25	1.506
30	1.481
35	1.456
40	1.431
45	1.406
50	1.381
55	1.356
60	1.331
65	1.306
70	1.281
75	1.256
80	1.231
85	1.206
90	1.181

4.9 Figures

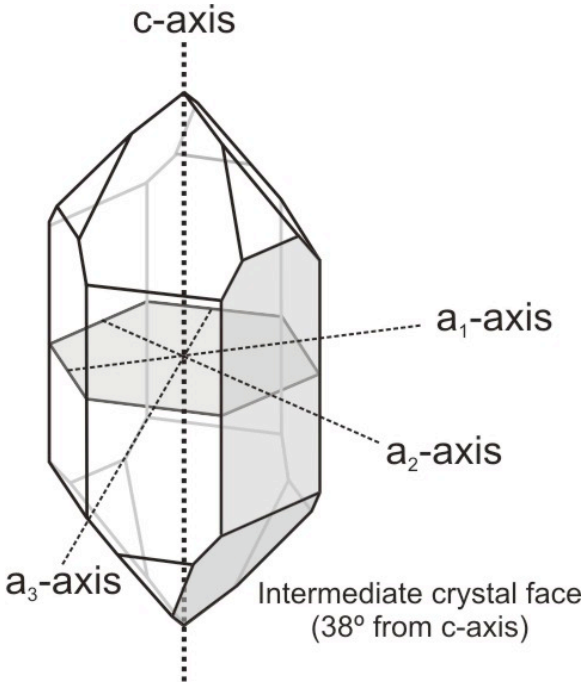

Figure 4-1. An idealized quartz crystal with its axes labeled. Shaded planes indicate locations where reflectance spectra were collected.

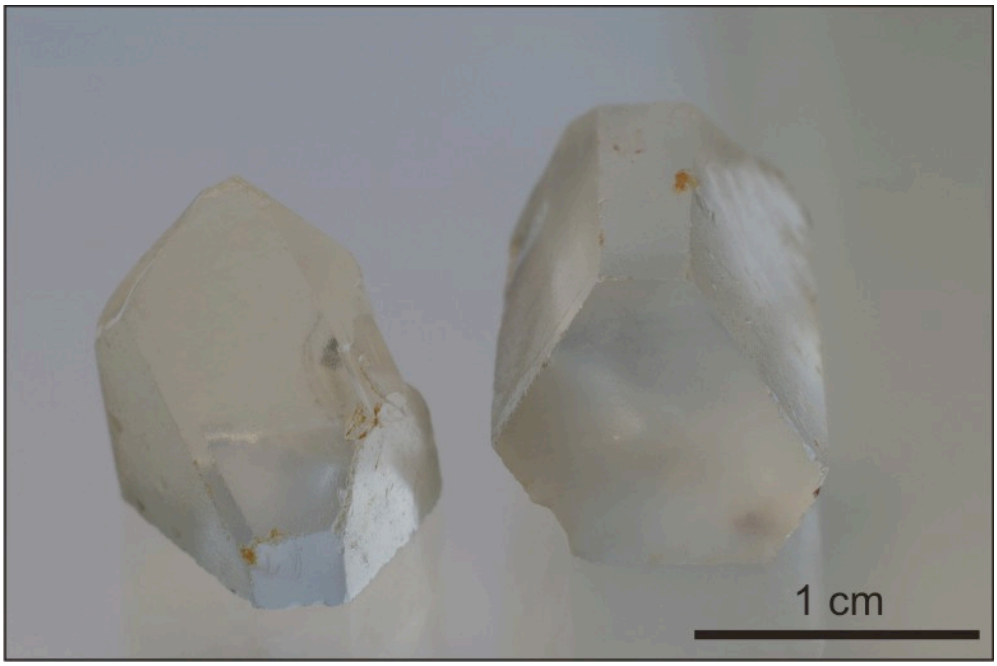

Figure 4-2. Photo of a natural well-formed, clear and colorless, chemically pure hydrothermal quartz crystal from Brazil that was cut into two pieces. Reflectance spectra were collected from the c- and a-axis, and the 38-degree crystal face.

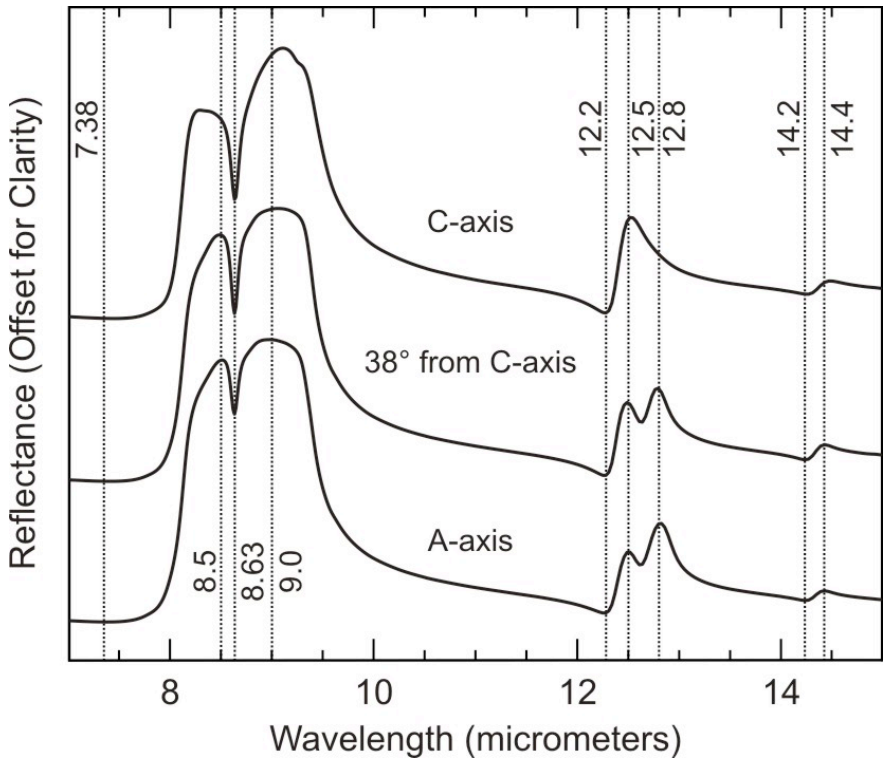

Figure 4-3. Reflectance spectra (7-15 μm) from the c- and a-axis of quartz, including a spectrum collected at an angle of 38 degrees from the c-axis (aperture size = 100 x 100 μm). Major spectral features are identified using dashed lines.

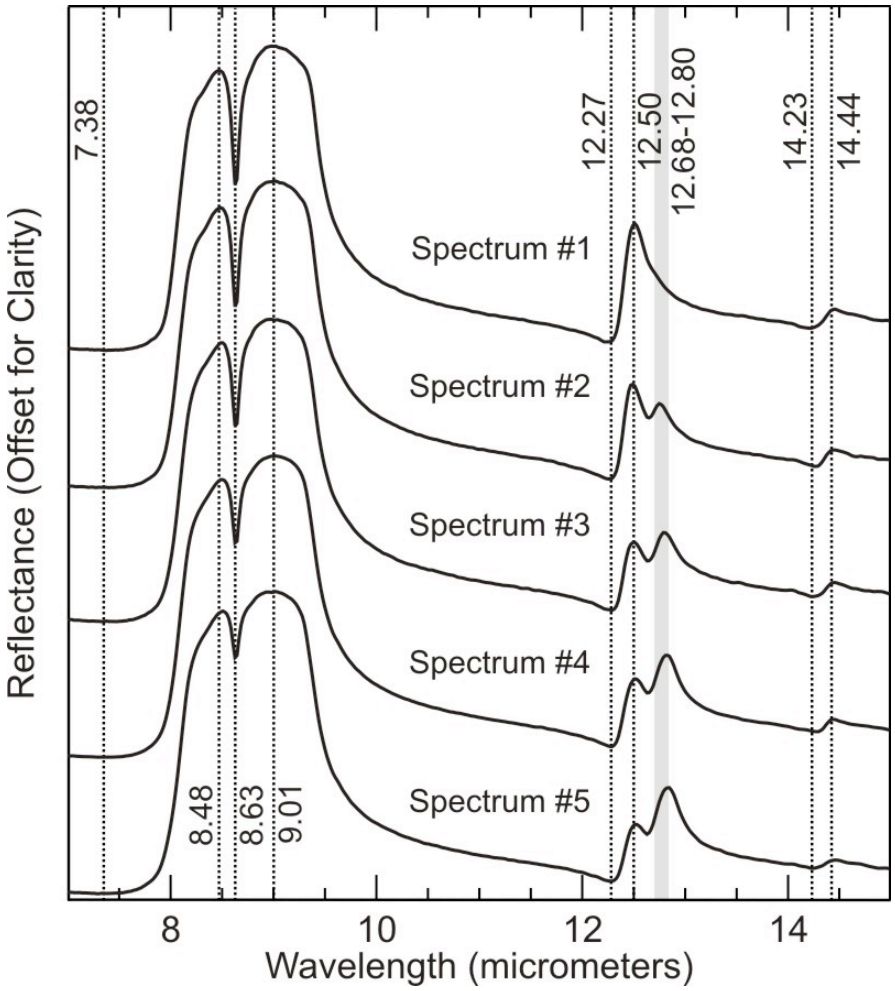

Figure 4-4. Reflectance spectra (7-15 μm) of quartz collected from Inco-37 (aperture size = 100 x 100 μm). Major spectral features are identified using dashed lines or a grey box. The wavelength value of each spectral feature is based on the average wavelength position calculated for the dataset of 285 spectra.

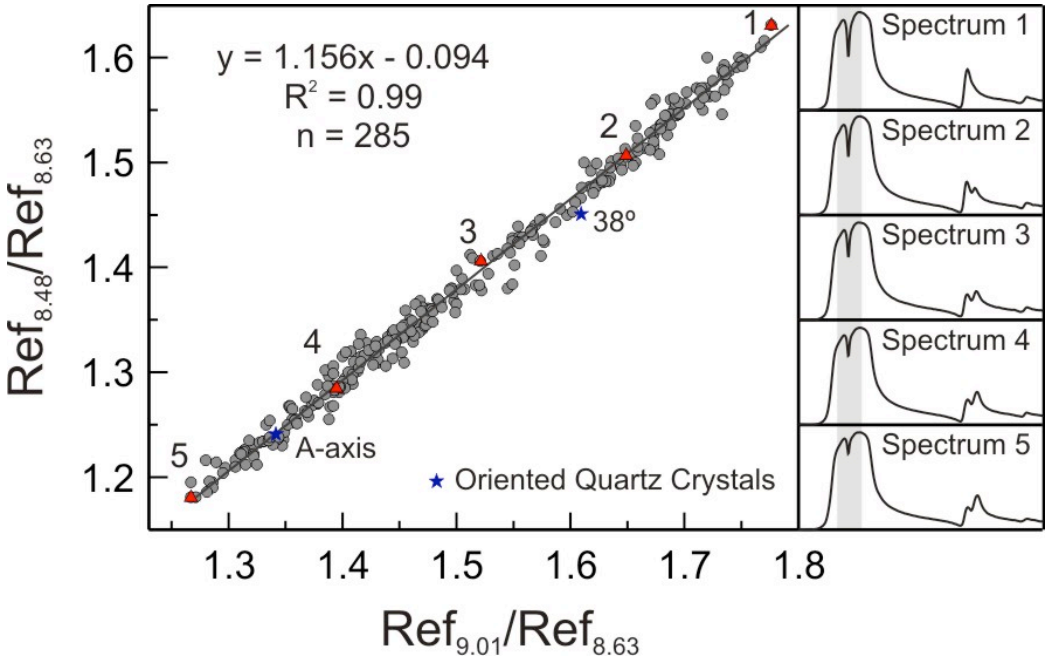

Figure 4-5. Band ratio $Ref_{8.48}/Ref_{8.63}$ versus band ratio $Ref_{9.01}/Ref_{8.63}$ plotted for 285 pure quartz spectra collected from Inco-37. Reference spectra (red triangles) and the results from oriented quartz grains (blue stars) are included for comparison. The grey box denotes the region of interest. The value for the c-axis plots out of range (2.21, 1.67).

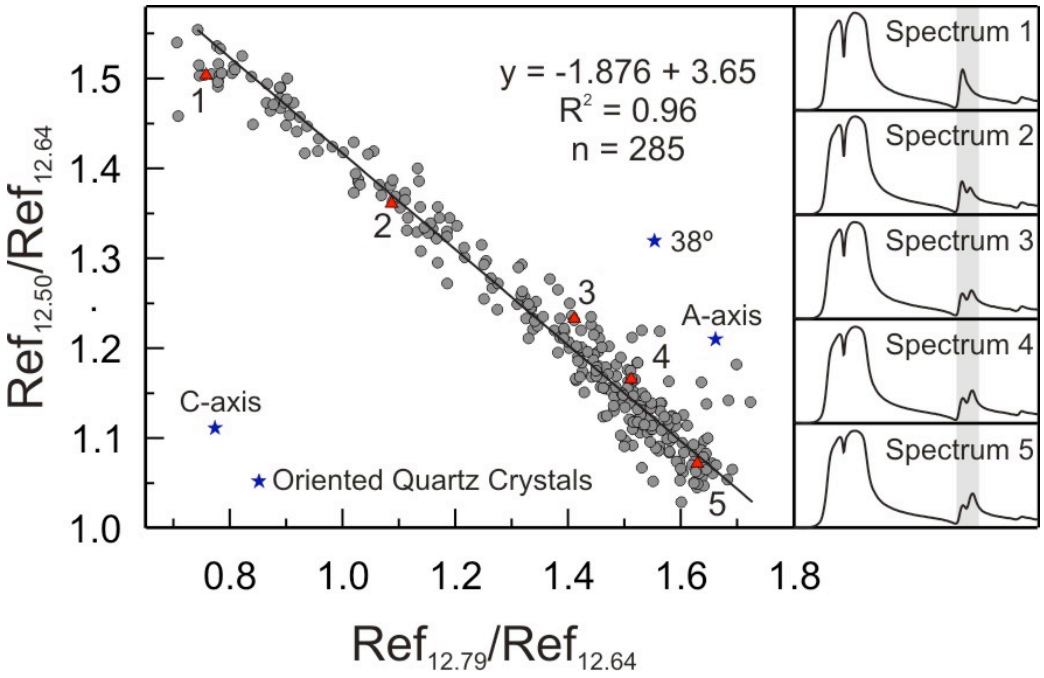

Figure 4-6. Band ratio $Ref_{12.50}/Ref_{12.64}$ versus band ratio $Ref_{12.79}/Ref_{12.64}$ plotted for 285 pure quartz spectra collected from Inco-37. Reference spectra (red triangles) are included for comparison. The grey box denotes the region of interest.

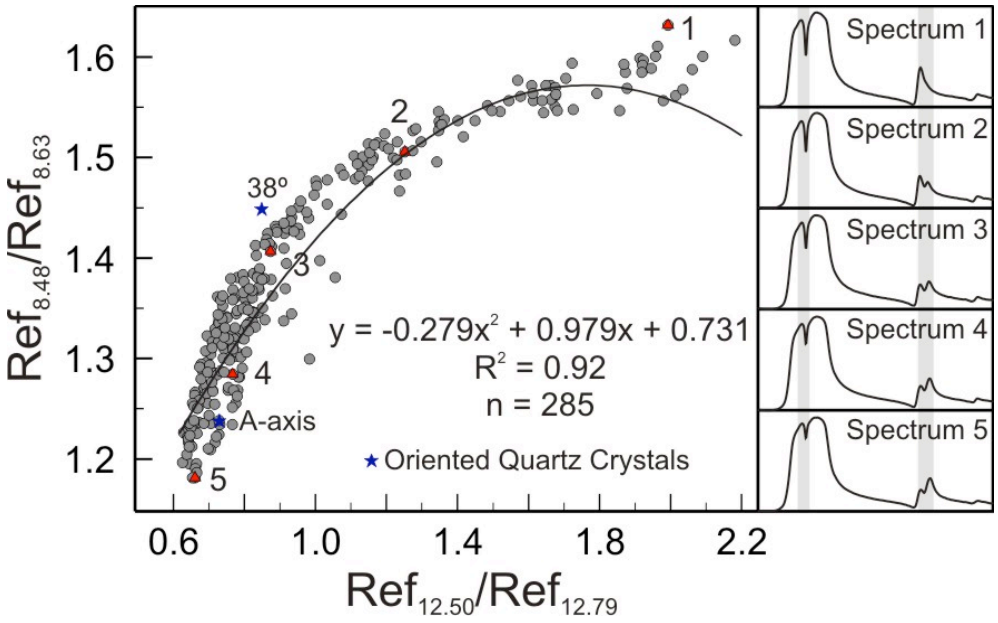

Figure 4-7. Band ratio $Ref_{8.48}/Ref_{8.63}$ versus band ratio $Ref_{12.50}/Ref_{12.79}$ plotted for 285 pure quartz spectra collected from Inco-37. Reference spectra (red triangles) are included for comparison. The grey box denotes the regions of interest. The value for the c-axis plots out of range (1.47, 1.67).

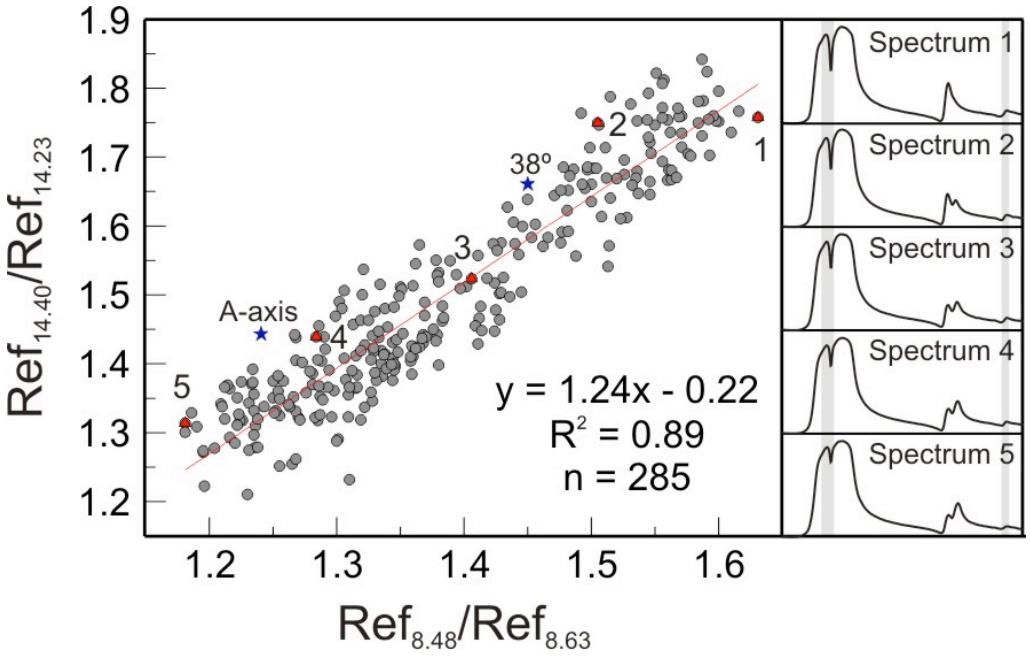

Figure 4-8 Band ratio $Ref_{14.40}/Ref_{14.23}$ versus band ratio $Ref_{8.48}/Ref_{8.63}$ plotted for 285 pure quartz spectra collected from Inco-37. Reference spectra (red triangles) are included for comparison. The grey box denotes the regions of interest. The value for the c-axis plots out of range (1.67, 1.47).

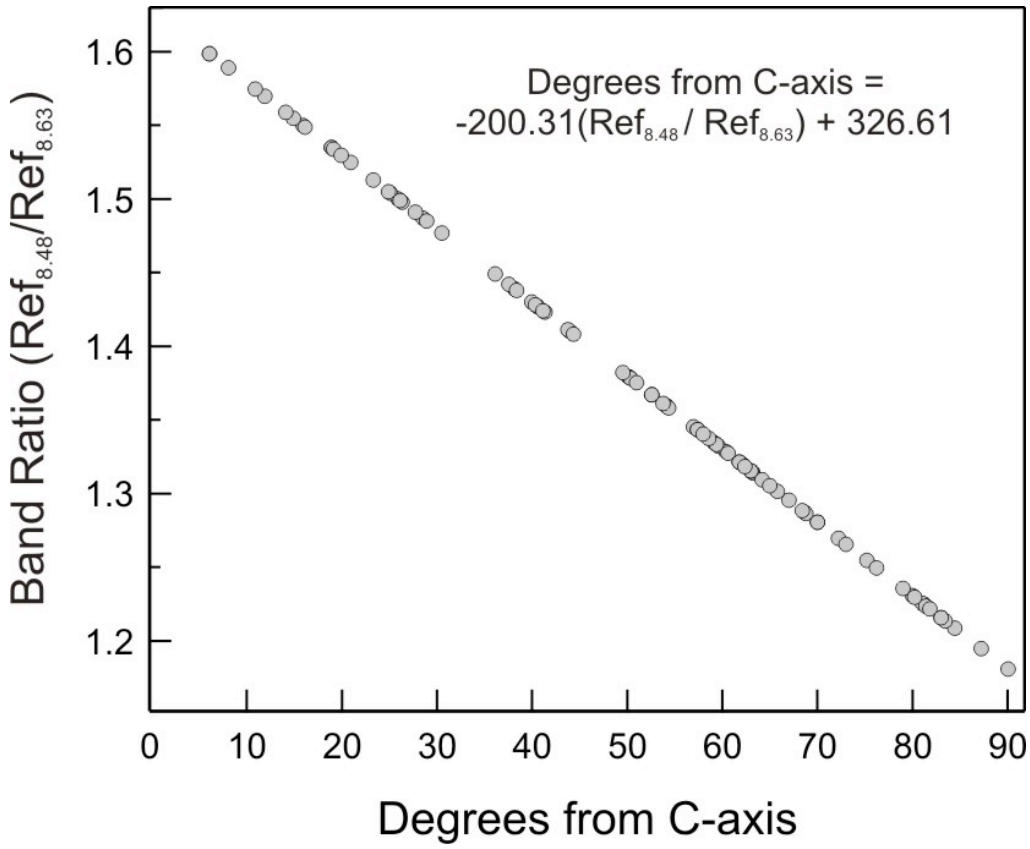

Figure 4-9. The values of the $Ref_{8.48}/Ref_{8.63}$ band ratio plotted against their converted orientation values (degrees from c-axis) for quartz spectra from the Inco-37 dataset.

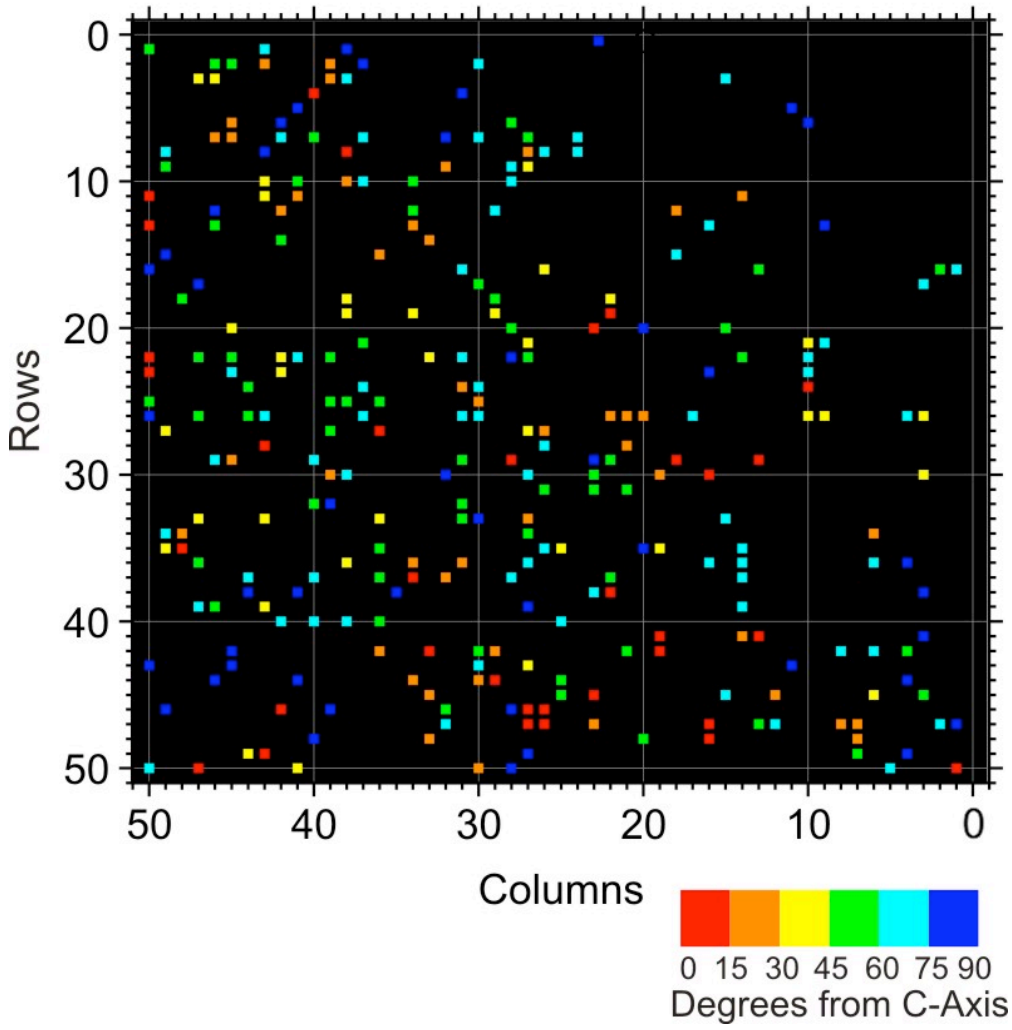

Figure 4-10. The distribution of pure quartz spectra over a 1.5 x 1.5 cm grid collected from Inco-37. Each pixel represents a reflectance spectrum collected from a spot size of 100 x 100 µm, and there is a 300 µm spacing between each row and column. The colors of the pixels denote the orientation of the in-situ quartz spectra (degrees from c-axis) as calculated using the value of the $Ref_{8.48}/Ref_{8.63}$ band ratio. The black pixels belong to spectra collected from minerals other than quartz (e.g., feldspar or mica) or non-pure quartz.

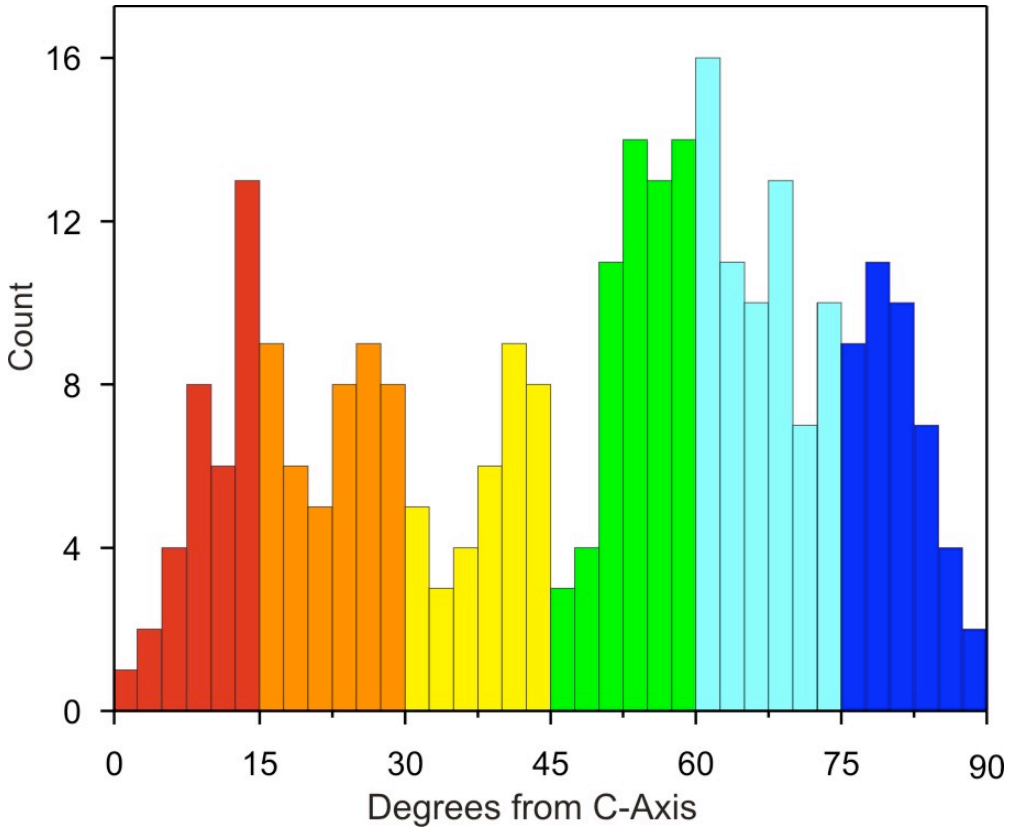

Figure 4-11. The orientation angles (degrees from c-axis) for 285 pure quartz spectra collected from Inco-37 as calculated using the value of the $Ref_{8.48}/Ref_{8.63}$ band ratio.

4.10 References

Coblentz, W.W. (1906) Infra-red absorption and reflection spectra. Physical Review (Series I), 23(2), 125.

Conel, J.E. (1969) Infrared emissivities of silicates: experimental results and a cloudy atmosphere model of spectral emission from condensed particulate mediums. Journal of Geophysical Research, 74, 1,614-1,623.

Henry, R.L. (1948) The transmission of powder films in the infra-red. J. Opt. Soc. Am., 38(9), 775-787.

Logan, L.M., Hunt, G.R., Salisbury, J.W., and Balsamo, S.R. (1973) Compositional implications of Christiansen frequency maximums for infrared remote sensing applications. Journal of Geophysical Research, 78(23), 4,983-5,003.

Lyon, R.J.P., and Burns, E.A. (1963) Analysis of rocks and minerals by reflected infrared radiation. Economic Geology, 58, 274-284.

McCracken, W.J., Person, W.B., and Hench, L.L. (1985) Polarized infrared reflection spectroscopy of single crystal lithia-silicates and quartz. Journal of Material Science, 20, 3,853-3,864.

Plyler, E.K. (1929) Combination frequencies of the infra-red bands of quartz. Physical Review, 33(1), 48.

Reinkober, O. (1911) Über Absorption und Reflexion ultraroter Strahlen durch Quarz, Turmalin und Diamant. Annalen der Physik, 339(2), 343-372.

Saksena, B. (1940) Analysis of the Raman and infra-red spectra of α-quartz. Proceedings Mathematical Sciences, 12(1), 93-139.

Salisbury, J.W., Walter, L.S., Vergo, N., and D'Aria, D.M. (1991) Infrared (2.1-25 μm) spectra of minerals. Johns Hopkins University Press, Baltimore.

Simon, I., and McMahon, H.O. (1953) Study of the structure of quartz, cristobalite, and viterous silica by reflection in infrared. The Journal of Chemical Physics, 21(1), 23-30.

Spitzer, W.G., and Kleinman, D.A. (1961) Infrared lattice bands of quartz. Physical Review, 121(5), 1,324-1,335.

Wald, A.E., and Salisbury, J.W. (1995) Thermal infrared directional emissivity of powdered quartz. Journal of Geophysical Research, 100(B12), 24,665-24,675.

Wenrich, M.L., and Christensen, P.R. (1996) Optical constants of minerals derived from emission spectroscopy: application to quartz. Journal of Geophysical Research, 101, 15,921-15,931.

Chapter 5: General Discussion and Conclusions

5.1 General Discussion

This thesis describes research that illustrates how reflectance spectroscopy can be used in a qualitative, semi-quantitative, and quantitative capacity for characterizing a range of mineralogical and geological materials. This research focuses on the collection of reflectance spectra using a variety of instruments and the development of new methods to analyze and interpret the spectral data. The main goal has been to demonstrate how reflectance spectroscopy can be used in practical settings to accurately identify minerals, quantify their abundance, gather information about their mineral chemistry, and derive orientation information from their reflectance spectra. Each of the three manuscripts contained within this thesis focuses on a distinct aspect of this pursuit.

The first manuscript introduces the possibility that reflectance spectroscopy can be used to log drill core. The drill core selected for this study originated from the iron oxide-copper-gold (IOCG) deposit at Olympic Dam, South Australia. Olympic Dam is the largest known IOCG deposit and one of the largest polymineralic ore deposits in the world; therefore, it would be highly advantageous to develop a method of automated drill core logging that is accurate and efficient. The results of the research presented in Chapter 2 demonstrate that reflectance spectroscopy can be used to differentiate between the ore-bearing and barren zones in drill core, and it can also be used to estimate the abundance of

ferric iron (Fe^{3+}) and aluminum (Al^{3+}) in rocks. In total, 49,500 near-infrared spectra were collected from 300 m of drill core using HyLogger. These spectra were analyzed between 850 and 970 nm, and 2,190 and 2,230 nm to identify the presence of hematite and phengite, respectively, which are the dominant alteration minerals at this ore deposit. Using the results of three calculations, the major and minor compositional units were identified along the drill core, and the resulting logs correlated very well with the visual inspection of the drill core and the whole rock geochemical data.

The second manuscript (Chapter 3) continues with the work introduced in Chapter 2, but it expands upon it by bringing attention to the mineral chemistry, near-infrared spectroscopy, and mid-infrared spectroscopy of the potassic dioctahedral micas (i.e., phengites) found at Olympic Dam. It was discovered that in the ore-bearing zone, the phengites have higher concentrations of aluminum (i.e., high-Al phengites), and they have lower Mg-numbers (i.e., they contain more iron). Conversely, the phengites from the barren zone have lower concentrations of aluminum (i.e., low Al-phengites), and they have higher Mg-numbers (i.e., they contain less iron). These differences were observed by plotting the cation results for aluminum and silicon against the Mg-number in a ternary diagram. The information contained within this manuscript provides those who are searching for the signs of hydrothermal alteration with the information they need to evaluate the mineralogical and spectroscopic data of phengite-bearing mineralized and barren drill core effectively.

The information contained within Chapter 4 diverges slightly from the topic of drill core logging and addresses one of the main phenomena that is observed when spectra are collected at high spatial resolutions (e.g., 100 x 100 μm spot sizes). At high spatial resolutions, the reflectance spectra of non-isotropic minerals display systematic variations that can be explained by changes in the crystal orientation of the mineral. Reflectance spectra were collected from an oriented quartz crystal and from quartz crystals in a rock. In addition to documenting and analyzing the spectral features of quartz that vary in response to changes in crystal orientation, it was discovered that the reflectance spectra of quartz can be used to obtain orientation information from a rock. In total, nine spectral features were examined. Many of these spectral features shifted in a systematic manner in response to changes in the orientation of the quartz crystal. In addition, four of the spectral features were found to vary systematically in their intensity. Two band ratios $Ref_{8.48}/Ref_{8.63}$ and $Ref_{9.01}/Ref_{8.63}$ were then used to infer the orientation of individual quartz crystals.

5.2 Conclusions

The different research topics presented in this thesis are united by a common goal: to provide those who use reflectance spectroscopy for exploration, mining, and research purposes with information they need to interpret their spectra accurately and to obtain meaningful results. The main benefit of using automated instruments to collect reflectance spectra for the purpose of obtaining abundance and mineral chemistry information is that it is no longer necessary to limit the number of samples selected for a study. Research can now be conducted

on a vast number of samples, or thousands of meters of drill core. No longer is it necessary to select samples that are deemed to be representative. Instead, abundance and compositional information can be collected from every surface of every sample, and this information can be stored digitally and viewed in many different ways. As a result, rocks from a field area can be fully documented with a very high level of detail (e.g., 2 x 2 mm pixel size). The datasets associated with these samples contain an enormous amount of information that can be used to document natural processes that are difficult to document using other analytical techniques.